A NOVEL APPROACH FOR THE SOLUTION OF FORWARD AND INVERSE PROBLEMS ASSOCIATED WITH NEAR FIELD MICROWAVE IMAGING SYSTEMS

A THESIS SUBMITTED TO
THE GRADUATE SCHOOL OF NATURAL AND APPLIED SCIENCES
OF
MIDDLE EAST TECHNICAL UNIVERSITY

BY

AKIN DALKILIÇ

IN PARTIAL FULFILLMENT OF THE REQUIREMENTS
FOR
THE DEGREE OF DOCTOR OF PHILOSOPHY
IN
ELECTRICAL AND ELECTRONICS ENGINEERING

AUGUST 2023

Approval of the thesis:

A NOVEL APPROACH FOR THE SOLUTION OF FORWARD AND INVERSE PROBLEMS ASSOCIATED WITH NEAR FIELD MICROWAVE IMAGING SYSTEMS

submitted by **AKIN DALKILIÇ** in partial fulfillment of the requirements for the degree of **Doctor of Philosophy** i**n Electrical and Electronics Engineering, Middle East Technical University** by,

Prof. Dr. Halil Kalıpçılar
Dean, Graduate School of **Natural and Applied Sciences** _____

Prof. Dr. İlkay Ulusoy
Head of the Department, **Electrical and Electronics Engineering** _____

Assoc. Prof. Dr. Lale Alatan
Supervisor, **Electrical and Electronics Engineering, METU** _____

Assoc. Prof. Dr. Sevinç Figen Öktem Seven
Co-Supervisor, **Electrical and Electronics Engineering, METU** _____

Examining Committee Members:

Prof. Dr. Mustafa Kuzuoğlu
Electrical and Electronics Eng. Dept., METU _____

Prof. Dr. S. Sencer Koç
Electrical and Electronics Eng. Dept., METU _____

Assoc. Prof. Dr. Lale Alatan
Electrical and Electronics Eng. Dept., METU _____

Prof. Dr. Vakur B. Ertürk
Electrical and Electronics Eng. Dept., Bilkent University _____

Prof. Dr. Özlem Özgün
Electrical and Electronics Eng. Dept., Hacettepe University _____

Date: 07.08.2023

I hereby declare that all information in this document has been obtained and presented in accordance with academic rules and ethical conduct. I also declare that, as required by these rules and conduct, I have fully cited and referenced all material and results that are not original to this work.

Name Last name : Akın Dalkılıç

Signature :

ABSTRACT

A NOVEL APPROACH FOR THE SOLUTION OF FORWARD AND INVERSE PROBLEMS ASSOCIATED WITH NEAR FIELD MICROWAVE IMAGING SYSTEMS

Dalkılıç, Akın
Doctor of Philosophy, Electrical and Electronics Engineering
Supervisor: Assoc. Prof. Dr. Lale Alatan
Co-Supervisor: Assoc. Prof. Dr. Sevinç Figen Öktem Seven

August 2023, 126 pages

In recent near field microwave imaging systems, the transmitters and receivers are arranged in multiple-input multiple-output (MIMO) configuration. In these systems, imaging is regarded as an inverse problem. For the solution of the inverse problem, the forward problem is required to be constructed with certain approximations. Among principal ones of these approximations is the low contrast assumption between the electrical properties of the object and the ambient medium. The object being in the far zone of the transducers and vice versa is another principal approximation. Although these approximations are crucial for the solution of the inverse problem, they limit the accuracy of the solution, because the approximations are often not realistic in representing the actual object properties and modeling the measurement setup. This thesis study presents three significant contributions in the field of near-field microwave imaging techniques. Firstly, for image reconstruction, an optimization problem involving the current density distribution and the dielectric and conductivity profile of the body is addressed using the alternating minimization technique. By handling the subproblems for each unknown variable separately and

utilizing total variation regularization, the proposed reconstruction method enables efficient and fast solutions for the inverse problem. Secondly, the study investigates the impact of different antenna polarizations and the number of antennas on imaging performance, a crucial aspect previously overlooked in experimental studies. The results demonstrate the potential of polarization diversity to enhance imaging results in space-constrained settings. Lastly, by efficiently utilizing near-field data obtained from full-wave analyses of antennas, the proposed methodology overcomes the computational complexity of full-wave solution approaches for the forward problem and allows for practical implementation in the image reconstruction process.

Keywords: Near Field Microwave Imaging, Forward Problem, Inverse Problem, Image Reconstruction, Polarization Diversity, Alternating Minimization

ÖZ

YAKIN ALAN MİKRODALGA GÖRÜNTÜLEME SİSTEMLERİNDE İLERİ VE GERİ PROBLEMLERİN ÇÖZÜMÜNE YÖNELİK YENİ BİR YAKLAŞIM

Dalkılıç, Akın
Doktora, Elektrik ve Elektronik Mühendisliği
Tez Yöneticisi: Doç. Dr. Lale Alatan
Ortak Tez Yöneticisi: Doç. Dr. Sevinç Figen Öktem Seven

Ağustos 2023, 126 sayfa

Günümüz yakın alan mikrodalga görüntüleme sistemlerinde, alıcı ve vericiler Çok Girdili Çok Çıktılı (ÇGÇÇ) konfigürasyonu ile düzenlenmektedir. Bu sistemlerde, görüntüleme bir ters problem olarak ele alınmaktadır. Ters problemin çözülebilir olması için ileri problemin bazı varsayımlarla oluşturulması gerekmektedir. Temel yaklaşımlardan biri, görüntülenecek cisim ile bulunduğu ortam arasındaki kontrast farkının az olduğunun varsayılmasıdır. Nesne ve görüntüleme sisteminin birbirlerinin uzak alanında olması da bir başka yaygın varsayımdır. Bu varsayımlar ters problemin çözümü için kritik olmalarıyla birlikte, çözümün doğruluğunu önemli bir şekilde kısıtlamaktadır. Çünkü, nesne özellikleri ve ölçüm modellemeleri genellikle gerçekçi olmamaktadır. Bu tez çalışması, yakın alan mikrodalga görüntüleme teknikleri alanında üç önemli katkı sunmaktadır. İlk olarak, akım yoğunluğu dağılımı ve dielektrik ve öziletkenlik profili arasında bir optimizasyon problemi, sıralı minimizasyon tekniği kullanılarak ele alınmaktadır. Karşılaşılan alt optimizasyon problemleri ayrı olarak ele alınıp, dielektrik ve iletkenlik profili için toplam değişim düzenlileştirmesi kullanılarak önerilen yöntem, ters problemin verimli ve hızlı çözülmesini sağlamaktadır. İkinci olarak, çalışma ile literatürde

şimdiye kadar göz ardı edilmiş olan farklı anten polarizasyonlarının ve anten sayısının görüntüleme performansı üzerindeki etkisi incelenmektedir. Sonuçlar, alansal olarak sınırlı ortamlarda görüntüleme performansını iyileştirmek için polarizasyon çeşitliliğinin potansiyelini göstererek önemli uygulamalı sonuçlar sunmaktadır. Son olarak, önerilen yöntem ile antenlerin tam dalga analizlerinden elde edilen yakın alan örüntüleri verimli bir şekilde kullanılmakta, hesaplama karmaşıklığı aşılmakta ve bu sayede görüntü geriçatımı işlemi için pratik bir şekilde uygulanması sağlanmaktadır.

Anahtar Kelimeler: Yakın Alan Mikrodalga Görüntüleme, İleri Problem, Ters Problem, Görüntü Geriçatımı

To all children..

ACKNOWLEDGMENTS

The author wishes to express his deepest gratitude to his supervisor Assoc. Prof. Dr. Lale Alatan and co-supervisor Assoc. Prof. Dr. Sevinç Figen Öktem Seven for their guidance, advice, criticism, encouragements, and insight throughout the research.

The author would also like to thank Prof. Dr. Mustafa Kuzuoğlu, Prof. Dr. S. Sencer Koç, Prof. Dr. Vakur B. Öztürk and Prof. Dr. Özlem Özgün for their participations in the thesis defence jury and providing valuable feedbacks about the thesis study.

The author would also like to thank Erdinç Erçil and Doğanay Doğan for their suggestions and comments.

I would like to thank Scientific and Technological Research Council of Turkey for providing financial support during the study under program TUBITAK 2211E.

For their understanding of me spending lots of time on this work, I sincerely thank my family.

TABLE OF CONTENTS

LIST OF TABLES

TABLES

LIST OF FIGURES

FIGURES

CHAPTER 1

INTRODUCTION

Microwave imaging of biological tissues has been an interesting topic for researchers over the past few decades [1]-[3]. The motivation behind the idea is to make use of the dielectric constant and conductivity difference between healthy and abnormal cells for the diagnosis of certain illnesses like breast cancer, brain stroke, etc. Microwave imaging has also found various application areas other than medical purposes such as surveillance, ground penetrating radars, behind-wall imaging systems and multi-layer dielectric material characterization [4]-[6]. Medical diagnosis is an attractive implementation area of microwave imaging for researchers since the malignant tissues are observed to have different electrical properties with respect to the healthy ones, as reported in [7] for brain tissues. The contrast difference is in terms of permittivity and/or conductivity of the tissues.

In this study, main focus will be on the detection of brain stroke. Brain stroke is the disturbance of the blood supply to the brain. There are two main types of brain strokes: ischemic and hemorrhagic. Ischemic stroke occurs due to the blockage of blood supply by thrombosis or embolism. If any vessel in the brain bursts, blood flows into the volume around the vessel and creates pressure. This type of stroke is called “hemorrhagic”. The first response paramedical teams have three hours to diagnose the type of the stroke and implement the appropriate treatment [8]. Therefore, it is very crucial to be able to diagnose the stroke and decide the type of it on site locations before the patient is carried to the hospital. Current imaging systems such as computed tomography (CT), magnetic resonance imaging (MRI), etc., are successful in detection and identification of stroke, however; these systems are not fast, cost effective, portable and accessible by paramedical emergency service

members. Microwave imaging is a powerful candidate which can fulfill all the aforementioned requirements that current systems cannot. Furthermore, microwave imaging uses non-ionizing radiation at a safe level of power which is not the case for CT that utilizes the ionizing harmful radiation.

A multi-input multi-output (MIMO) microwave imaging system consists of transmitter and receiver antennas placed around the region that needs to be imaged. Data from all receiver antennas are collected when one of the transmitter antennas is excited, and this procedure is repeated for all transmitter antennas and for all frequencies considered for the specific application. Then, this measured data is processed to obtain the dielectric constant and conductivity distribution within the imaging space. Data processing step involves two problems, namely forward and inverse problems. In the forward problem, given the dielectric constant and conductivity distribution of the imaging space, field values at receiver locations are computed when one of the transmitting antennas is excited. On the other hand, in the inverse problem, the dielectric constant and conductivity distribution is inferred from the measured data. It is obvious that the inverse problem requires the use of the forward problem. Therefore, a fast and accurate forward problem solver is one of the fundamental milestones of microwave imaging studies, since it is required for the formulation of the inverse problem and additionally provides “measured” field values in simulation environment without needing a real measurement setup. Another important role of having a powerful forward problem solver is that it enhances the performance of inverse problem solver since forward problem simulator can be used at any iteration step of the solution method.

The forward problem to be solved in microwave imaging systems is the scattering of EM fields in near field region due to 3D scatterer objects when numerical techniques like method of moments and finite element method are employed. The induced current density distribution in the scatterer object is required to be calculated in the forward problem since it is an intermediate step to determine the scattered fields. The equation to calculate the induced currents from the given geometry of the scatterer and the incident fields is called state equation, whereas the equation that relates the

scattered fields at receiver antenna locations to induced currents is called data equation.

In inverse problem solutions, Born approximation, which relies on replacing the total field with the incident field, is widely used during early studies in microwave imaging. By using Born approximation, the nonlinear inverse scattering problem takes a linear form such that the inter-relation between the unknowns is diminished. An iterative reconstruction method can be constructed where the total field at each iteration is approximated with scattered field calculated from the electrical parameters found in the previous iteration, and this method is called Born Iterative Method. General Born approximation assumes homogenous background. The distorted Born Iterative method studied in [31] and [32] assumes an inhomogeneous background and updates the background parameters at each iteration. This approach increases the convergence speed; however, it requires the update of Green's function at each iteration and increases the computational cost.

Back-projection algorithm is another image reconstruction technique that also linearizes the inverse problem by considering each point in the imaging space as an isolated point scatterer and neglecting multiple scattering between different cells of the distributed scatterer. In this approach, it is assumed that the normalized scattered signals are originated from a given point and if that pre-assumed scattering point does actually exist, a coherent summation of the signals results in large values, while, in other case, it gives a very small signal level which is considered as noise. By applying that calculation for each point on a 2D slice section, an image is obtained, and the existence and location of the scatterer can be estimated. The applications of this algorithm to brain imaging systems can be found in [12] and [14].

The confocal algorithm which is widely used to detect breast cancer tumors is a similar approach to back-projection algorithm. The main difference is the processing of time domain signals in the confocal algorithm [42], [61]. In this method, the backscattered signals at all antennas are time-shifted and added to create a synthetic

focus at each point in solution domain to identify the presence and location of strong scatterers.

Born iterative method, back-projection method and confocal algorithm are based on the linearization of the nonlinear inverse problem, however, some studies demonstrate that direct solution of the nonlinear problem provides better resolution for the same frequency range [7], [8]. In the direct solution of the nonlinear inverse problem, an optimization problem is defined to minimize the error between the signals measured at the receiver antennas and the computed scattered fields at the receiver antenna positions by using the data and state equations derived for the forward problem. Iterative Gauss-Newton algorithm and conjugate gradient algorithm are the widely used methods to solve this optimization problem and their applications to microwave imaging can be found in [16] and [60], respectively.

Note that, inverse problem is ill-posed due to the underdetermined nature of the problem since number of measured data is usually much smaller than the number of cells in the imaging domain, which requires the utilization of regularization methods to improve the conditioning of the problem. Tikhonov and Total Variation (TV) regularization methods are widely used in microwave imaging applications since both of them make use of the continuity of the electrical properties of the scatterer as prior information. Tikhonov regularization uses ℓ_2-norm of the gradient of the dielectric constant and conductivity profile, whereas TV considers ℓ_1-norm of it. This difference results in a smoothing effect for Tikhonov regularization. Consequently, TV regularization is more preferred when the application requires to preserve edge discontinuities. A comparison of these regularization techniques applied in the image reconstruction procedure in order to smooth the created image while preserving the edges is studied in [28] by V. L. Coli, et. al. In their study, it is stated that the relative error for dielectric properties distribution is significantly decreased with the implementation of regularization.

In the next section, the studies in the literature on microwave imaging of brain will be presented.

1.1 Literature Review

Chronogically, research in the literature regarding microwave imaging of brain can be classified into three groups, which are listed as,

1. Feasibility studies
2. Experimental studies
3. Machine-Learning based studies

Each group will be discussed in the following subsections.

1.1.1 Feasibility Studies

At the beginning period of utilizing microwave imaging for brain stroke detection, a couple of feasibility studies are reported in [7], [9] and [10] . In [7], Semenov S. and Corfield D. utilized microwave tomography (MWT) simulations on a simplified 2D head model (see Fig.1). They suggest 0.5-1 GHz frequency band for the optimal operation. Moreover, they demonstrate the feasibility of microwave imaging for stroke detection via multi-frequency reconstruction which results in fairly better images when compared to single frequency implementation. They also noted that low frequency implies low resolution in classical far-field sense, however; non-linear near field imaging approaches for brain imaging are proposed as candidates for super-resolution images. Another super-resolution image reconstruction study by M. A. Ali and M. Moghaddam [8] also indicates that utilizing non-linear formulation, creates an inherent super resolution since the multiple scattering effects are taken into account at each reconstruction iteration.

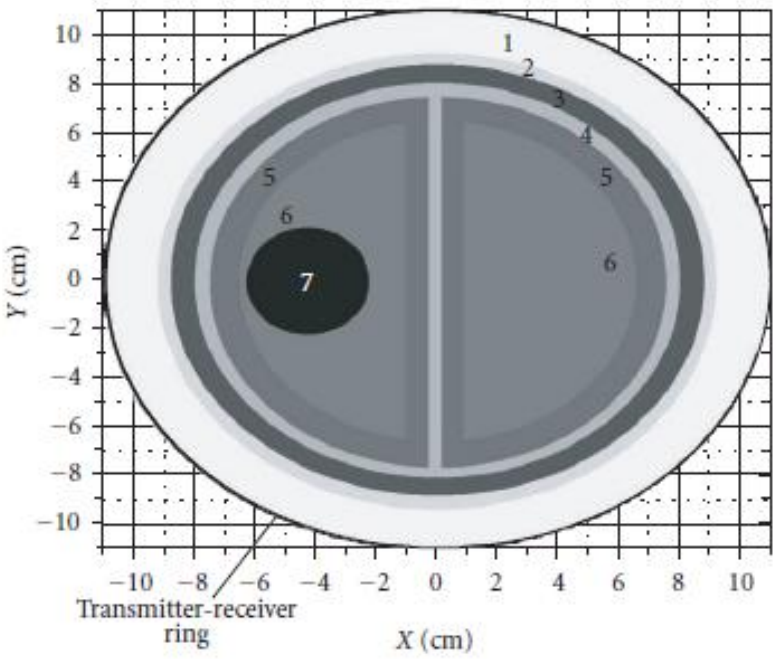

Figure 1.1. 2D simplified head model with brain stroke [7]

In [9], Ireland D. and Bialkowski M. held a study using a realistic 3D head phantom and Finite Difference Time Domain (FDTD) method. The anatomically realistic head phantom in the study is obtained from [11] and will be utilized for this thesis study.

Another feasibility study by Scapaticci R., et.al. achieved successful image reconstruction from different 2D cuts of the brain for both ideal and non-ideal (noisy) conditions in simulation environment [10]. The study also demonstrates the matching medium requirements and forbidden frequency zones with the help of simple transmission line model of multi-layer structure of the brain aiming the maximization of the energy penetrated into the head. It is also stated that the resolution of the images is related to the wavelength in the matching medium at corresponding frequency, not to the one in free space.

1.1.2 Experimental Studies

Examples of experimental systems for brain imaging can be found in [12]-[20].

A real experimental system implementation with a realistic 3D head phantom is held in [12] by Mobashsher A.T. and Abbosh A. They built a wideband (1.1-3.4 GHz) system with a unidirectional antenna, a transceiver and image reconstruction and signal processing algorithms as shown in Figure 1.2. The head is rotated, and measurements are done at 32 separate positions on a full circle. Back-projection algorithm is applied for image reconstruction and the quality of the images is poor and the identification of the stroke is not possible without having the knowledge (image) of the healthy brain. The calibration procedure detailed in [12] is important for the removal of errors originating from measurement environment. Finally, they emphasize the time-domain characterization/performance control (fidelity factor) of the radiated pulse of the antenna for near-field operations.

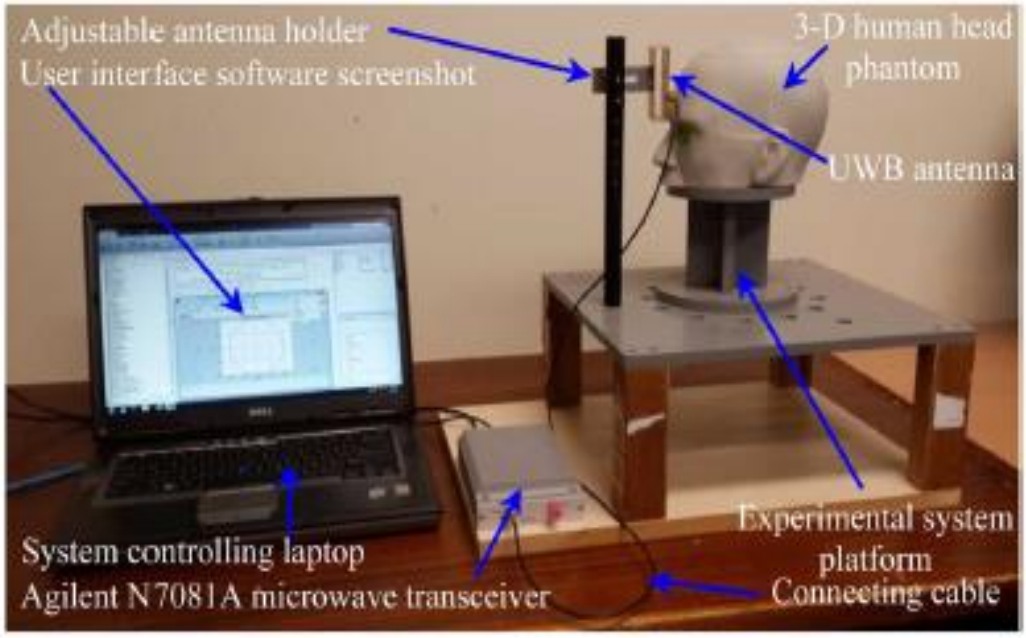

Figure 1.2. Head imaging system constructed in [12]

Another microwave system construction is conducted by Mohammed B. J., et. al. for head imaging in [13]. They prepared a realistic head phantom and configured a

platform that integrates a circular array of 16 exponentially corrugated tapered slot antennas operating in the band from 1 GHz to 4 GHz into the system. The back-scattered signals are collected and transformed into time domain as an input to the confocal algorithm. The images obtained by the study are observed to be limited by the capability of the confocal algorithm.

A portable microwave imaging system that applies back-projection algorithm in order to construct the image of the head is reported in [14] by Mobashsher A.T., Mahmoud A. and Abbosh A. The wideband (0.75 and 2.55 GHz) signals gathered from the system are transformed from frequency domain to time domain and delay-and-sum back projection algorithm is utilized. The system includes a single wideband antenna and a realistic head phantom rotating on a platform such that reflection measurements are repeated at equiangular positions and used for the detection of the brain stroke. The radiation safety considerations are also examined in [14] and it is observed that the power emitted into the body is at a harmless level.

A flexible cap is designed and fabricated by Alqadami A. S. M., et. al. in [15] in pursuance of a wearable microwave imaging system, which reduces the mismatch between the skin and antenna array by introducing a flexible high-permittivity matching layer, for the detection of brain stroke. The system consists of 16 antennas operating in 0.6-2.5 GHz frequency band. Images obtained in the study are observed to be satisfying in detection of brain stroke.

An experimental setup that has 20 point sources placed on a circular array operating in the frequency band from 0.4 to 1.2 GHz is constructed by Bisio I., et. al. in [16] in order to retrieve the differential dielectric map of the human head which is generated due to increasing size of the stroke by time.

In [17], Scapaticci R., et. al. present the design procedure of a low-complexity microwave imaging system for brain stroke monitoring so as to clarify the optimum parameters for the system like array configuration, positioning, number and polarizations of antennas. The findings of this study indicate that a microwave imaging system consisting of 24 antennas evenly distributed on a helmet at

approximately $0.4\lambda_g$ distance, where λ_g represents the wavelength in the matching medium, successfully meets the design requirements and effectively accomplishes the desired imaging objective.

In [18] by Rodriguez-Duarte D. O., et. al., an experimental setup is designed and produced with an array of 22 antennas ellipsoidally placed around the head as shown in Figure 1.3 in order to obtain the differential scattering parameters to form the reconstructed images, resulting from the progressive expansion of a stroke over time. A multifrequency imaging algorithm is utilized with data gathered within the frequency range of 0.8 to 1 GHz.

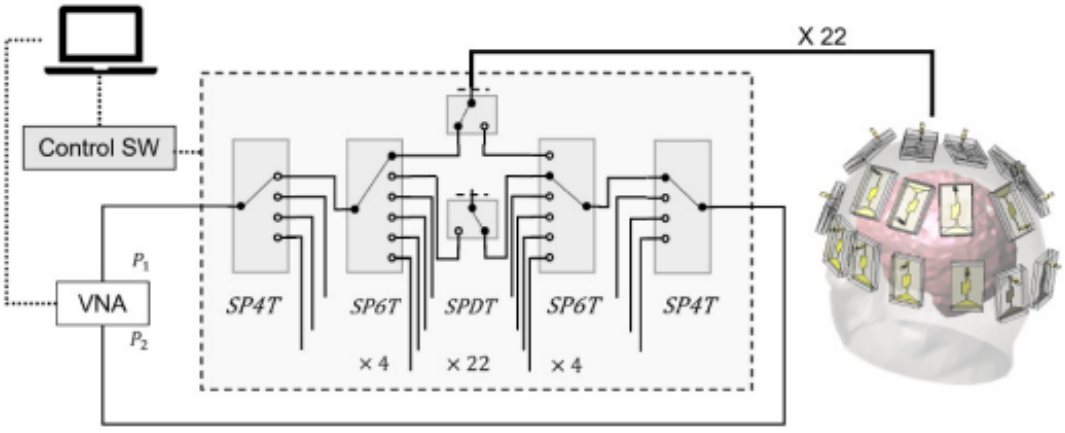

Figure 1.3. Hardware configuration of the suggested prototype in [18]

Statistical data taken from S-parameter measurements of the antennas around the head is utilized for the detection of brain atrophy due to Alzheimer's disease and reported in [19] by Saied I. M. and Arslan T.

The importance of the pre-processing techniques at experimental imaging systems is demonstrated in [20] by Mustafa S., Mohammed B., and Abbosh A. The strong background reflection on a measured set of data is eliminated with two different pre-processing techniques and results are compared with the original case where no pre-processing implementation is held. The image quality is observed to increase with the techniques detailed in the paper.

Compressive sensing application in microwave imaging for brain stroke detection in [21] is considered in order to reduce number of frequency and recover time domain correlation (TDC) signals from these decreased frequency points. Then, the confocal algorithm is utilized for image reconstruction from recovered TDC signals. They reported that the same image quality is obtained with half the number of frequency points.

1.1.3 Machine-Learning Based Studies

Machine-Learning algorithms are applied for microwave imaging problems in order to increase the speed and provide the image reconstruction which is not feasible for systems utilizing iterative or direct forward and inverse problem solutions of near field radiation and scattering formulizations ([22]-[26]). Convolutional Neural Network (CNN) based image reconstruction algorithms are studied as in [26] by Chen G., et. al. that utilizes CNN as an assisting tool in order to increase the performance of the microwave imaging algorithm.

The first clinical study is held by Persson, et. al. [27] with two prototype systems which are shown in Figure 1.4. They analyzed the measurements from the patients with known conditions with a machine-learning algorithm and created subspaces for signals that correspond to healthy, ischemic and hemorrhagic stroke conditions. With these prototypes, they can differentiate hemorrhagic and ischemic strokes and diagnose for the hemorrhagic stroke. However, the success of the prototypes with a 99.9% sensitivity is around 30%, which is not acceptable for a diagnosis tool.

A complete review by J. Liu, et. al in [59] on the current state of the aforementioned microwave imaging systems for brain stroke detection clearly indicates that all these methods are still in the early stages of development, and promising potential for future investigations. Moreover, the common point that all these techniques suffer from is discussed to be the lack of accurate and high-resolution stroke images. This deficiency is claimed to be due to shortage of smart unification of analysis methods

in the forward problem and the image reconstruction algorithms in the inverse problem.

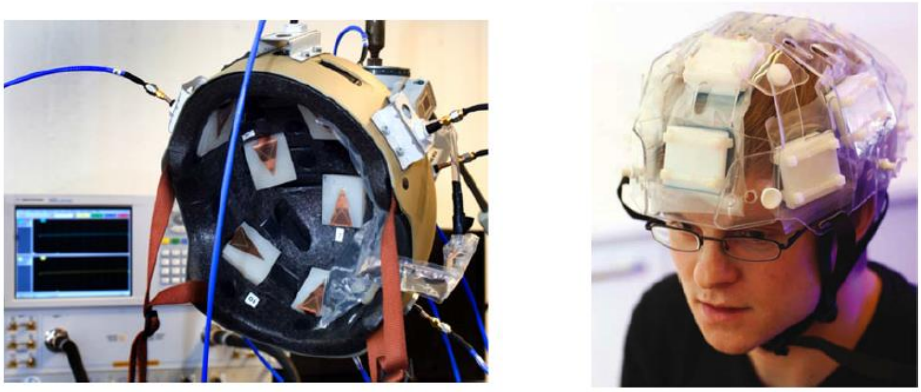

Figure 1.4. Prototype stroke detection systems used in first clinical studies [27]

1.2 Contributions of This Thesis

In this thesis, the core topic is the detection of brain strokes using a near field microwave imaging system. The well-defined forward and inverse problem structures will be the key points to increase the accuracy and quality of the images. There exist many microwave imaging systems developed by researchers as described and detailed in the previous sections of this chapter. During the implementation phase, almost all of these systems have some disadvantageous points, as far as the author's knowledge, like being bulky, slow in creating the image or detecting the abnormality, high error rate for false detection, etc. Furthermore, there is no specific study that incorporates the radiation characteristics of antenna into the image reconstruction algorithm in order to construct a realistic model that considers all practical parameters of the realized system. This thesis study also refers to the original works of the authors in [73].

Three main contributions of this thesis study are summarized as:

Within the scope of the thesis study, for image reconstruction, we address an optimization problem involving two variables: the current density distribution and

the dielectric and conductivity profile of the body. While previous research studies approached the problem with a single optimization or functional to minimize, we adopted the alternating minimization technique. In alternating minimization method, two independent optimization problems for the current density and dielectric and conductivity profiles are handled separately. At each solution step, the output of one inner step is used as input for the other step. Consequently, the size of the optimization problems is reduced, which results in more efficient and fast solution of the inverse problem. The minimization problem solved for the current density distribution incorporates terms from both the "state" and "data" equations, with a weighting coefficient between them. Due to the larger number of equations, the problem becomes well-conditioned, and it does not require regularization. Conjugate gradient method is used to solve this optimization problem.

To tackle the ill-conditioned nature of the minimization problem corresponding to the dielectric and conductivity profile variable, we incorporated total variation regularization. This regularization method aids in stabilizing the optimization process and enhancing the robustness of the results. Among different optimization techniques, which are recently proposed to solve ill-conditioned optimization problems, constrained split augmented Lagrangian shrinkage algorithm (C-SALSA) is chosen to be implemented for its efficiency. In this context, our contribution lies in employing alternating minimization in conjunction with the contemporary solution technique C-SALSA. By combining these approaches, we achieve improved accuracy and efficiency in solving the ill-conditioned inverse problem, making our methodology an innovative and valuable addition to the field.

In the course of conducting a comprehensive literature review, our research focused on a collection of studies presented under the "Experimental Studies" section which reveals that all of these studies have one common aspect: they are all based on the utilization of single-polarized antennas. This observation prompted us to explore the potential impact of different antenna polarization types and number of antennas on the overall imaging performance, a crucial aspect ignored in previous studies. We conducted a thorough investigation on the effects of variations on antenna

polarizations within the framework of this thesis. Our goal was to make it clear how polarization diversity and the number of antennas might influence the imaging outcomes. For this purpose, we set up an extensive array of experiments, comparing and analyzing the imaging results obtained from different polarization setups. One of the primary motivations behind this focused topic was to assess the feasibility of reducing the overall number of antennas while still maintaining satisfactory imaging performance. Upon the conclusion of our investigations, we arrived at some remarkable insights that have not been previously reported in the literature. The most notable revelation was that, when N dual-polarized antennas were employed, a noticeably better imaging performance was achieved in comparison to the scenario where 2N single-polarized antennas were used. It should also be noted that these two scenarios have exactly the same computational load for the image reconstruction algorithm developed in this thesis. This observation holds significant implications for the field, as it highlights the potential of polarization diversity and its remarkable effect in enhancing imaging results compared to spatial diversity. The significance of our findings possesses practical implications as well. We realized that the constraints related to the limited number of antennas that could be feasibly placed on the surface of the human head, often a challenge in practical imaging scenarios, could be effectively overcome by adopting dual-polarized antenna structures. This contribution represents important progress in antenna-based imaging techniques, opening up new possibilities for challenging and constrained settings with a powerful tool to achieve improved imaging results in real-world applications.

In [45] and [62] detailed full-wave analyses of the imaging system together with the antennas are conducted. Their primary aim was to obtain realistic measured data within a simulation environment. The acquisition of such measured data is crucial for validating and benchmarking imaging algorithms and techniques; however, it is important to note that these analyses were not directly utilized for image reconstruction purposes due to the considerable computational load caused by the inclusion of the antennas into the simulation model. This computational complexity limits its practical implementation in iterative image reconstruction algorithms,

where multiple iterations are required for accurate and detailed image reconstruction. Consequently, employing their forward model approach in each iteration of the inverse problem is infeasible, prompting the search for an alternative and more efficient solution. Therefore, our research is focused on finding a novel formulation that could efficiently incorporate the near-field data obtained from individual antennas by full-wave analyses into the forward model and utilize it in the image reconstruction step. By combining the scattered field data and the near field pattern of antennas thorough reaction theorem, we compute port voltage values [63]. The incorporation of the induced port voltages, rather than the scattered field values, into our imaging algorithm enabled us to effectively use the near-field data, obtained from the full-wave analyses of isolated antennas, in the process of reconstructing the final images.

In conclusion, our research not only highlighted the significance of employing realistic measured data obtained from antenna analyses in simulation environments but also provided a crucial solution to overcome the computational challenges in the image reconstruction process.

This thesis is organized in the following manner:

In Chapter 2, the forward problem part of the microwave imaging algorithm is explained together with formulations for the state and data equations of the specific problem handled in the thesis study.

Chapter 3 is devoted to the inverse problem related topics including the definition of the problem, formulation of the optimization problem with an appropriate cost function, developed solution approach using alternating minimization and C-SALSA and details of the implementation of the imaging algorithm.

In Chapter 4 of the thesis, a thorough and comprehensive exploration is presented, focusing on image reconstruction operations using Hertzian dipole antennas. This investigation employs various scenarios associated with antenna polarization diversity. Moreover, the chapter examines the configuration of dual-polarized

Hertzian antennas placed around a realistic head model. The results obtained from this examination are also detailed within the same chapter.

In Chapter 5, microwave imaging results are obtained for the scenario where the antenna model is incorporated into the imaging system. The imaging is performed using the developed formulation taking into account the port voltage (S-parameter) values, and the related examinations and evaluations are presented. The results with antennas are thoroughly analyzed and discussed within this chapter.

In Chapter 6, the thesis is concluded with final remarks, providing a brief summary of the key topics covered throughout the study.

CHAPTER 2

FORWARD PROBLEM

In literature, there are numerous studies on forward problem solution techniques starting from the early fundamental ones towards up-to-date advanced applications [34]-[49].

Method of Moments (MoM) technique is one of the major solution techniques which enables the handling of integral equations related to field expressions of electromagnetic scattering and implemented by various researchers [34]-[41]. In [34], Livesay and Chen use tensor integral equation solution by 3D MoM technique for the determination of electromagnetic fields induced in biological bodies which are modeled by cubic mesh elements. They give derivation of the tensor integral equation and matrix formulation for MoM application together with the details regarding principal value, singularity and uniqueness problems. Tetrahedral modeling is introduced by Schaubert et.al. in [35] for the electromagnetic scattering problem solution from inhomogeneous bodies. Tetrahedral elements bring flexibility in modeling of arbitrary volumetric shapes. Special basis functions are also defined to ensure the continuity of electric flux density at adjacent faces of tetrahedral elements. Another technique by Tsai et. al. for the realistic modeling of 3D volumetric dielectric objects is the utilization of polyhedral elements with MoM [36]. In their study, Modified Galerkin's Approach is also introduced in order to decrease the computation time with an increased accuracy with respect to the original Galerkin's method. Volume Integral Equation (VIE) is used for the solution of scattering problems of both 2D and 3D high-permittivity dielectric objects in [38] by Kottman and Martin. Their study introduces a novel formalism technique which is independent of the basis type and removes the singularity of Green's tensor that

results accurate calculations of the scattered electromagnetic field due to high permittivity materials.

Fast Multipole Method (FMM) is an integral-based computational technique developed by Rokhlin and Greengard [69]-[70]. There exist several studies that utilize FMM in solving forward and inverse problems related to microwave imaging as in [71]-[72].

Finite-Difference Time-Domain (FDTD) is another major forward problem solution method widely used in microwave imaging algorithms which require time domain electromagnetic fields like confocal algorithm [42], nonlinear super-resolution algorithm [43], etc. In [42] Li and Hagness simulated the scattering of 2D realistic breast model with cancer tumor illuminated by a monopole array of 18 elements using FDTD method. Afterwards, the backscattered signals at all antennas are time-shifted and added to create a synthetic focus at each point in solution domain. With this approach, they attempt to identify the presence and location of strong scatterers (breast cancer tumor in this case), not to reconstruct the complete dielectric profile. Nonlinear super-resolution imaging study by Ali and Moghaddam [43] utilizes 3D FDTD method for both forward and inverse problem solutions. It brings super-resolution results since the method takes multi-reflections into account.

Finite Element Method (FEM) is also applied in microwave imaging simulations in [44] and [45], where scattered near zone fields are calculated using FEM and then used in inverse problem solution as measured fields.

The forward problem in the scope of this thesis study can be demonstrated with a simple model as shown in Figure 2.1. In that model, there exist a transmitting antenna and 3D scatterer object as the known parts of the problem. The measurement set (E-field intensity values or port voltage values or S-parameters, etc.) at observation points, namely receiver points, is the main unknown of the problem.

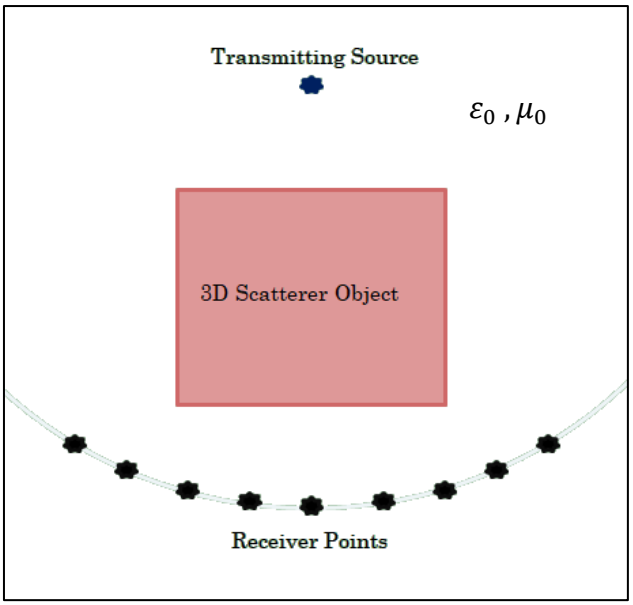

Figure 2.1. Forward problem model for 3D EM scattering

The integral equation for the scattered field, caused by the currents induced in the object ($\bar{J}_{eqv}$) is given by

$$\bar{E}_s(\bar{r}) = \int_v \bar{\bar{G}}(\bar{r},\bar{r}') \cdot \bar{J}_{eqv}(\bar{r}')dv' \tag{1}$$

where,

$$\bar{\bar{G}}(\bar{r},\bar{r}') = -j\omega\mu_0 \left[\bar{\bar{I}} + \frac{1}{{k_0}^2}\nabla\nabla\right]\psi(\bar{r},\bar{r}') \tag{2}$$

$$\psi(\bar{r},\bar{r}') = \frac{\exp(-jk_0|\bar{r}-\bar{r}'|)}{4\pi|\bar{r}-\bar{r}'|} \tag{3}$$

$$k_0 = \omega\sqrt{\mu_o\varepsilon_0} \tag{4}$$

$$\bar{J}_{eqv}(\bar{r}) = \tau\bar{E}_t(\bar{r}) \tag{5}$$

$\bar{\bar{I}}$ is the unit dyad (idemfactor) and τ is the electrical properties parameter which is given as:

$$\tau(\bar{r}) = \sigma(\bar{r}) + j\omega\varepsilon_0(\varepsilon_r(\bar{r}) - 1) \tag{6}$$

where σ is conductivity, ε_r is relative permittivity of the volumetric scatterer body. The convention for time dependence in this study is taken as $e^{j\omega t}$ where $\omega = 2\pi f$ and f is the operation frequency. Note that, the first del operator (∇) in equation (2) is not divergence operator. Therefore, dot product sign is not used between two consecutive del operators. After the application of the second del operator, we obtain a vector. Then, the first del operator acts on each component of this vector, resulting in a dyadic.

Furthermore, $\bar{E}_t$ in equation (5) is the total electric field inside the dielectric object which can be written as:

$$\bar{E}_t(\bar{r}) = \bar{E}_i(\bar{r}) + \bar{E}_s(\bar{r}) \tag{7}$$

where $\bar{E}_i$ is the incident electrical field value created by the source in the absence of scatterer.

Combining equations (1), (5) and (7), we obtain

$$\int_v \bar{\bar{G}}(\bar{r},\bar{r}') \cdot \bar{J}_{eqv}(\bar{r})dv - \frac{\bar{J}_{eqv}(\bar{r})}{\tau} = -\bar{E}_i(\bar{r}) \tag{8}$$

By applying MoM algorithm detailed in [34], and presented in the next section of this chapter, equation (8) will be transformed into a matrix equation which is generally referred as the state equation. Before presenting the matrix equation, some variables will be defined to introduce the notation from continuous variables to discrete variables adopted throughout this thesis. To apply MoM, the scatterer region is divided into N cubic cells. Incident electric field and induced current vectors computed at the center of nth cell ($\bar{r}_n$) can be expressed as follows by using the discrete variables denoted by small letters.

$$\bar{E}_i(\bar{r}_n) = e^i_{xn}\,\hat{a}_x + e^i_{yn}\,\hat{a}_y + e^i_{zn}\,\hat{a}_z \tag{9}$$

$$\bar{J}_{eqv}(\bar{r}_n) = j^{eqv}_{xn}\hat{a}_x + j^{eqv}_{yn}\hat{a}_y + j^{eqv}_{zn}\hat{a}_z \tag{10}$$

The incident electric field intensity and induced current vectors are defined by using the above discrete variables as:

$$[e^i] = \begin{bmatrix} e^i_{x1} \\ \vdots \\ e^i_{xN} \\ e^i_{y1} \\ \vdots \\ e^i_{yN} \\ e^i_{z1} \\ \vdots \\ e^i_{zN} \end{bmatrix}_{3Nx1} \qquad [j^{eqv}] = \begin{bmatrix} j^{eqv}_{x1} \\ \vdots \\ j^{eqv}_{xN} \\ j^{eqv}_{y1} \\ \vdots \\ j^{eqv}_{yN} \\ j^{eqv}_{z1} \\ \vdots \\ j^{eqv}_{zN} \end{bmatrix}_{3Nx1} \tag{11}$$

$\tilde{\tau}$ and $\tilde{\tau}'$ vectors are defined as follows in terms of the inverse of τ values at the center of nth cell (τ_n^{-1}),

$$[\tilde{\tau}] = \begin{bmatrix} \tau_1^{-1} \\ \vdots \\ \tau_N^{-1} \end{bmatrix}_{Nx1} \quad , \qquad [\tilde{\tau}'] = \begin{bmatrix} \tilde{\tau} \\ \tilde{\tau} \\ \tilde{\tau} \end{bmatrix}_{3Nx1} \tag{12}$$

and finally, diagonal matrices, $\tilde{\tau}_{\,diag}$ and $\tilde{\tau}'_{diag}$, are defined as:

$$\left[\tilde{\tau}_{\,diag}\right] = \begin{bmatrix} \tilde{\tau}_1 & 0 & 0 \\ 0 & \ddots & 0 \\ 0 & 0 & \tilde{\tau}_N \end{bmatrix}_{NxN} , \left[\tilde{\tau}'_{diag}\right] = \begin{bmatrix} \tilde{\tau}'_1 & 0 & 0 \\ 0 & \ddots & 0 \\ 0 & 0 & \tilde{\tau}'_{3N} \end{bmatrix}_{3Nx3N} \tag{13}$$

For the sake of completeness, it is appropriate to define the reciprocal counterparts of the above vectors and matrices in terms of electrical properties parameter τ as:

$$[\tau] = \begin{bmatrix} \tau_1 \\ \vdots \\ \tau_N \end{bmatrix}_{Nx1} \quad , \qquad [\tau'] = \begin{bmatrix} \tau \\ \tau \\ \tau \end{bmatrix}_{3Nx1} \tag{14}$$

$$\left[\tau_{\,diag}\right] = \begin{bmatrix} \tau_1 & 0 & 0 \\ 0 & \ddots & 0 \\ 0 & 0 & \tau_N \end{bmatrix}_{NxN} , \left[\tau'_{diag}\right] = \begin{bmatrix} \tau'_1 & 0 & 0 \\ 0 & \ddots & 0 \\ 0 & 0 & \tau'_{3N} \end{bmatrix}_{3Nx3N}$$

G^S matrix which is related to dyadic Green's function for state equation is defined as:

$$[G^S] = \begin{bmatrix} G^S_{xx} & G^S_{xy} & G^S_{xz} \\ G^S_{yx} & G^S_{yy} & G^S_{yz} \\ G^S_{zx} & G^S_{zy} & G^S_{zz} \end{bmatrix}_{3Nx3N} \tag{15}$$

entries of which will be given in the next section.

By using all definitions of discrete variables, the state equation can be expressed in matrix form as follows,

$$\left([G^S] - [\tilde{\tau}'_{diag}]\right)[j^{eqv}] = -[e^i] \tag{16}$$

After determining equation (16), which can be solved for the unknown induced current density j_{eqv}, the next step in the forward problem solution is to obtain the data equation which gives the radiated E-field intensity values at observation points, namely, the measured signals. By utilizing the volume equivalence theorem, we have equivalent current sources at dielectric object positions radiating into free space. Radiated scattered electrical field intensity values at observation points can be calculated as,

$$\bar{E}_{obs}(\bar{r}) = \iiint \bar{\bar{G}}(\bar{r},\bar{r}') \cdot \bar{J}_{eqv}(\bar{r}')\, dv' \tag{17}$$

where $\bar{\bar{G}}$ is free space Dyadic Green's function defined in equation (2). It can be written in the following compact form,

$$\begin{aligned}\bar{\bar{G}}(\bar{r},\bar{r}') &= -j\omega\mu \left[\bar{\bar{I}} + \frac{1}{k^2}\nabla\nabla\right] g(R) \\ &= -j\omega\mu \left\{\left(\frac{3}{k^2R^2} + \frac{3j}{kR} - 1\right)\hat{R}\hat{R} + \left(1 - \frac{j}{kR} - \frac{1}{k^2R^2}\right)\bar{\bar{I}}\right\} g(R)\end{aligned} \tag{18}$$

where $g(R) = \frac{e^{-jkR}}{4\pi R}$ and $R = |\bar{r} - \bar{r}'|$

Similar to the procedure presented for state equation, discrete variables for data equation need to be defined. The electric field observed at the mth receiver location can be written as:

$$\bar{E}_{obs}(\bar{r}_m) = e_{xm}^{obs}\hat{a}_x + e_{ym}^{obs}\hat{a}_y + e_{zm}^{obs}\hat{a}_z \tag{19}$$

The observed electric field vector for M receivers can be written as:

$$[e^{obs}] = \begin{bmatrix} e_{x1}^{obs} \\ \vdots \\ e_{xM}^{obs} \\ e_{y1}^{obs} \\ \vdots \\ e_{yM}^{obs} \\ e_{z1}^{obs} \\ \vdots \\ e_{zM}^{obs} \end{bmatrix}_{3Mx1} \tag{20}$$

and the Green's function matrix corresponding to data equation is defined as:

$$[G^D] = \begin{bmatrix} G_{xx}^D & G_{xy}^D & G_{xz}^D \\ G_{yx}^D & G_{yy}^D & G_{yz}^D \\ G_{zx}^D & G_{zy}^D & G_{zz}^D \end{bmatrix}_{3Mx3N} \tag{21}$$

where G_{pq}^D (p=*x, y or z* and q=*x, y or z*) are sub-matrices with (m,n)th entry corresponding to the value of the Green's function given in equation (18) evaluated at the position of mth receiver due to a source at the nth cell.

By approximating the volume integral given in equation (17) by multiplication with the volume of the unit cell (ΔV), equation (17) can be written in matrix form as:

$$[T][j^{eqv}] = [e^{obs}] \tag{22}$$

where T is radiation matrix whose elements are given as:

$$T_{mn} = \Delta V G_{mn}^D \tag{23}$$

Matrix representation given in (22) completes the data equation part of the forward problem solution.

2.1 Solution of Forward Problem Via Method Of Moments

2.1.1 Method of Moments (MoM) Basics

In this section, a brief summary of Method of Moments (MoM) basics is presented. MoM is a general procedure for the solution of linear inhomogeneous equations ([50],[51]) in the form of

$$L(f) = g \tag{24}$$

where L is a known linear operator, g is a known function and f is the function to be determined. In MoM, first, f is converted into a series sum of known functions called "basis" in the domain L,

$$f \cong \tilde{f} = \sum_{n} \alpha_n f_n \tag{25}$$

where α_n's are constants and f_n's are basis functions. Next, the series sum approximation of f is inserted into equation (24) and the below equation is obtained by making use of the linearity of the operator,

$$\sum_{n=1}^{N} \alpha_n L f_n \cong g \tag{26}$$

Finally, the residual, difference between approximate and exact unknown function f, is minimized with a suitable inner product and weighting function set resulting below equation,

$$\sum_{n=1}^{N} \alpha_n \langle w_m, L f_n \rangle = \langle w_m, g \rangle \tag{27}$$

Equation (27) can be written in matrix form as:

$$[Z][\alpha] = [g] \tag{28}$$

where,

$$[Z] = \begin{bmatrix} \langle w_1, Lf_1 \rangle & \langle w_1, Lf_2 \rangle & \cdots & \\ \langle w_2, Lf_1 \rangle & \ddots & & \vdots \\ \vdots & & \cdots & \langle w_M, Lf_N \rangle \end{bmatrix} \quad (29)$$

$$[\alpha] = \begin{bmatrix} \alpha_1 \\ \alpha_2 \\ . \\ . \\ . \\ \alpha_N \end{bmatrix} \quad \text{and} \quad [g] = \begin{bmatrix} \langle w_1, g \rangle \\ \langle w_2, g \rangle \\ . \\ . \\ . \\ \langle w_M, g \rangle \end{bmatrix} \quad (30),(31)$$

α vector can be calculated from equation (28) by using direct inverse of (29) or iterative calculation methods like conjugate gradient, etc. Once α is determined, it is incorporated into (25) and approximate f is obtained with the help of basis functions.

2.1.2 Implementation of MoM for the Solution of Forward Problem

The forward problem to be solved in this study is the scattering of EM fields in near field region due to 3D dielectric objects. This problem is first handled in [34] using cubic mesh elements and plane wave incidence in order to calculate the field intensities induced in biological bodies via Method of Moments. The basis functions in [34] are pulse functions and impulse function is chosen as testing function (point matching method). Following the solution steps starting with the definition of tensor integral equation for the scattered field and detailed in [34], the entries of the Green's matrix for state equation (G^S) in (16) are obtained for the non-diagonal terms as:

$$G_{pq}^S(m,n) = \frac{-j\omega\mu_0 k_0 \Delta V_n \exp(-j\alpha_{mn})}{4\pi\alpha_{mn}^3}[(\alpha_{mn}^2 - 1 - j\alpha_{mn})\delta_{pq} + \cos\theta_p^{mn}\cos\theta_q^{mn}(3 - \alpha_{mn}^2 + 3j\alpha_{mn})], \; m \neq n \quad (32)$$

where

$$\alpha_{mn} = k_0 R_{mn} \qquad R_{mn} = |\bar{r}_m - \bar{r}_n|$$

$$\cos\theta_p^{mn} = \frac{(p_m - p_n)}{R_{mn}} \quad \cos\theta_q^{mn} = \frac{(q_m - q_n)}{R_{mn}}$$

$$\bar{r_m} = (x^m, y^m, z^m) \quad \bar{r_n} = (x^n, y^n, z^n)$$

while the diagonal terms are given by

$$G_{pq}^S(n,n) = \delta_{pq}\left[\frac{-j2\omega\mu_0}{3k_0^2}\left\{e^{-jk_0a_n}(1+jk_0a_n)-1\right\} - \frac{1}{j3\omega\epsilon_0}\right] \tag{33}$$

where,

$$\alpha_n = \left(\frac{3\Delta V_n}{4\pi}\right)^{1/3} \tag{34}$$

Equations (32) and (33) can be combined in order to retrieve coupled Green's matrix G_{pq} and modifying equation (16) the matrix form below is determined as:

$$\left[G_{pq}\right]_{NxN} = \left[G_{pq}^S\right]_{NxN}\left[\tau_{diag}\right]_{NxN} - [I]_{NxN}\delta_{pq} \quad ; p,q=x,y,z \tag{35}$$

where I is an N-by-N identity matrix and τ_{diag} was defined in equation (14). Arranging (35) for all values of p and q, we obtain

$$[G]_{3Nx3N} = [G^S]_{3Nx3N}\left[\tau'_{diag}\right]_{3Nx3N} - [I]_{3Nx3N} \tag{36}$$

Final linear matrix equation given in [34] is

$$[G][e_t] = -[e_i] \tag{37}$$

where e_t is total electrical field intensity vector inside the object, given as:

$$[e^t] = \begin{bmatrix} e_{x1}^t \\ \vdots \\ e_{xN}^t \\ e_{y1}^t \\ \vdots \\ e_{yN}^t \\ e_{z1}^t \\ \vdots \\ e_{zN}^t \end{bmatrix}_{3Nx1} \tag{38}$$

Inserting (36) into (37), equation (39) is determined,

$$\left\{[G^S]_{3Nx3N}[\tau'_{diag}]_{3Nx3N} - [I]_{3Nx3N}\right\}[e_t]_{3Nx1} = -[e_i]_{3Nx1} \tag{39}$$

Afterwards, by modifying (39), equation (40) is obtained as:

$$\left\{[G^S]_{3Nx3N} - \left[\tilde{\tau}'_{diag}\right]_{3Nx3N}\right\}\left[\tau'_{diag}\right]_{3Nx3N}[e_t]_{3Nx1} = -[e_i]_{3Nx1} \qquad (40)$$

Combining equations (5) and (40), the matrix form of state equation (16) of the forward problem is obtained in (41) and completes the derivation steps as,

$$\left\{[G^S]_{3N\,x\,3N} - \left[\tilde{\tau}'_{diag}\right]_{3Nx3N}\right\}[j_{eqv}]_{3N\,x\,1} = -[e_i]_{3Nx1} \qquad (41)$$

The solution process can be started after evaluating all elements of G^S matrix using above equations (32) and (33). The current density at each evaluated point can be obtained (from matrix form equation) by direct matrix solution or iterative inversion methods.

2.1.3 Verification of Forward Problem Solver

The forward problem solution detailed above is implemented using MATLAB under different conditions and the results are compared to the ones given in [34] and [52]. Furthermore, scattering by inhomogeneous objects are realized in MATLAB and the determined field values are compared to ANSYS HFSS simulation results. As a first verification step of the 3D EM scattering forward problem solver code, Sadiku's animal head model [52], which is an approximated sphere constructed by cubic mesh elements (see Figure 2.2), is tested and the normalized power distributions at sample positions along the principal axes are shown in Figure 2.3 together with the original work. As seen from Figure 2.3, the results are consistent with each other.

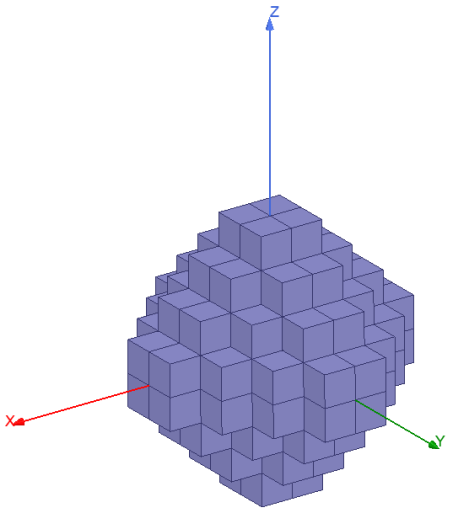

Figure 2.2. Approximate Spherical Animal Head Model

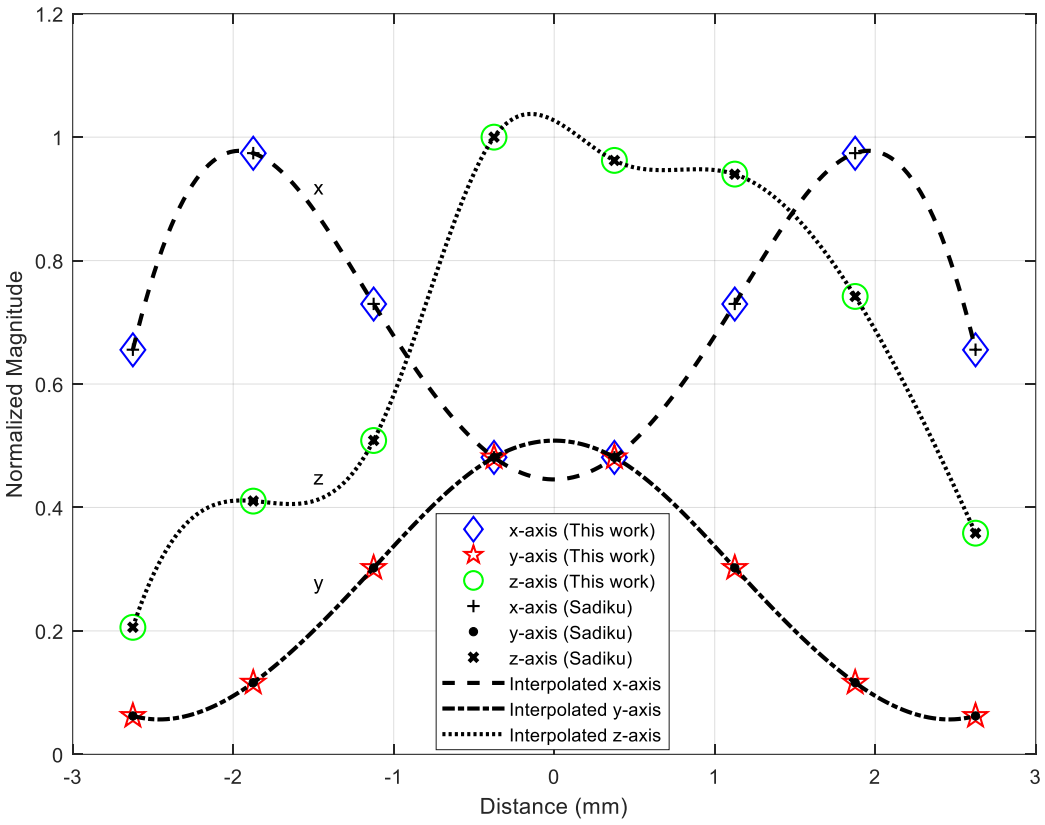

Figure 2.3. Power distributions in principal (x-y-z) axes of the head model

Afterwards, the performance of the forward problem solver is examined by comparing the results of examples in [34]. In the first case in [34], the electric field at the center of a cube (with edge length of 4cm) is determined for different frequencies and relative dielectric constant values. As seen in Table 2.1, both results from [34] and 3D MoM code developed in this study are same up to 3 decimal points.

Table 2.1. Comparison of results of original [34] and this work

f (Hz)	**ε_r**	**$\lvert E_{center} \rvert$ (V/m)**	
		[8]	**This work**
10^7	5	0,4172	0,4173
10^6	5	0,4172	0,4173
10^3	5	0,4172	0,4173
10^3	20	0,1124	0,1124
10^3	51.7	0,0503	0,0503

In the second case, a dielectric layer is illuminated by a plane wave and the field distribution along the object is determined. The model of the problem is given in Figure 2.4. The electric field distribution normalized to incident field, e^{norm}, is obtained and the root mean squared error (RMSE) between two studies is calculated by the formula,

$$RMSE = \left[\frac{1}{N}\sum_{i=1}^{N}(e^{norm}_{original_i} - e^{norm}_{fps\ i})^2\right]^{1/2} \tag{42}$$

where $e^{norm}_{original}$ and e^{norm}_{fps} are the electric field distributions normalized to incident fields from the original study in [34] and forward problem solver developed in this study, respectively. RMSE calculated for the model in Figure 2.4 is 0.29% which reveals that there is a very good agreement between the original work and this study for this specific case. Exact values for the distributions of $e^{norm}_{original}$ given in [34] and e^{norm}_{fps} determined by the forward problem solver are presented in Appendix A for further inspection.

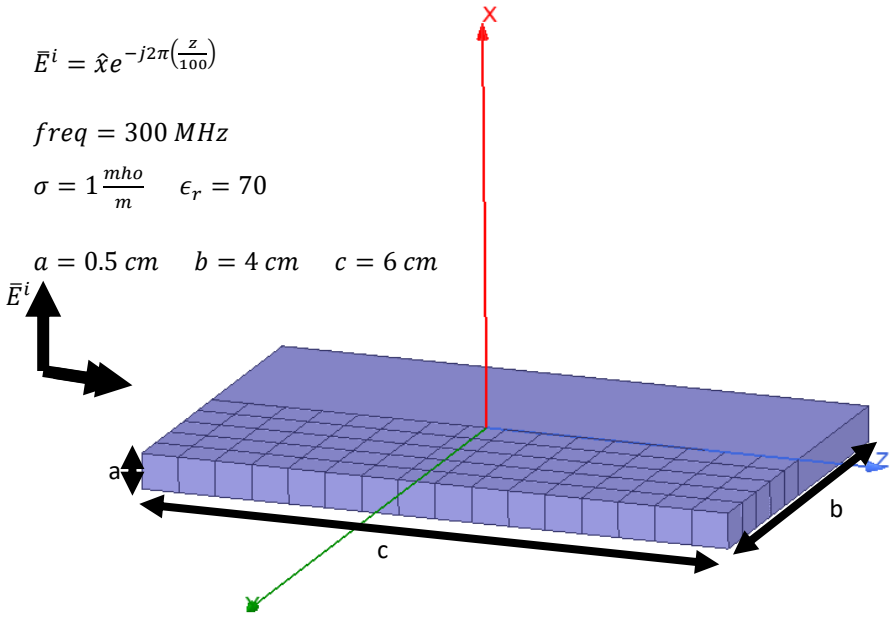

Figure 2.4. Model of the scattering problem in [34]

The third case studied in [34] is to illuminate the same dielectric slab by rotating it 90° around z-axis so that the incident electric field becomes tangential to air-dielectric interface as shown in Figure 2.5.

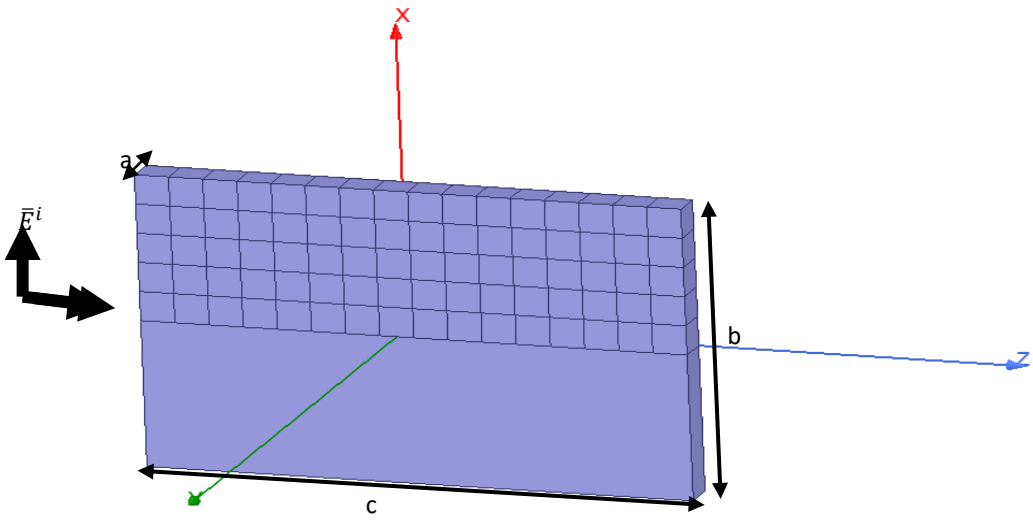

Figure 2.5. Model of the scattering problem in [34] with different excitation

RMSE values calculated for the distribution of x-component and z-component of E-field normalized to incident field, obtained by [34] and our study are 0.23% and 0.61%, respectively, which also implies a good agreement for both cases. As in the previous case, exact values for the distributions of $e_{original}^{norm}$ given in [34] and e_{fps}^{norm} determined by the forward problem solver are presented in Appendix 1 for further inspection for the third case as well.

Above examples demonstrate the capability of the 3D MoM code for solving the forward scattering problem for homogeneous elements with different shapes. The objects are modeled using uniform cubic mesh elements. In order to test the performance of the solver for inhomogeneous objects, cubic scatterers are created which have different relative permittivity value for the center and outer layers. ANSYS HFSS simulations are taken as reference in order to examine the performance of the 3D MoM solution. Inhomogeneous cubic object model in HFSS (see Figure 2.6) is illuminated by an x-polarized plane wave propagating in +z-direction at 1 GHz.

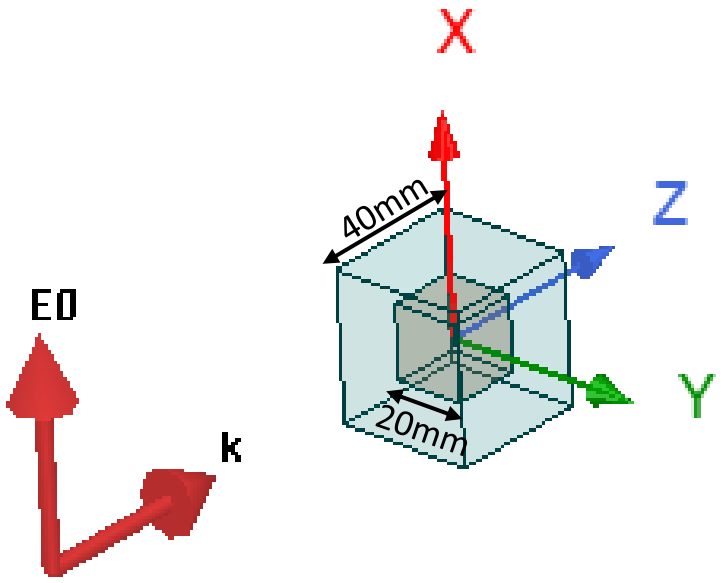

Figure 2.6. Inhomogeneous cube and incident field (plane wave) modeled in HFSS

The simulation is run for a dielectric contrast of 1.6/1 between layers such that inner dielectric layer has relative permittivity of $\varepsilon_r = 8$ while outer layer has $\varepsilon_r = 5$. At x=y=0, the percentage error between the results of developed code and HFSS simulations are given in Figure 2.7 for different mesh sizes (2.5mm ($0.023\lambda_g$), 5mm ($0.047\lambda_g$) and 10mm ($0.094\lambda_g$) where λ_g is the guided wavelength in the inner layer.) used in the MoM code. As seen from the figure, increasing the mesh resolution favors the performance of the 3D MoM solver as expected. The percentage error of E-field on *yz*-plane at the center of the object is shown in Figure 2.8 for mesh size 2.5mm. These results reveal that maximum relative error regions concentrate around the boundary between inner and outer regions neglecting the maximum error points at the corners of the outer layer.

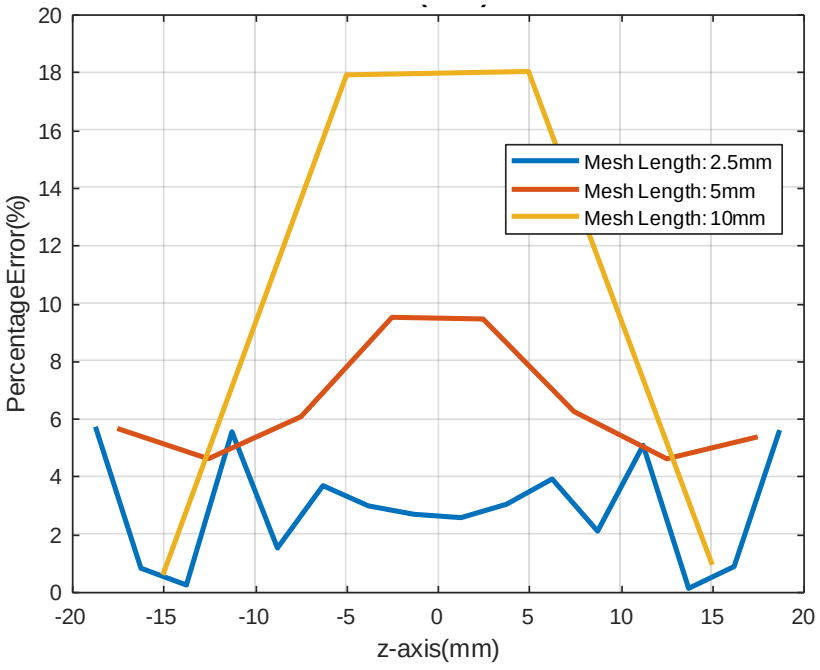

Figure 2.7. Relative Error for Total Electric Field distribution along z-axis of inhomogeneous cube model for different mesh sizes with respect to HFSS solution

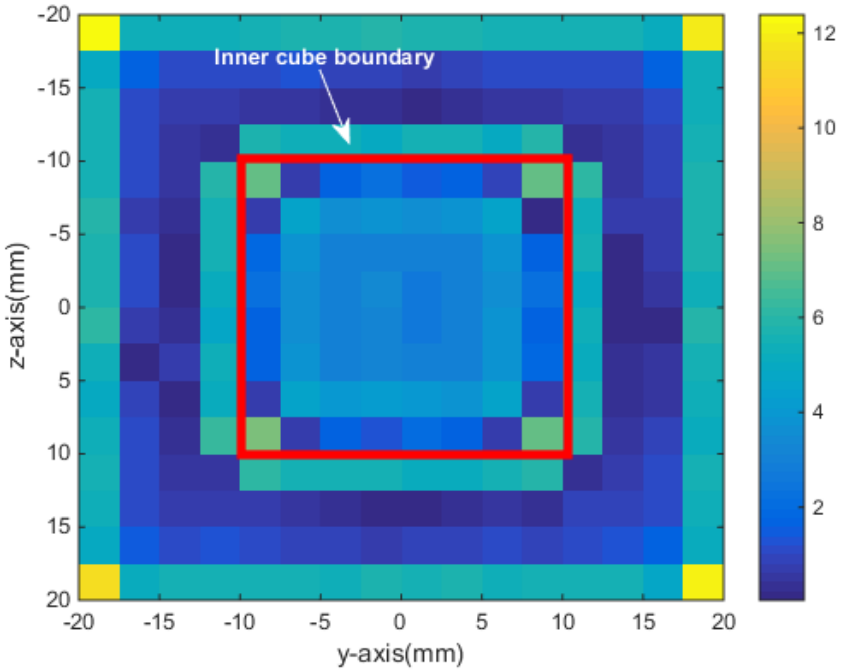

Figure 2.8. Percentage error of 3D MoM referenced to HFSS simulation for low dielectric contrast case

Table 2.2. Matrix solution times of 3D MoM Solver for different mesh size and solution methods

	3000 unknowns			**12288 unknowns**		
Solution type	**Matrix solution time (sec)**	**Number of iterations**	**Residual (Limit:10^{-8})**	**Matrix solution time (sec)**	**Number of iterations**	**Residual (Limit: 10^{-8})**
Direct Inverse Multiplication	1,24	-	-	36,44	-	-
Biconjugate Gradient (BiCG) Method	1,4	34	8,60 x10^{-9}	20,39	33	8,70 x10^{-9}
Conjugate Gradient Squared (CGS) Method	0,83	18	5,80 x10^{-9}	12,12	19	7,80 x10^{-9}
Biconjugate Gradient Stabilized (BiCGstab) Method	0,88	20	9,40 x10^{-9}	14,24	23	1,70 x10^{-9}
Biconjugate Gradient Stabilized (l) (BiCGstab-l) Method	0,81	9	9,30 x10^{-9}	11,74	9	3,60 x10^{-9}

Moreover, a study on matrix solution time is held and listed in Table 2 for 10x10x10 and 16x16x16 cubic mesh elements which corresponds to 3000 and 12288 unknowns, respectively. Matrix solution time is an important performance parameter that dominates the overall solution time of 3D MoM applications, which also affects the efficiency of the imaging algorithm. For direct inversion and various iterative methods listed in Table 2.2, matrix solution time is determined, and it is observed that as the size of the problem increases direct inversion become very inefficient while other methods reach the solution very fast with a few iterations. Consequently, Biconjugate Gradient Stabilized (l) (BiCGstab-l) Method [65] is chosen for the solution of MoM matrix equation.

2.2 Determination of Scattered/Total Field Quantities at Measurement Locations

Up to this point, the scattered field intensities in the cubic meshes of the dielectric object under test are calculated in the forward problem solver and compared with the results of the same problems given in [34] and solved by HFSS. In order to have a complete forward problem solver, the scattered field quantities outside the object are required to be calculated.

At the first step of the forward problem solver, the equivalent current densities which are assumed to exist and radiate into free space are obtained by the solution of state equation (16). Afterwards, the radiation problem from known sources is solved by the data equation given in (22) which leads us to the fields at real observation points outside the body. The field quantities at those points determined from forward problem solver and HFSS simulation software are compared and presented in the next sections.

2.2.1 Hertzian Dipole Excitation

In the previous sections, the incident field defined for scattering problem solution via 3D MoM is plane wave which is an appropriate choice at the beginning of the code verification period. However, in the real-world implementation of the imaging system, there exist near field radiation signals emitted from corresponding antennas around the head of the person who is suspected of having brain stroke. Therefore, a more realistic radiation source, Hertzian dipole, is preferred in the forward problem solution in order to obtain the scattered and total E-field intensities at the sensor points around the head. The results of the forward problem solver in terms of incident, scattered and total E-field strength values are compared with the ones from HFSS simulations, and they are observed to be consistent with each other. This result also reveals that the forward problem solver is powerful when the near field conditions are valid which is very crucial in order to have a robust imaging system.

Radiated field of a z-directed Hertzian dipole with length d and current I is given as:

$$\bar{E}(\bar{r}) = \eta_0 \frac{jkId}{4\pi r} e^{-jkr} \left\{ \hat{r} \left[\frac{1}{jkr} + \left(\frac{1}{jkr} \right)^2 \right] 2\cos\theta + \hat{\theta} \left[1 + \frac{1}{jkr} + \left(\frac{1}{jkr} \right)^2 \right] \sin\theta \right\} \quad (44)$$

In order to test the forward problem solution with Hertzian dipole, an HFSS model is prepared. There exist 9 sensing locations on an arc separated by 5 degrees rotation from each other at the same radius from the source position (r=170mm) as shown in Figure 2.1. The comparison of developed code in MATLAB for the solution of forward problem and HFSS simulation is realized at these points at f=2 GHz in terms of total E-field magnitude and phase and corresponding graphs are given in Figure 2.10 and Figure 2.11, respectively, for mesh sizes of 10 mm ($0.184\lambda_g$) and 20mm ($0.368\lambda_g$). It is observed from the results presented in Figure 2.10 and Figure 2.11 that as the mesh resolution of forward solver is increased, the agreement with HFSS simulation increases as expected.

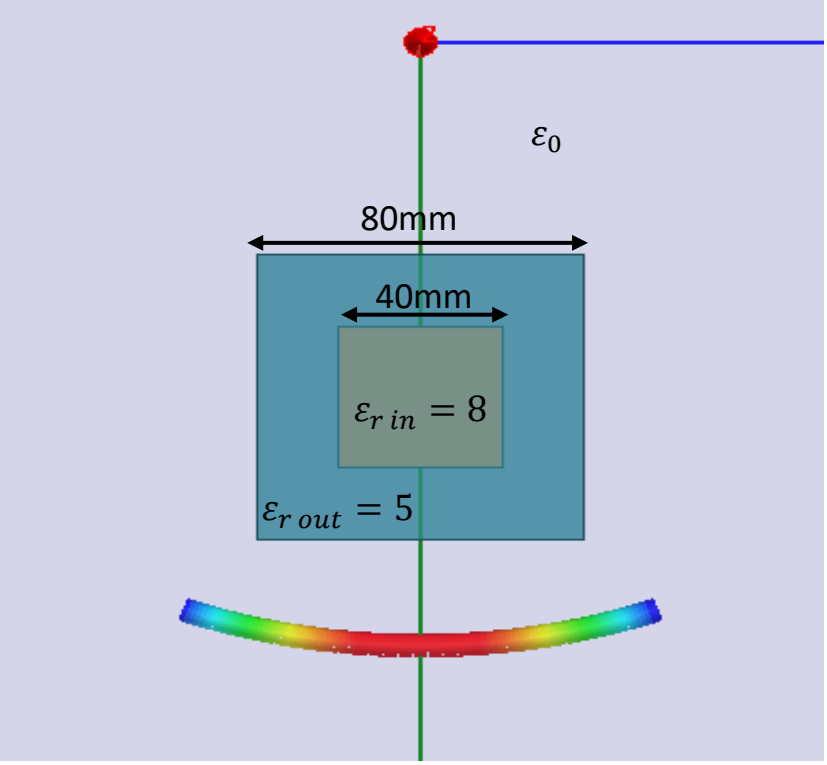

Figure 2.9. HFSS model for Hertzian Dipole incident wave

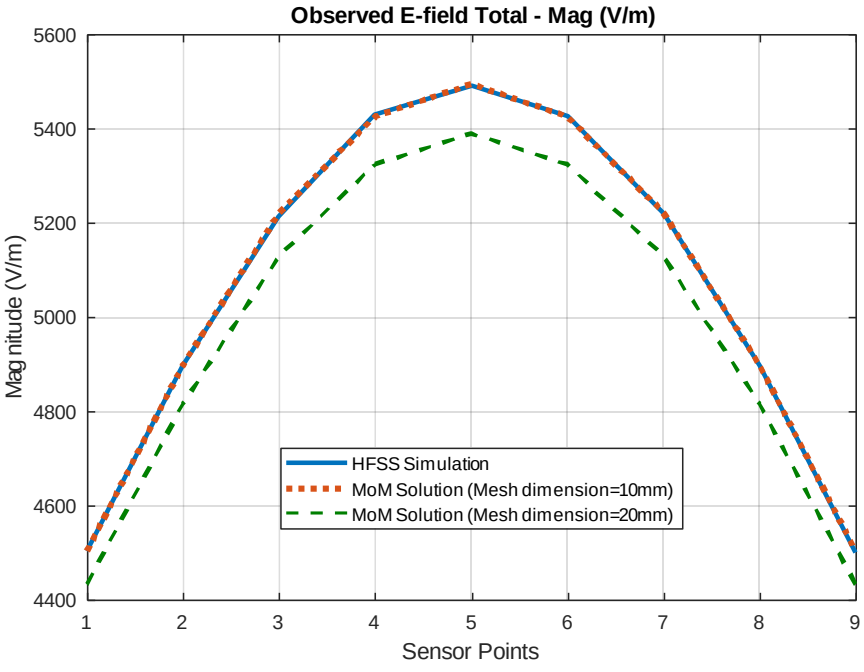

Figure 2.10. Comparison of forward problem solver (MATLAB) and HFSS simulation for Hertzian Dipole excitation - Magnitude

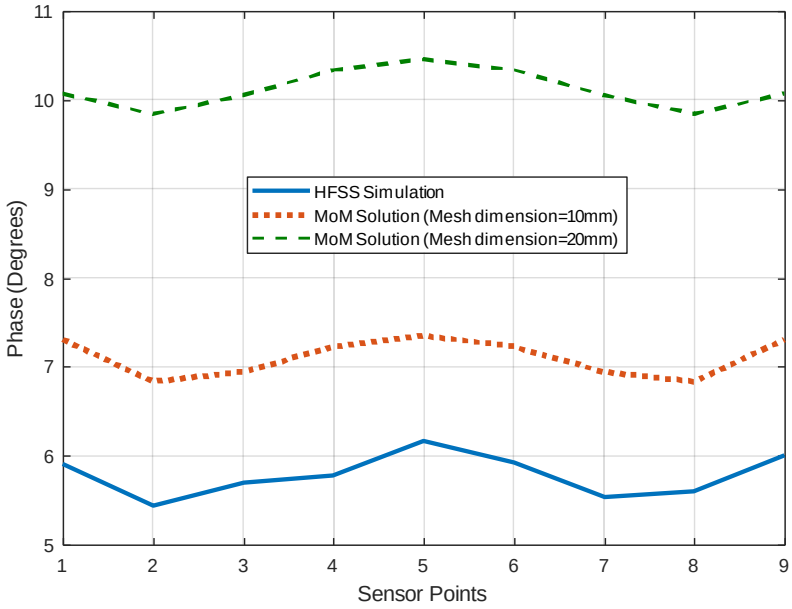

Figure 2.11. Comparison of forward problem solver (MATLAB) and HFSS simulation for Hertzian Dipole excitation - Phase

2.2.2 Modification on Data Equation to Handle Polarization and Orientation of Receiver Antennas

In realistic scenarios, transmitter and receiver antennas will be placed around the head, distributed over an ellipsoid surface. In all of the experimental studies in microwave imaging of brain, linearly polarized antennas are used. Therefore, received signal at an antenna will be the linear combination of all three components (x,y,z) of the electric field with weighting coefficients determined by the position and orientation of the corresponding receiver antenna on the ellipsoid surface. This linear transformation is performed by modifying the radiation matrix T given in (22). Multiplication with T matrix gives all three components of the electric field at M receiver positions. After modifying T matrix, the appropriate combination of three components will result only one field value for each receiver according to its polarization. Modified radiation matrix T^m is obtained in the following manner. First, receiver antennas polarization matrix P_r, each column of which is x, y and z

components of the polarity (p_r^x, p_r^y and p_r^z), is constructed with respect to the configuration of receiver antenna polarizations, such that,

$$P_r = [p_r^x \quad p_r^y \quad p_r^z] = \begin{bmatrix} p_{r1}^x & p_{r1}^y & p_{r1}^z \\ \vdots & \vdots & \vdots \\ p_{rM}^x & p_{rM}^y & p_{rM}^z \end{bmatrix}_{Mx3} \tag{45}$$

Diagonalizing the column polarity vectors and combining as shown below, final polarization multiplier matrix is obtained as:

$$P_r^{fin} = \left[p_{r\,diag}^x \quad p_{r\,diag}^y \quad p_{r\,diag}^z\right]_{Mx3M} \tag{46}$$

where,

$$p_{r\,diag}^q = \begin{bmatrix} p_{r1}^q & 0 & 0 \\ 0 & \ddots & 0 \\ 0 & 0 & p_{rM}^q \end{bmatrix}_{MxM} \quad \text{for} \quad q = \{x, y, z\} \tag{47}$$

Modified radiation matrix T^m is calculated as:

$$[T^m]_{Mx3N} = \left[P_r^{fin}\right]_{Mx3M} [T]_{3Mx3N} \tag{48}$$

which results the modified data equation

$$[T^m]_{Mx3N} \left[j_{eqv}\right]_{3Nx1} = [e_{obs}]_{Mx1} \tag{49}$$

This modification is valid for single polarized receiver antennas. When dual polarized antennas are utilized, the modification should be applied for each polarization, resulting in an electric field vector of size $2M \times 1$.

2.3 Relation Between Measured Field Intensity and Antenna Port Voltage Values

In a physical imaging system, the measured quantities are only the voltage values at the receiver antenna ports or S-parameters of the transmitting-receiving antenna pairs which gives the voltage ratios at/between the ports for incoming and outgoing signals

under certain conditions. In order to observe the applicability of sensing the E-field level at corresponding antenna positions instead of including the antennas in the solution and determining the voltage signal levels at the ports, a couple of simulations with HFSS are realized and the results are presented below.

As a first observation, the voltage ratios (S_{21}) and E-field ratios (E_2/E_1) are compared for one transmitting and one receiving antenna pair which are placed on the same plane (co-planar arrangement) as shown in Figure 2.12. A probe-fed patch antenna operating at 1.64 GHz, with a dimension of 100mm x 100mm, is utilized in HFSS simulations. E-field values are obtained over a line standing on the center of the patch antenna surfaces aligned in polarization direction (x-direction).

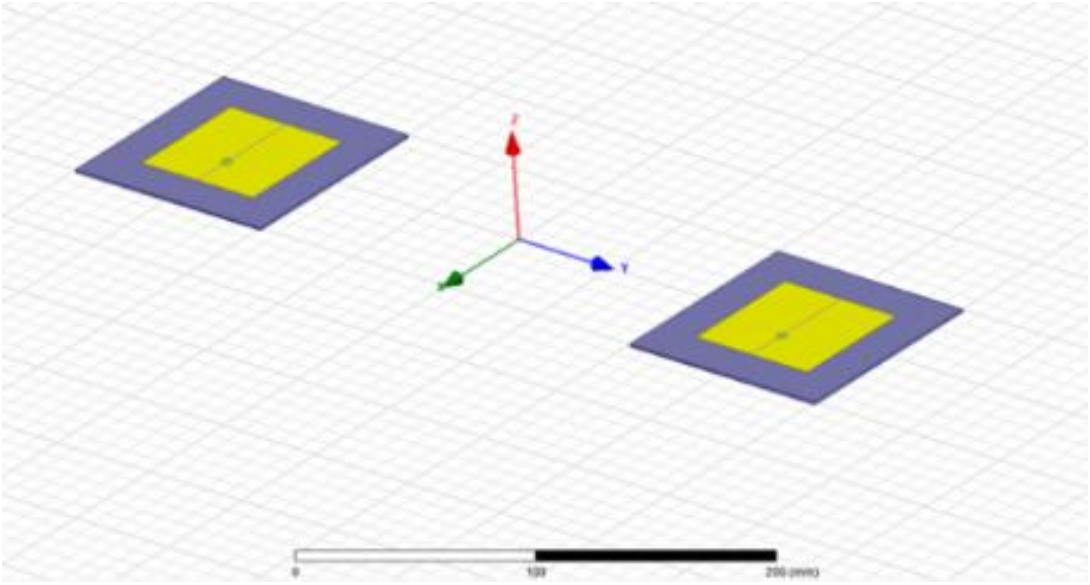

Figure 2.12. Co-planar arrangement of 2-antenna system

The results of the simulation are given in Figure 2.13. The position of "10mm" in x-axis on the graphs is the place where the feed probe of patch antenna stands in that axis. With this simulation, it is observed that the ratios of E-field and port voltages are fairly close to each other especially in magnitude and at the feed probe position in x-axis, however, there is no agreement in terms of phase values.

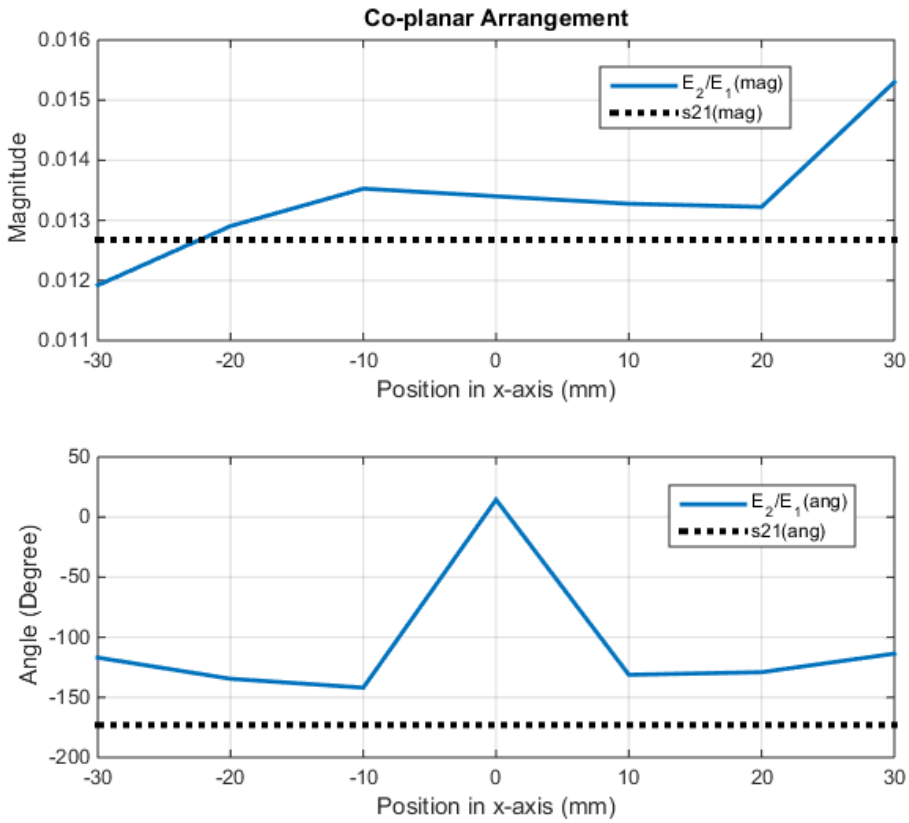

Figure 2.13. Comparison of voltage and E-field ratios for co-planar arrangement

Since the voltage (and naturally E-field) values are at a very low level due to the co-planar arrangement of 2-antenna system, there may possibly occur solution errors due to solution inaccuracy. Therefore, a face-to-face arrangement is also tested in terms of same parameters for co-planar arrangement case (see Figure 2.14) and the results given in Figure 2.15 show that the magnitudes of the voltage and E-field ratios at feed probe position are very close to each other. Nonetheless, the phase characteristics are incompatible for that case as well

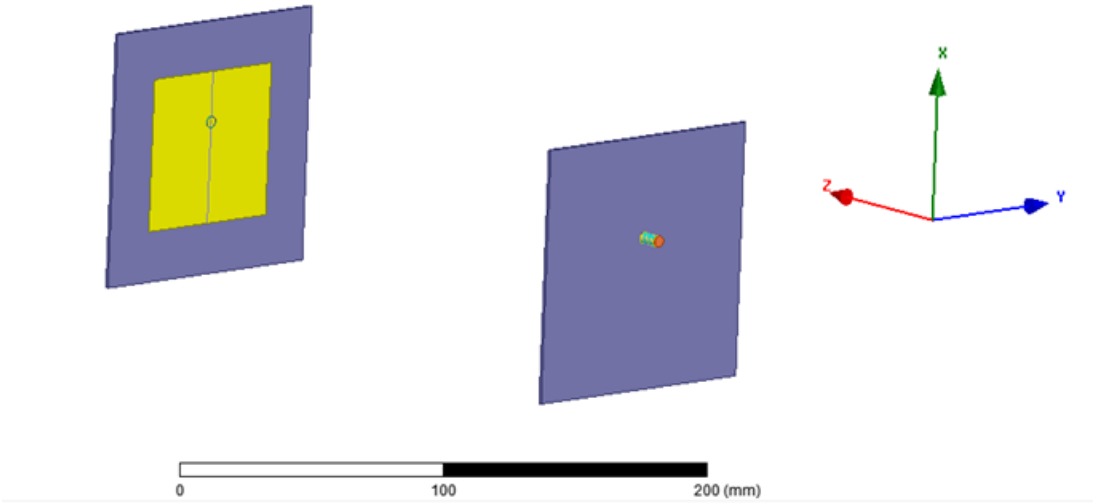

Figure 2.14. Face-to-face arrangement of 2-antenna system

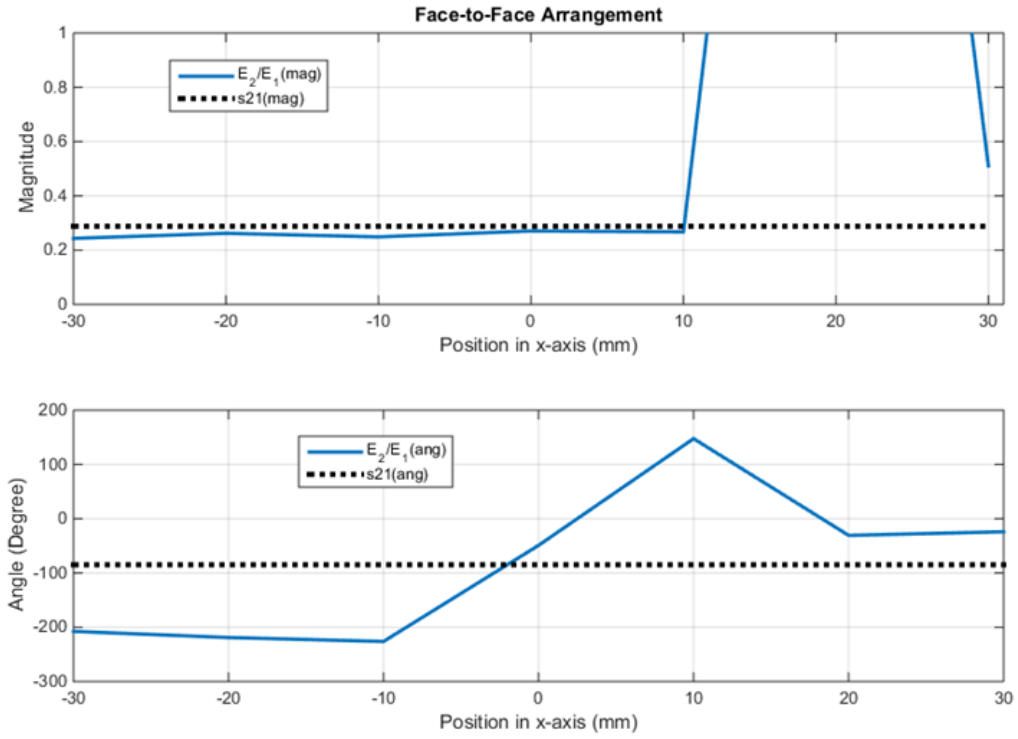

Figure 2.15. Comparison of voltage and E-field ratios for face-to-face arrangement

In order to gather deeper intuition about the phenomena investigated above, a more realistic scenario is studied which utilizes an 8-element patch antenna array shown in Figure 2.16. With this configuration, the ratio of the E-field ratios (E_n/E_m) to voltage ratios (V_n/V_m), given as (E_n/E_m)/ (V_n/V_m), for different pairs of array elements are compared and presented in Figure 2.17 and Figure 2.18 along the line on x-axis. X-axis position of "10mm" defines the position of feed probe. As seen from the results, the agreement between different antenna pairs is moderately weak which makes it clear that the forward problem solver algorithm is necessarily required to incorporate the voltages at the antenna ports, or S-parameters of the system, which are actual and only measurement results in a real physical system.

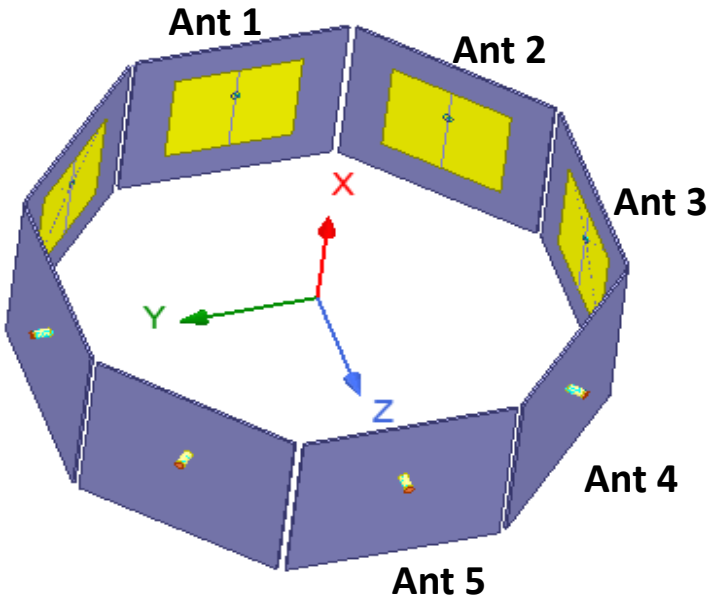

Figure 2.16. 8-element Octagonal Patch Antenna Array

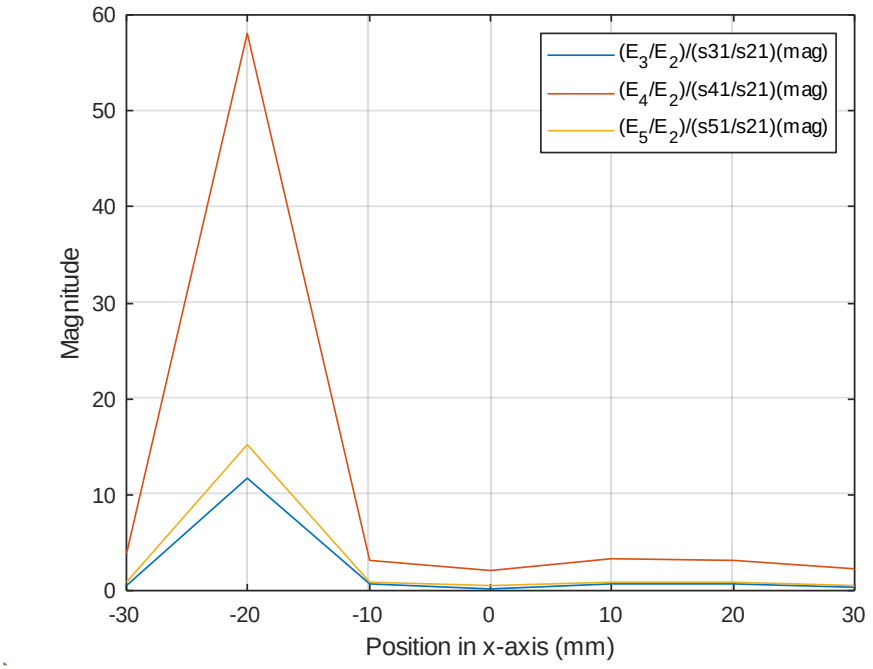

Figure 2.17. Octagonal Antenna Array E-field ratio to voltage ratio comparison for different antenna pairs – Magnitude

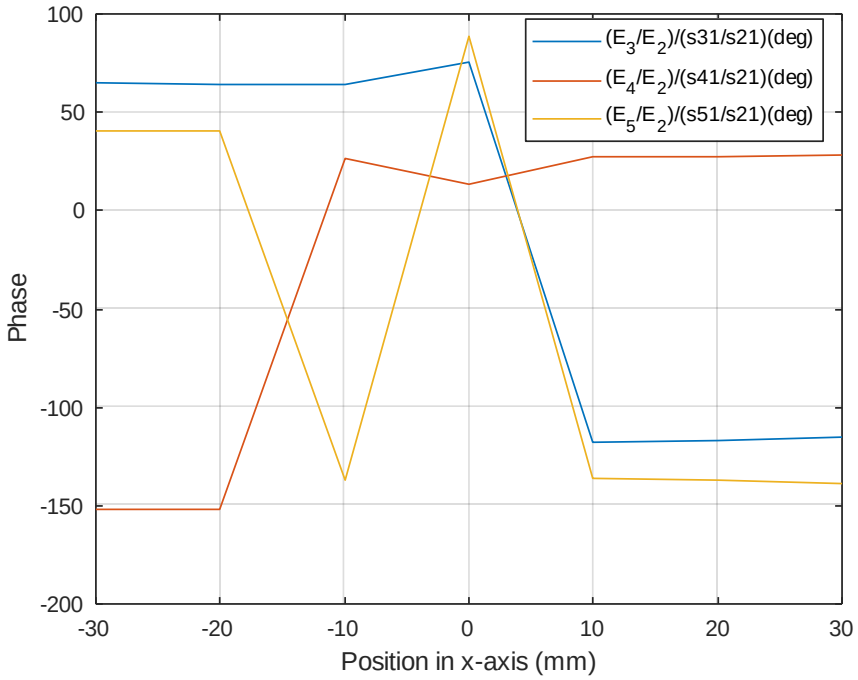

Figure 2.18. Octagonal Antenna Array E-field ratio to voltage ratio comparison for different antenna pairs – Phase

To calculate the voltage at the receiving antenna ports from the electric field values at the antenna aperture reaction theorem will be utilized. As a first step for the application of reaction theorem, consider an antenna excited by a current source. Assume that when the antenna is excited with I_0, the current density induced on a surface enclosing the antenna (S) is $\bar{J}_{ap}^{inc}$. Next, consider a transmitter and receiver antenna pair. When the transmitter antenna is excited with I_0 the open circuit voltage measured at the receiver antenna is V_{oc}. Moreover, denote the electric field intensity distribution on the enclosing surface S of the receiver antenna as $\bar{E}_{ap}^{inc}$. Then, by using reaction theorem, V_{oc} can be expressed as ([64]):

$$V_{oc} = \frac{1}{I_0} \int \bar{J}_{ap}^{inc} \cdot \bar{E}_{ap}^{inc} dS \tag{50}$$

The current density on the aperture can be determined by the formula,

$$\bar{J}_{ap}^{inc} = \hat{n} \times \bar{H}_{ap}^{inc} \tag{51}$$

where, $\hat{n}$ is the unit vector normal to surface S, and $\bar{H}_{ap}^{inc}$ is the magnetic field intensity on antenna aperture which can be obtained by the full wave EM simulations as a characterization process of each individual antenna element in the imaging system. Therefore, the near field radiated fields obtained through full-wave analysis of the antenna is incorporated into the forward model. $\bar{E}_{ap}^{inc}$ is also available from the same HFSS simulation. Note that $\bar{J}_{ap}^{inc}$ and $\bar{E}_{ap}^{inc}$ data is required over a closed surface. However, in order to increase computational efficiency, using an open surface close to the antenna aperture is preferred. The size and location of this surface are determined based on the results presented in [66]. For the patch antenna given in previous examples, an 120mm x 120mm aperture is chosen to be at a distance of 5mm from the antenna divided into N_s number of samples. The results are used to compute V_{oc} for a face-to-face antenna configuration shown in Figure 2.19. A row vector of size 1x3N_s is defined for the aperture current density distribution, j_{ap}, corresponding to each component of the current density at each sampling point.

Similarly, a column vector of size $3N_s$x1 is defined for the incident electric field intensity at the aperture, e_{ap}^{inc}. Then the open circuit voltage is obtained as:

$$V_{oc} = \frac{\Delta S}{I_0}\left[j_{ap}\right]\left[e_{ap}^{inc}\right] \tag{52}$$

where ΔS is the area of a mesh on the aperture.

First, two antennas are placed parallel to each other (Figure 2.20(a)) and the V_{oc} corresponding to this case is used as a reference (V_{oc}^{ref}) value for normalization. Then, one of the antennas are rotated up to 40^o (Figure 2.20(b)) and V_{oc} values are computed. Then, these values are divided to V_{oc}^{ref} to obtain V_{oc} ratio values. Similarly, S_{21} values for each angular position are obtained through HFSS simulations and S_{21} ratio values are obtained with reference to 0^o. These ratios are presented and compared in Figure 2.21.

As observed from Figure 2.21, both the magnitude and phase characteristics of S_{21} and calculated V_{oc} ratios are in a good agreement with each other which makes the approach feasible in order to reach a realistic image reconstruction model. Furthermore, it implies that suggested port voltage calculation step is essential to be integrated into the forward solution algorithm which is one of the main contributions of this study.

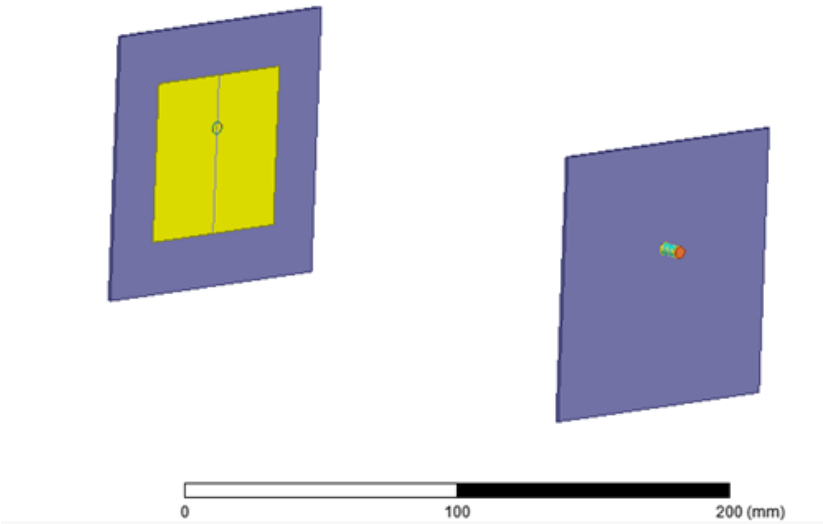

Figure 2.19. HFSS simulation model

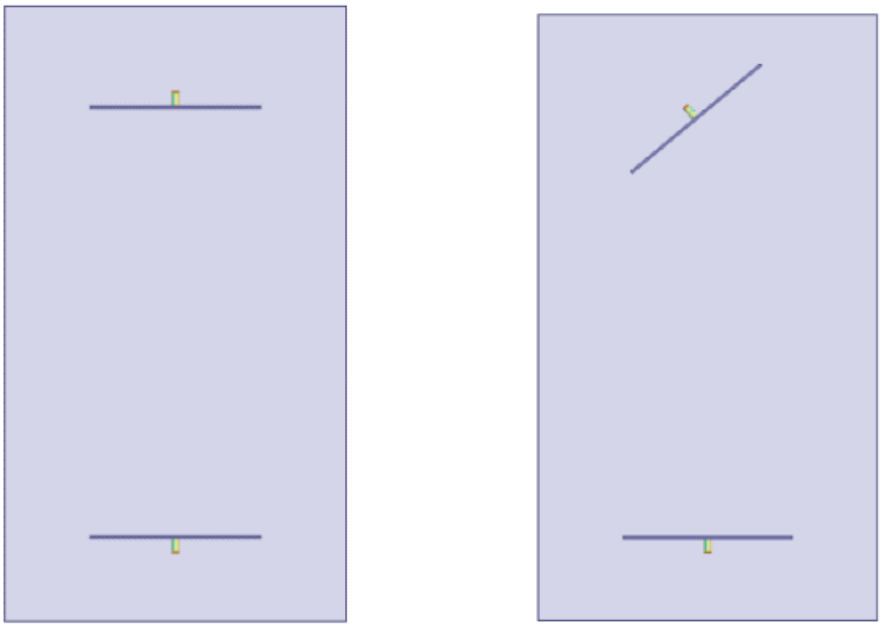

(a) (b)

Figure 2.20. Arrangement of antenna pair as; (a) parallel (b) 40^{o} rotated

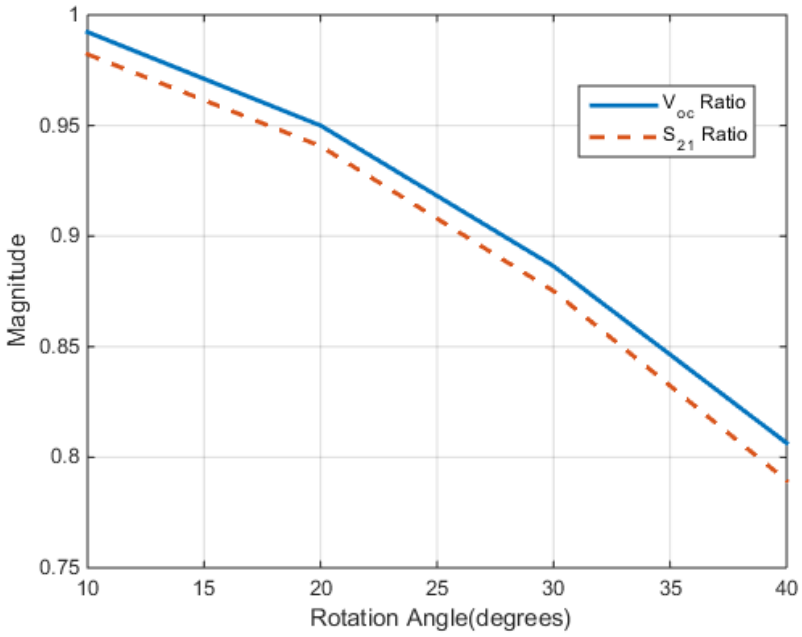

(a)

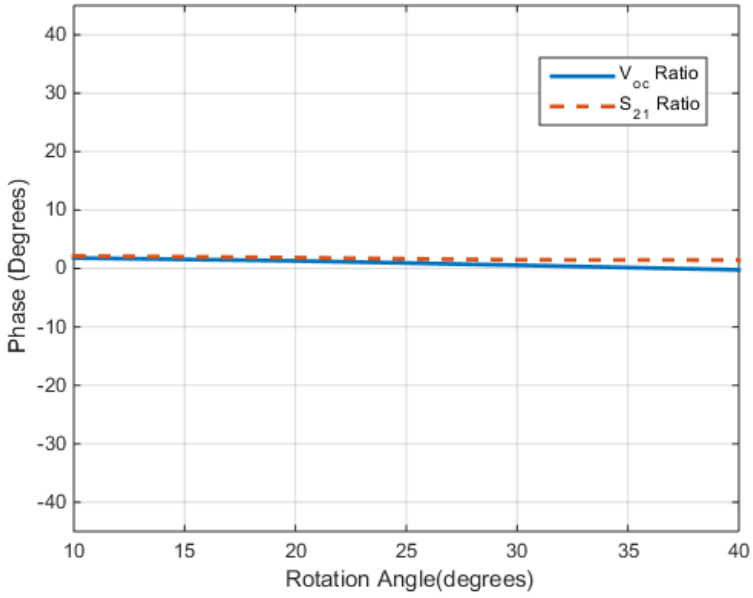

(b)

Figure 2.21. Comparison of V_{oc} and S21 ratios: (a) magnitude and (b) phase

2.3.1 Derivation of Data Equation in Terms of Antenna Port Voltages/S-Parameters

First, the formulation constructed to obtain the S_{21} parameter when there exists a scatterer between two antennas will be presented. Then, this formulation will be generalized for M number of receivers and K number of transmitters. When Antenna-k is transmitting and Antenna-m is receiving, the open circuit voltage induced in Antenna-m in presence of the scatterer, V_{oc}^{mk}, can be computed from the total fields at the aperture of the second antenna as:

$$V_{oc}^{mk} = \frac{\Delta S}{I_0}\left[j_{ap,m}\right]\left[e_{ap,m}^{inc,k} + e_{ap,m}^{scat,k}\right] \tag{53}$$

where $e_{ap,m}^{inc,k}$ is the electric field distribution on the mth aperture in the absence of the scatterer and $e_{ap,m}^{scat,k}$ is the scattered electric field distribution on the mth aperture computed by the data equation when kth transmitter is excited. In order to express the S-parameter (S_{21}) in terms of open circuit voltage, the self-induced open circuit voltage values for transmitter antenna in the absence of the scatterer is defined as the reference voltage, $V_{oc}^{ref,k}$, as:

$$V_{oc}^{ref,k} = \frac{\Delta S}{I_0}\left[j_{ap,k}\right]\left[e_{ap,k}^{inc,k}\right] \tag{54}$$

Finally, S_{mk} parameter can be obtained as:

$$s_{mk} = \frac{V_{oc}^{mk}}{V_{oc}^{ref,k}} \tag{55}$$

When there are K transmitters, the aperture field column vector is extended to be a matrix to incorporate field values due to excitation of each transmitter. Each column of this matrix, $E_{ap,m}^{inc}$, corresponds to field values due to excitation of each transmitter

$$\left[E_{ap,m}^{inc}\right] = \left[e_{ap,m}^{inc,1}\ \ e_{ap,m}^{inc,2}\ \ \dots\ e_{ap,m}^{inc,K}\right]_{3N_s \times K} \tag{56}$$

Similar procedure is applied to obtain the scattered field distribution matrix, $E_{ap,m}^{scat}$, when there is a scatterer.

The open circuit voltage at m[th] receiver due to excitation of each transmitter results in a row vector, V_{oc}^{m}, of size 1xK as:

$$[V_{oc}^{m}]_{1\times K} = \frac{\Delta S}{I_0}\left[j_{ap,m}\right]_{1\times 3N_s}\left[E_{ap,m}^{inc} + E_{ap,m}^{scat}\right]_{3N_s\times K} \tag{57}$$

Similarly, the reference voltage becomes a row vector, V_{oc}^{ref}, as:

$$\left[V_{oc}^{ref}\right]_{1\times K} = \frac{\Delta S}{I_0}\left[j_{ap,k}\right]_{1\times 3N_s}\left[E_{ap,k}^{inc}\right]_{3N_s\times K} \tag{58}$$

Finally, the S-parameter row vector can be obtained by element-by-element division of V_{oc}^{m} vector to V_{oc}^{ref} vector. Expanding the matrices for M receivers, we obtain

$$[V_{oc}]_{M\times K} = \frac{\Delta S}{I_0}\left[j_{ap}\right]_{M\times 3MN_s}\left[E_{ap}^{inc} + E_{ap}^{scat}\right]_{3MN_s\times K} \tag{59}$$

where

$$\left[j_{ap}\right]_{M\times 3MN_s} = \begin{bmatrix} \left[j_{ap,1}\right]_{1\times 3N_s} & \cdots & \left[j_{ap,1}\right]_{1\times 3N_s} \\ \vdots & \ddots & \vdots \\ \left[j_{ap,M}\right]_{1\times 3N_s} & \cdots & \left[j_{ap,M}\right]_{1\times 3N_s} \end{bmatrix} \tag{60}$$

$$\left[E_{ap}^{inc}\right]_{3MN_s\times K} = \begin{bmatrix} \left[E_{ap,1}^{inc}\right]_{3N_s\times K} \\ \vdots \\ \left[E_{ap,M}^{inc}\right]_{3N_s\times K} \end{bmatrix} \tag{61}$$

To perform the division to reference voltages by matrix multiplications, a diagonal normalization matrix is constructed by using the reference open circuit voltage vector as:

$$\left[V^{normalize}\right]_{K\times K} = \left[diag\left({V_{oc}}^{ref}\right)\right]^{-1} \tag{62}$$

Finally, the S-parameter matrix can be obtained as:

$$\left[S_{para}\right]_{M\times K} = \left[V_{oc}\right]_{M\times K}\left[V^{normalize}\right]_{K\times K} \tag{63}$$

Note that, although the antennas used in the MIMO array are identical, the characterization of each antenna is done individually, and aperture field distributions are found separately to include different scattering effects associated with the specific position of the corresponding antenna.

Below results are presented as a verification of the above formulation derived for S-parameters and antenna port voltages calculated by the utilization of reaction theorem. A dual polarized antenna array of 21 elements (42 ports in total) on an ellipsoidal surface (see Figure 2.22) is investigated for the verification process. One element in the array (Antenna 11 in this case) is chosen as the transmitter and the rest are receivers. By following the steps detailed above, S-parameter values ($S_{(m)(11)}$ for m=1 to 42) for each receiver antennas are calculated and given in Figure 2.23. The calculation for the reference open circuit voltage is done for both scenarios that there exists a scatterer in the system (Figure 2.22) and in the absence of the scatterer. The results of these two scenarios are presented in Figure 2.23 in comparison with the results obtained from the full-wave analysis of the whole system in HFSS. It is observed that the reference input open circuit voltage values do not differ if there exists a scatterer or not. Both calculated S-parameter characteristics are in good agreement with the S-parameter values directly gathered from HFSS simulations.

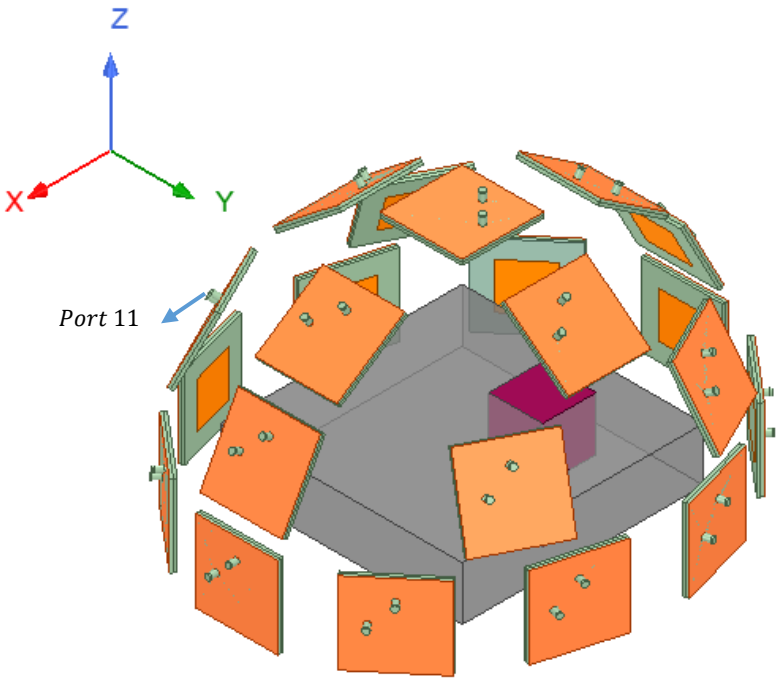

Figure 2.22. Ellipsoidal placement of patch antennas, measurement case with object and excitation at Port 11

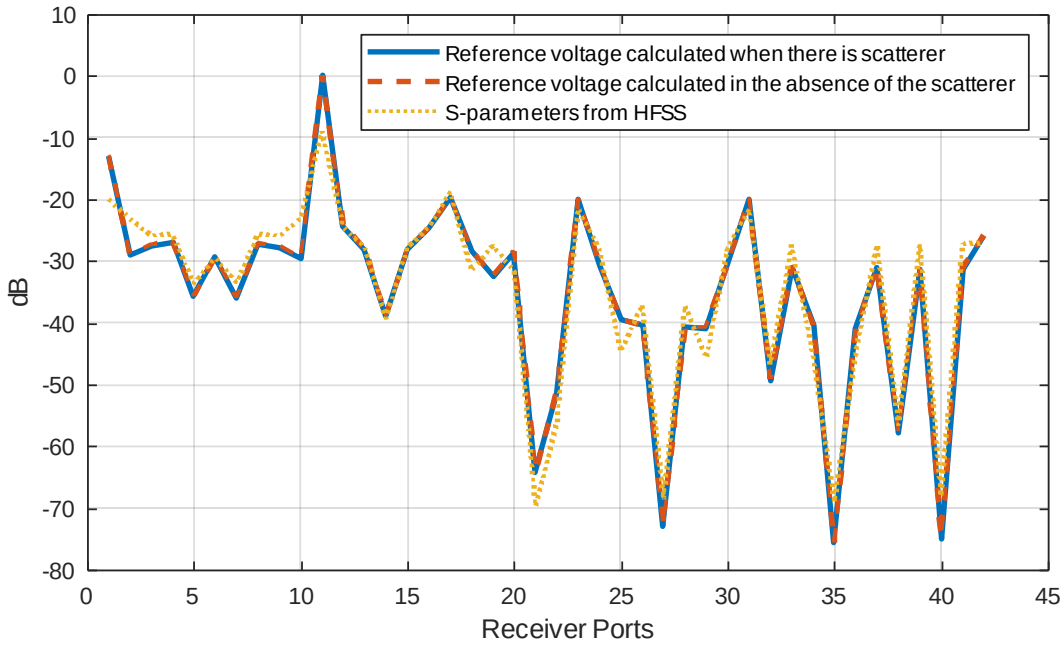

Figure 2.23. Measured and calculated S-parameter values

CHAPTER 3

INVERSE PROBLEM

In the inverse problem of this study, the goal is to infer the electrical properties of the object under test, which is the brain structure in our case, using the acquired near-field measurements. We develop an alternating minimization approach to solve this inverse problem. We first present the formulation of the inverse problem and then the solution approach we developed, together with the implementation details.

3.1 Definition of State and Data Equations

For the sake of traceability, we first revisit the state and data equations obtained in Chapter 2 for the forward problem. The state equation as given in (16) and (41) is

$$\left([G^S] - [\tilde{\tau}'_{diag}]\right)[j^{eqv}] = -[e^i] \tag{64}$$

where G^S is the Green's matrix, j^{eqv} is the unknown equivalent current density vector, e^i is the incident electrical field intensity inside the object, $\tilde{\tau}'_{diag}$ is the diagonal matrix formed using the unknown electrical properties parameter τ, details of which are given in equation (14). The data equation as given in (22) is

$$[T][j^{eqv}] = [e^{obs}] \tag{65}$$

where T is the radiation matrix and e^{obs} is the observed electrical field intensity vector at receiver points. Alternatively, in the image reconstruction process, it is possible to relate e^{obs} directly to the S-parameter measurements using equation (63) as presented in Chapter 2. As a result, the measured S-parameter values obtained for the realistic case, where the near-field radiation patterns of the antennas are required to be considered, can be incorporated into the data equation efficiently.

In the inverse problem, the main goal is to estimate the unknown electrical properties of the object as captured in $\tilde{\tau}'_{diag}$ by using equations (64) and (65). Because the current density vector j^{eqv} in these equations is also unknown, we should jointly solve these equations also for j^{eqv}. An alternating minimization approach is used for this purpose as explained in the next section. Also note that the model in (64) is a nonlinear model due to the multiplication of the unknown electrical properties parameter with the unknown equivalent current density vector. Hence, we have a nonlinear inverse problem which is more difficult to solve compared to the linear ones.

3.2 Formulation and Solution of the Inverse Problem via Alternating Minimization

Since we have a nonlinear ill-posed inverse problem, we exploit prior knowledge about the unknown $\tilde{\tau}$ and j^{eqv} in the form of regularization. This leads to the minimization of the following cost function:

$$min_{\tilde{\tau}',j^{eqv}} \left\{ \|[T][j^{eqv}] - [e^{obs}]\|_2^2 + \alpha \left\| \left([G'] - [\tilde{\tau}'_{diag}] \right) [j^{eqv}] + [e^i] \right\|_2^2 \right\} + \lambda_{\tilde{\tau}'} R(\tilde{\tau}') + \lambda_{j^{eqv}} R(j^{eqv}) \quad (66)$$

Here $R(\tilde{\tau})$ and $R(j^{eqv})$ are regularization functions and $\lambda_{\tilde{\tau}'}$ and $\lambda_{j^{eqv}}$ are regularization parameters for the variables $\tilde{\tau}'$ and j^{eqv}, respectively.

To solve the minimization problem in equation (66), we use an alternating minimization (coordinate descent) approach. That is, we first solve the minimization problem over j^{eqv} with $\tilde{\tau}'$ fixed, then solve for $\tilde{\tau}'$ with j^{eqv} fixed and repeat these iterations until a stopping criterion is satisfied. Hence, the following optimization problems are successively solved over each variable while fixing the other:

$$min_{j^{eqv}} \left\{ \|[T][j^{eqv}] - [e^{obs}]\|_2^2 + \alpha \left\| \left([G^S] - [\tilde{\tau}'_{diag}] \right) [j^{eqv}] + [e^i] \right\|_2^2 + \lambda_j R(j^{eqv}) \right\} \quad (67)$$

$$min_{\tilde{\tau}'}\left\{\left\|\left(\left[j_{diag}^{eqv}\right][\tilde{\tau}'] - [G^S][j^{eqv}]\right) - \left[e^i\right]\right\|_2^2\right\} + \lambda_\tau R(\tilde{\tau}') \tag{68}$$

The first one is to update j^{eqv} and the second one is to update $\tilde{\tau}'$. Here j_{diag}^{eqv} is the diagonal matrix formed by the elements of the vector j^{eqv} as follows:

$$[j_{diag}^{eqv}] = \begin{bmatrix} j_1^{eqv} & 0 & 0 \\ 0 & \ddots & 0 \\ 0 & 0 & j_{3N}^{eqv} \end{bmatrix} \tag{69}$$

Note that $\tilde{\tau}'$ which is previously demonstrated in equation (13) can also be expressed as:

$$[\tilde{\tau}'] = \begin{bmatrix} [I]_{NxN} \\ [I]_{NxN} \\ [I]_{NxN} \end{bmatrix} [\tilde{\tau}]_{Nx1} \tag{70}$$

where $[I]_{NxN}$ is an NxN identity matrix. Inserting (69) into (67), the final form of the optimization problem for updating $\tilde{\tau}$ is obtained as:

$$min_{\tilde{\tau}}\left\{\left\|\left(\left[j_{diag}^{eqv}\right]\begin{bmatrix} [I]_{NxN} \\ [I]_{NxN} \\ [I]_{NxN} \end{bmatrix}[\tilde{\tau}] - [G^S][j^{eqv}]\right) - [e_i]\right\|_2^2\right\} + \lambda_{\tilde{\tau}} R(\tilde{\tau}) \tag{71}$$

An outer iteration limit is defined for the alternating minimization approach together with an inner iteration limit for the update of each variable, $\tilde{\tau}$ and j^{eqv}. As the stopping criterion for the iterations, two conditions are checked: either the percentage change in each variable drops below a predefined value, or the limit for the maximum number of iterations is reached.

Note that it seems possible to utilize only data equation for the solution of j^{eqv}, however, this problem cannot be uniquely and correctly solved without additional information since it is under-determined due to the limited number of measurements at receiver locations compared to the excess number of unknowns in the imaging domain. Therefore, the state equation is also incorporated into the joint minimization

problem which transforms the problem into an over-determined one and provides reasonable results.

In the simulations, it is required that the forward problem solver is run first in order to provide the measurement data necessary for the inverse problem solver, which are namely the observed scattered field or S-parameters, Green's matrix and incident field values without object present.

3.3 Iterative Solution Method Based on C-SALSA and Implementation Details

3.3.1 Constrained Split Augmented Lagrangian Shrinkage Algorithm (C-SALSA)

Constrained Split Augmented Lagrangian Shrinkage Algorithm (C-SALSA) proposed by Afonso et al. uses an augmented Lagrangian method, specifically the alternating direction method of multipliers (ADMM), and variable splitting to provide a general-purpose efficient algorithm for solving linear inverse problems with regularization [54]. In order to follow the notation of the algorithm in [54], in this section, the convention for matrices and vectors are provided differently from the rest of this thesis, such that capital and small bold letters represent matrices and vectors, respectively.

For an inverse problem with a noisy observation $\boldsymbol{y}$, unknown image $\boldsymbol{x}$, and forward model $\boldsymbol{y} = \boldsymbol{B}\boldsymbol{x} + \boldsymbol{n}$ with $\boldsymbol{B}$ being the system matrix and $\boldsymbol{n}$ being noise, C-SALSA algorithm solves the following constrained optimization problem [54]:

$$\min_{\boldsymbol{x}} \emptyset(\boldsymbol{P}\boldsymbol{x}) \quad subject\ to \quad \|\boldsymbol{B}\boldsymbol{x} - \boldsymbol{y}\|_2^2 \leq \varepsilon \tag{72}$$

where $\emptyset : \mathbb{R}^n \rightarrow \overline{\mathbb{R}} = \mathbb{R}\{-\infty, +\infty\}$ is a regularization function, and $\varepsilon \geq 0$ is a parameter which depends on the noise variance. An equivalent unconstrained problem formulation is also given [54] as:

$$\min_{\boldsymbol{x}} \frac{1}{2}\|\boldsymbol{B}\boldsymbol{x}-\boldsymbol{y}\|_2^2 + \lambda\, \emptyset(\boldsymbol{P}\boldsymbol{x}) \tag{73}$$

for some $\lambda > 0$. Note that both the optimization problem for updating $\tilde{\tau}$ in equation (71) and the optimization problem for updating j^{eqv} in equation (67) are in this unconstrained form, and hence can be solved using the C-SALSA algorithm.

When we choose the regularization term $\emptyset(\boldsymbol{P}\boldsymbol{x})$ as $\|\boldsymbol{P}\boldsymbol{x}\|_1$ to impose total variation (TV) regularization, the algorithmic steps of C-SALSA are as given in Table 3.1. The parameters κ, ε, μ should be chosen properly to enable convergence to the desired solution as discussed in the next section.

Table 3.1. Algorithmic steps of C-SALSA method

Algorithm C-SALSA

1. $Set\ k = 0, choose\ \kappa, \varepsilon, \mu > 0,\ \boldsymbol{v}_0^{(1)}, \boldsymbol{v}_0^{(2)}, \boldsymbol{d}_0^{(1)}, \boldsymbol{d}_0^{(2)}$

2. **repeat**

3. $\boldsymbol{r}_k = \kappa \boldsymbol{P}^H\left(\boldsymbol{v}_k^{(1)} + \boldsymbol{d}_k^{(1)}\right) + \boldsymbol{B}^H(\boldsymbol{v}_k^{(2)} + \boldsymbol{d}_k^{(2)})$

4. $\boldsymbol{u}_{k+1} = (\kappa\, a\boldsymbol{P}^H\boldsymbol{P} + \boldsymbol{B}^H\boldsymbol{B})^{-1}\boldsymbol{r}_k$

5. $\boldsymbol{v}_{k+1}^{(1)} = \psi_{\frac{\emptyset}{\mu}}\left(\boldsymbol{P}\boldsymbol{u}_{k+1} - \boldsymbol{d}_k^{(1)}\right) = soft\left(\boldsymbol{P}\boldsymbol{u}_{k+1} - \boldsymbol{d}_k^{(1)}, \frac{1}{\mu}\right)$

6. $\boldsymbol{v}_{k+1}^{(2)} = \psi_{l_{E(\varepsilon,I,y)}}\left(\boldsymbol{B}\boldsymbol{u}_{k+1} - \boldsymbol{d}_k^{(2)}\right)$

$$= \boldsymbol{y} + \begin{cases} \in \dfrac{\boldsymbol{B}\boldsymbol{u}_{k+1} - \boldsymbol{d}_k^{(2)} - \boldsymbol{y}}{\left\|\boldsymbol{B}\boldsymbol{u}_{k+1} - \boldsymbol{d}_k^{(2)} - \boldsymbol{y}\right\|_2}, if\ \left\|\boldsymbol{B}\boldsymbol{u}_{k+1} - \boldsymbol{d}_k^{(2)} - \boldsymbol{y}\right\|_2 > \varepsilon \\ \boldsymbol{B}\boldsymbol{u}_{k+1} - \boldsymbol{d}_k^{(2)} - \boldsymbol{y}, if\ \left\|\boldsymbol{B}\boldsymbol{u}_{k+1} - \boldsymbol{d}_k^{(2)} - \boldsymbol{y}\right\|_2 \leq \varepsilon \end{cases}$$

7. $\boldsymbol{d}_{k+1}^{(1)} = \boldsymbol{d}_k^{(1)} - \boldsymbol{P}\boldsymbol{u}_{k+1} + \boldsymbol{v}_{k+1}^{(1)}$

8. $\boldsymbol{d}_{k+1}^{(2)} = \boldsymbol{d}_k^{(2)} - \boldsymbol{B}\boldsymbol{u}_{k+1} + \boldsymbol{v}_{k+1}^{(2)}$

9. $k \leftarrow k+1$

10. **until** stopping criterion is satisfied.

C-SALSA algorithm is implemented in MATLAB with TV regularization. In the initial experiments, this algorithm is used for the solution of each subproblem in the alternating minimization approach to successively update $\tilde{\tau}$ and j^{eqv}. To solve the optimization problem in (67) for j^{eqv}, the variables in the C-SALSA algorithm are defined as follows:

$$\boldsymbol{B} = \begin{bmatrix} [T] \\ \sqrt{\propto}\,[G^S - \tilde{\tau}'_{diag}] \end{bmatrix}$$

$$\boldsymbol{y} = \begin{bmatrix} [e^{obs}] \\ -\sqrt{\propto}\,[e^i] \end{bmatrix} \tag{74}$$

$\boldsymbol{x} = [\,j^{eqv}]$ to be determined
$\boldsymbol{u_k}$: iterative solution for $\boldsymbol{x}$
$\boldsymbol{P} = \boldsymbol{P_{j^{eqv}}}$, derivative operator calculated over j^{eqv}.
$\boldsymbol{v_0^{(1)}} = \boldsymbol{P u_0}, \boldsymbol{v_0^{(2)}} = \boldsymbol{B u_0}$, $\boldsymbol{d_0^{(1)}}$, $\boldsymbol{d_0^{(2)}} = 0$
α: weighting coefficient

To solve the optimization problem in (70) for $\tilde{\tau}$, the variables in the C-SALSA algorithm are defined as follows:

$$\boldsymbol{B} = \begin{bmatrix} [j_{diag}^{eqv}] \end{bmatrix} \begin{bmatrix} [I]_{NxN} \\ [I]_{NxN} \\ [I]_{NxN} \end{bmatrix},$$

$\boldsymbol{y} = [G^S]\,[j^{eqv}] + [e^i]$,
$\boldsymbol{x} = \tilde{\tau}$ to be determined, (75)
$\boldsymbol{u_k}$: iterative solution for $\boldsymbol{x}$,
$\boldsymbol{P} = \boldsymbol{P_{\tilde{\tau}}}$, derivative operator calculated over $\tilde{\tau}$,
$\boldsymbol{v_0^{(1)}} = \boldsymbol{P u_0}, \boldsymbol{v_0^{(2)}} = \boldsymbol{B u_0}$, and $\boldsymbol{d_0^{(1)}}$, $\boldsymbol{d_0^{(2)}} = 0$

Sample results obtained with the developed solution method are presented in the following sections.

3.3.2 Parameter Selection

The parameters of the algorithm (κ, μ, ε and α) should be properly chosen and optimized for each problem when we deal with an imaging system with different characteristics such as different number of antennas, placement of antennas, polarization variety, object size, operating frequency, etc. Therefore, for each alternating minimization step, the coefficient κ, the threshold parameter μ are optimized using a grid search. To achieve this, the relative error is calculated by the following formula:

$$e_k = \frac{\|x_k - x_{original}\|_2^2}{\|x_{original}\|_2^2} \tag{76}$$

where x_k and $x_{original}$ are the estimated and original distributions of the current density (j^{eqv}) or electrical properties parameter ($\tilde{\tau}$) of the object. Then, two-dimensional error plots for a range of κ and μ values are obtained, and the optimum $\kappa - \mu$ pair is chosen as the grid corresponding to minimum error.

Noise related parameter ε is determined by evaluating the ℓ_2 norm of differences between e^{obs} values acquired from HFSS simulations and values computed analytically in MATLAB. The weighting factor α, which is the measure of the contribution of two distinct minimization terms to estimate j^{eqv}, is determined after a few iterations once the other parameters are set as described above.

For the first step that updates the current density distribution, the optimal parameters are obtained as $\kappa_j = 10^{-6}$ and $\mu_j = 100$ as shown in Figure 3.1, which presents the error for the current density distribution for different values of κ_j and μ_j. In this step, the permittivity and conductivity distribution is assumed to be known exactly. Using their true values, parameter optimization is performed only for updating the single variable, j^{eqv}.

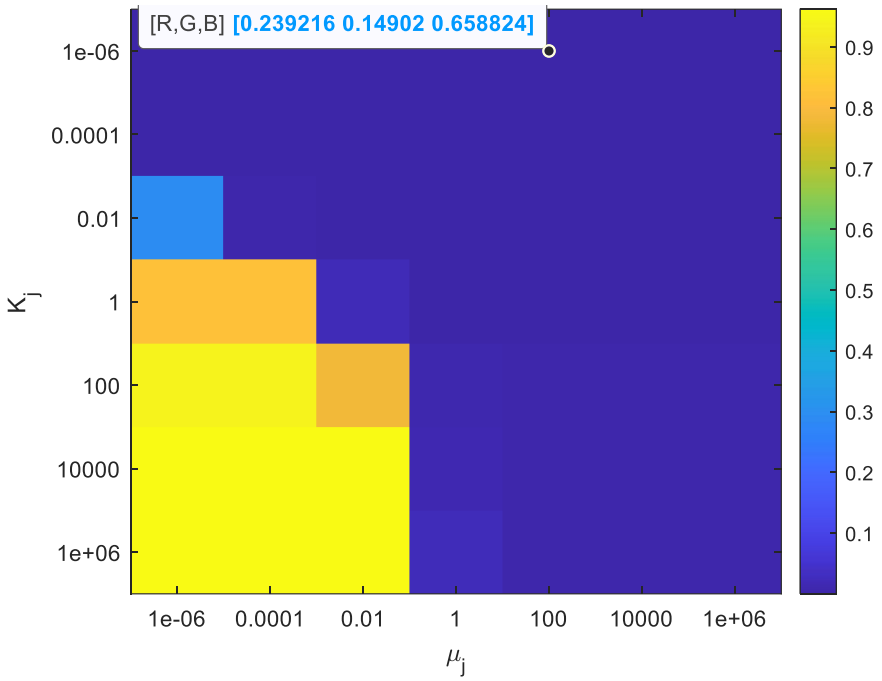

Figure 3.1. Error for j^{eqv}distribution with respect to C-SALSA parameters κ_j and μ_j

Above procedure for parameter selection is repeated for the update step of the variable $\tilde{\tau}$. The optimal values of the coefficient κ and the threshold parameter μ are determined as $\kappa_{\tilde{\tau}} = 100$ and $\mu_{\tilde{\tau}} = 1000$ as shown in Figure 3.2 which presents the error for $\tilde{\tau}$ for different values of $\kappa_{\tilde{\tau}}$ and $\mu_{\tilde{\tau}}$. It should also be noted that as seen in Figure 3.1 and Figure 3.2 the error is not too sensitive to the parameter selection as desired. Hence the parameters can be selected from a relatively broad region without much change in the performance. The weighting coefficient α is found to be 10^{-4}.

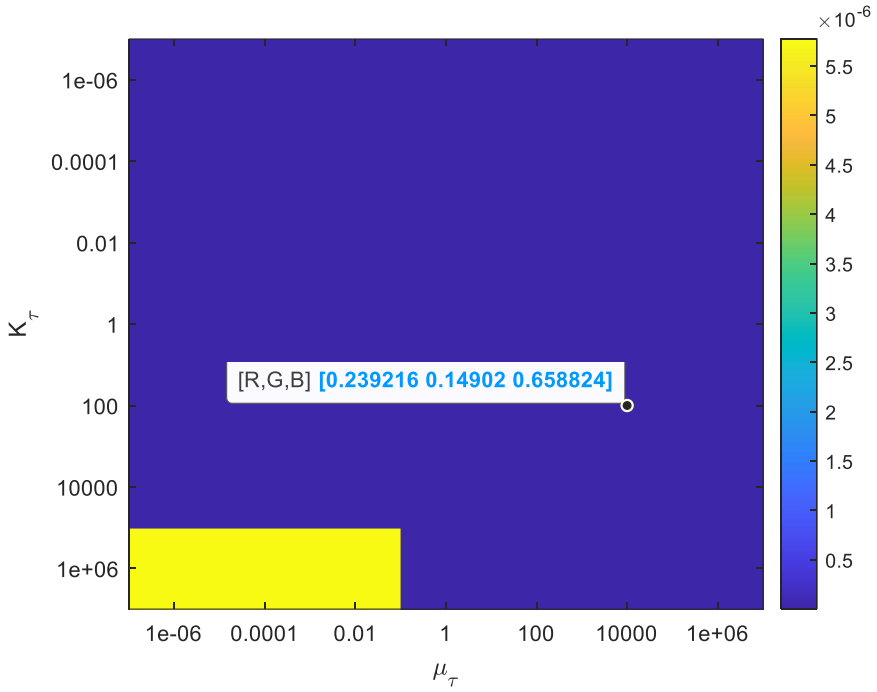

Figure 3.2. Error for $\tilde{\tau}$ distribution with respect to C-SALSA parameters $\kappa_{\tilde{\tau}}$ and $\mu_{\tilde{\tau}}$

After parameter selection, alternating minimization method is executed for image reconstruction using C-SALSA algorithm for the update steps. To evaluate the convergence speed of the algorithm, for each variable, relative change is defined with the formula

$$\Delta_k = \frac{\|x_k - x_{k-1}\|_2}{\|x_{k-1}\|_2} \tag{77}$$

where x is either the current density (j^{eqv}) or electrical properties parameter ($\tilde{\tau}$) of the object and k is the iteration number. Figure 3.3 illustrates the relative change in the current density and electrical properties parameter ($\tilde{\tau}$) values with respect to iterations, along with the relative errors at each iteration.

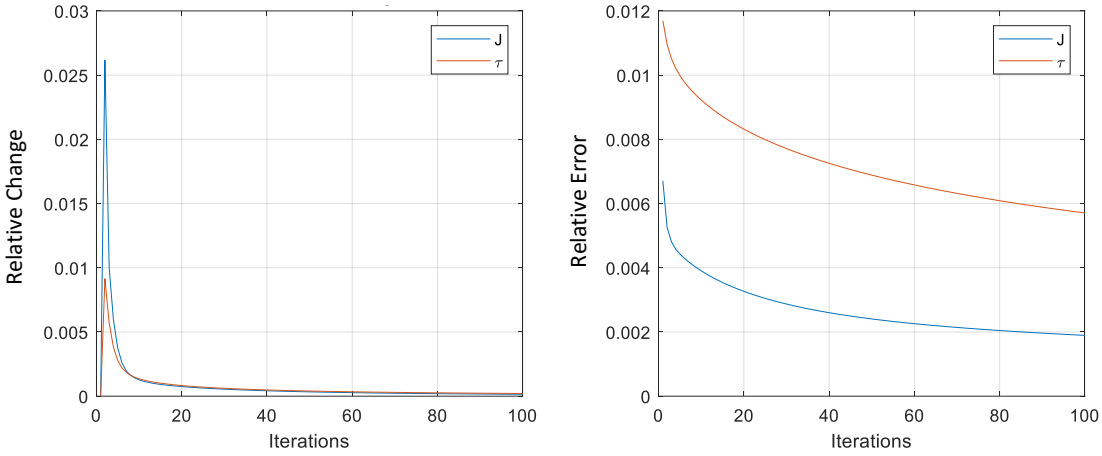

Figure 3.3. (a) Relative change and (b) relative error with respect to iterations

Using C-SALSA approach for both alternating minimization steps increases the computation time. Since the problem related to the current density variable is relatively well-determined as it involves both state and data equations, we can omit the regularization term, $R(j^{equ})$, for the current density from equation (67) and employ a simple iterative solver like least squares (LS) (instead of C-SALSA) for the first update step. This will speed up the overall reconstruction algorithm and also simplify the parameter selection procedure. For comparison, this approach is applied to the same problem above, and relative change and relative error results are presented in Figure 3.4. The threshold value shown in the figure is used to stop the algorithm when relative change drops below this threshold. As it is observed from Figure 3.3 (b) and Figure 3.4 (b), this faster approach results in better relative errors for both variables. Therefore, this method is pursued to solve the inverse problem in this thesis. That is, the first alternating minimization step for updating the current density is solved using LS solver (Conjugate-Gradient) without employing regularization, and the second alternating minimization step for updating the electrical properties is solved using C-SALSA solver as discussed above.

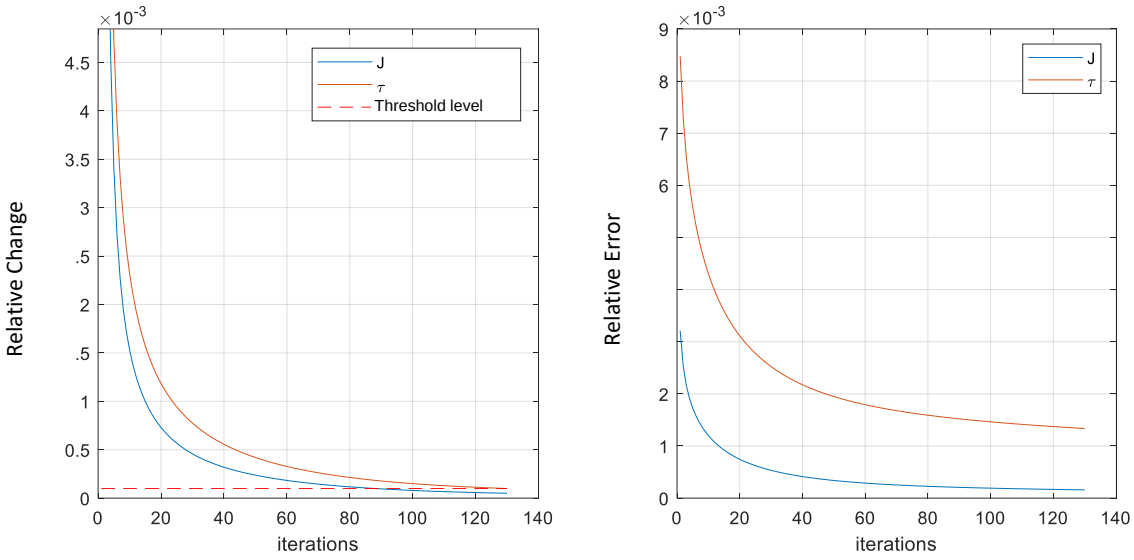

Figure 3.4. (a) Relative change and (b) relative error distributions with respect to iterations

CHAPTER 4

IMAGE RECONSTRUCTION WITH HERTZIAN DIPOLE ANTENNAS

After formulating the forward and inverse problems, it is necessary to test the performance of the image reconstruction algorithm under different observation scenarios. The studies in this thesis have been conducted starting from simple configurations and progressing towards a more complex setting that closely resembles a realistic head model. In these investigations, first, Hertzian dipole antennas have been employed since they both exhibit near-field radiation characteristics and can be expressed analytically, such that they effectively and efficiently fit into the solution method. The impact of antenna placement and polarization types on the imaging performance has also been thoroughly examined at the end of this chapter. All simulations are performed at 1 GHz.

4.1 Simple Transmitter and Receiver Antenna Array Configurations

First, a simple configuration is studied and to obtain 3D image of a scatterer in the shape of rectangular prism, receiver and transmitter antennas are placed on all faces of a prism in order to gather a meaningful scattering information all-around the object. The effect of number of antennas and the polarization of antennas are studied in the following two sub-sections.

4.1.1 Performance Analysis with Different Number and Arrangement of Transmitter and Receiver Antennas

In order to compare the image reconstruction performances of different transmitter and receiver antenna arrangements, a number of simulations are performed, details of which are given in Table 4.1.

Table 4.1. Configuration details of various Tx/Rx antenna arrangements

Configuration No.	Number of Faces	Number of Tx/Rx Antennas on Each Face	Total Number of Tx/Rx Antennas	Antenna Array Topology on Each Face
1	6	4	24	2 x 2 (2D)
2	4	4	16	2 x 2 (2D)
3	4	4	16	4 x 1 (1D)
4	4	2	8	2 x 1 (1D)
5	4	1	4	-

The placement of the antennas and the object with respect to the above configurations are shown between Figure 4.1 and Figure 4.5. Blue and pink points represent transmitters and receivers, respectively. We consider a 3D scatterer object that consists of 8x8x2 cubic cells. There is a region of 2x2x2 cells occupied by blood ($\varepsilon_r^{blood} = 61.065$, $\sigma_r^{blood} = 1.583$) at the center of the object, whereas the remaining space is filled with white matter ($\varepsilon_r^{whitematter} = 38.578, \sigma_r^{whitematter} = 0.622$) .

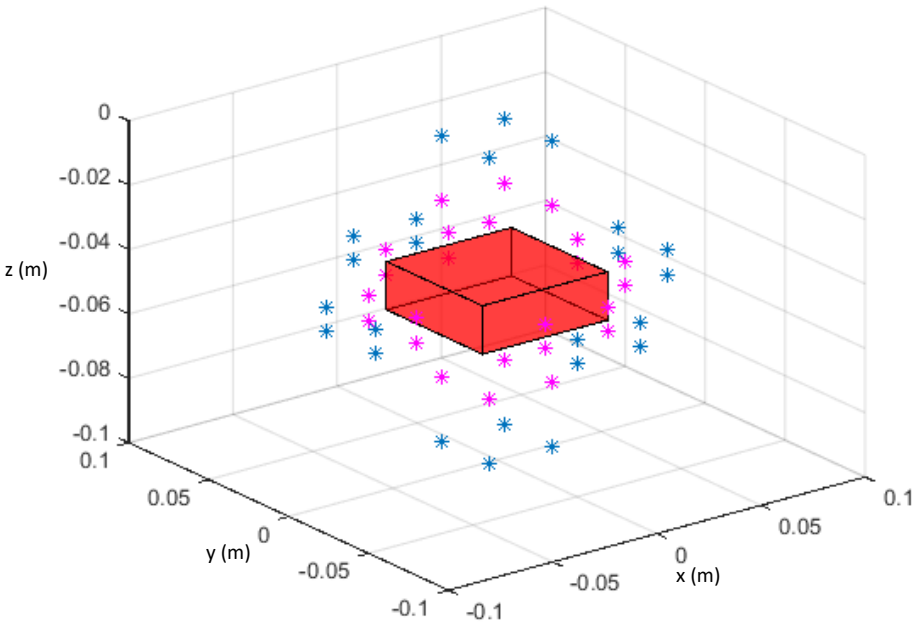

Figure 4.1. Transmitting and Receiving Antennas - Configuration No.1 (6 Faces x 4 Antennas - 2D Array)

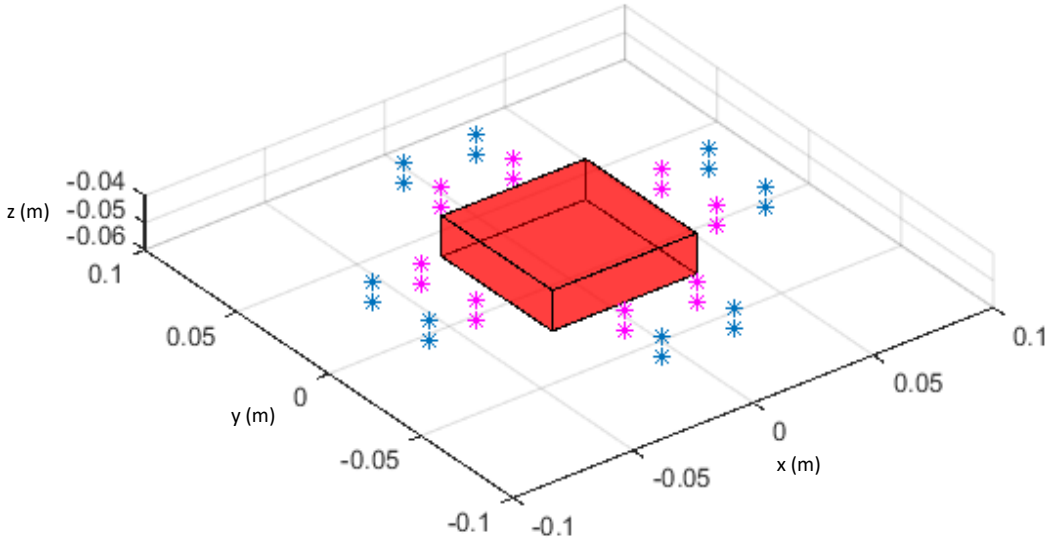

Figure 4.2. Transmitting and Receiving Antennas - Configuration No.2 (4 Faces x 4 Antennas - 2D Array)

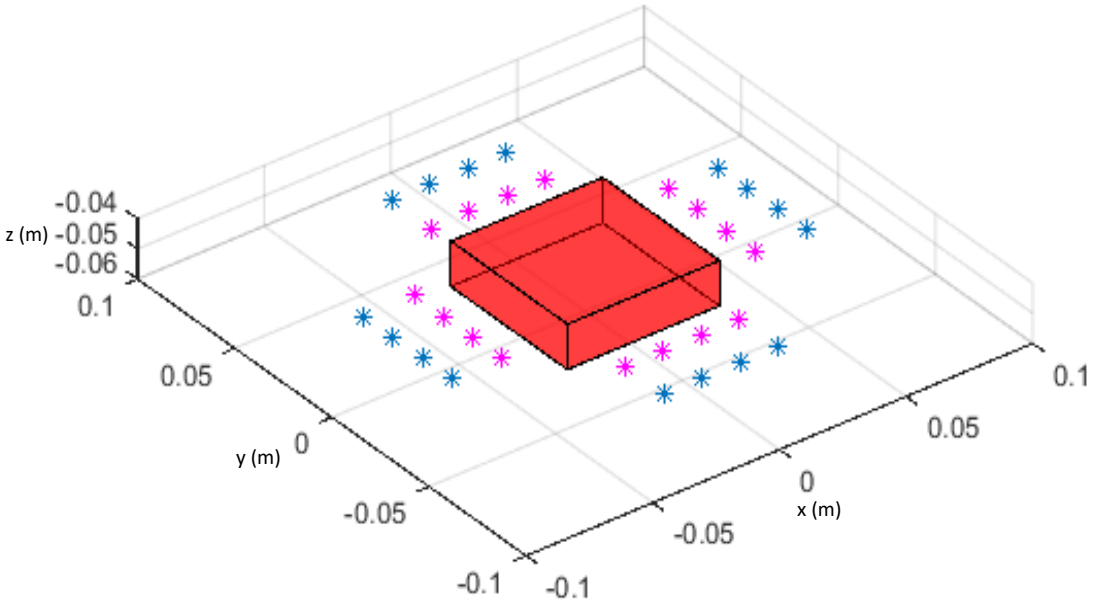

Figure 4.3. Transmitting and Receiving Antennas - Configuration No.3 (4 Faces x 4 Antennas - 1D Array)

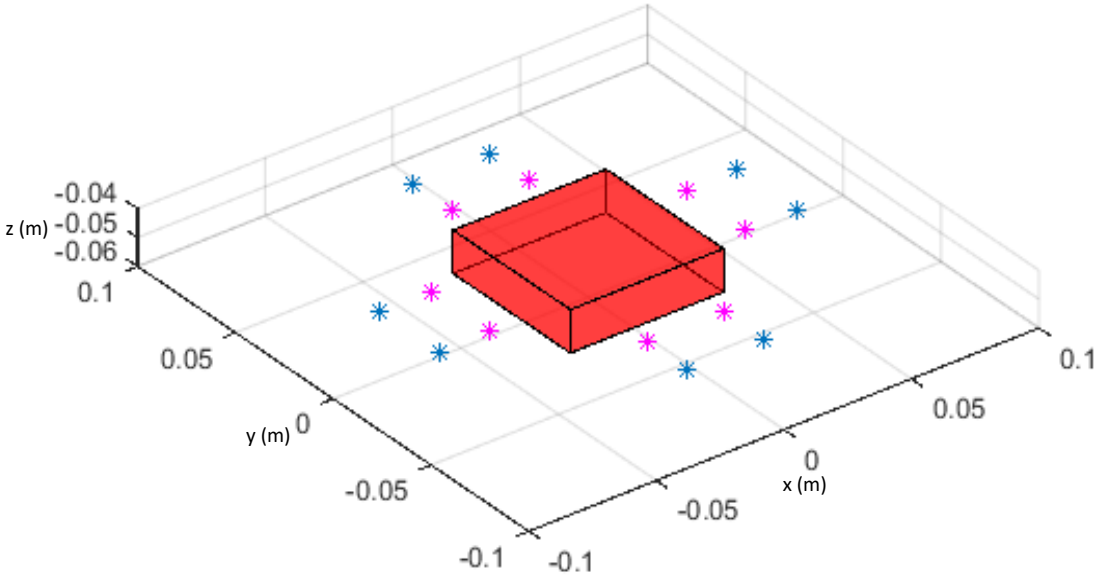

Figure 4.4. Transmitting and Receiving Antennas - Configuration No.4 (4 Faces x 2 Antennas - 1D Array)

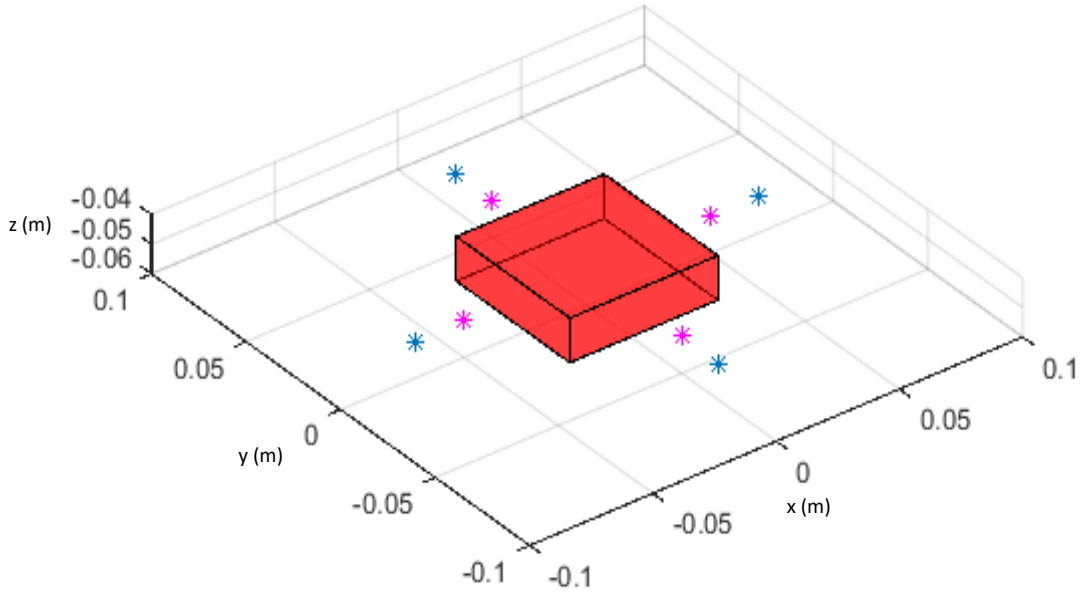

Figure 4.5. Transmitting and Receiving Antennas - Configuration No.5 (4 Faces x 1 Antenna)

The image reconstruction process is employed for all configurations defined above and the relative error characteristics are given in Figure 4.6. As it is observed from Figure 4.6, the minimum relative error for both j^{eqv} and τ distributions is obtained by Configuration No.1, which employs Tx/Rx antennas placed on all six faces of the cubical object with a 2x2 array topology. It is also inspected that as the total number of antennas decreases, the relative errors exhibit an increasing trend. The comparison of configurations having the same number of antenna pairs, reveals the effect of the antenna array topology. Despite the fact that both 4 faces x 4 antennas - 2D array and 4 faces x 4 antennas - 1D array configurations have the same number of Tx and Rx antennas, 2D (2x2) array topology provides more spatial information and gives more accurate results. Relative change characteristics for different configurations are also presented in Figure 4.7. From the figure, it can be concluded that the number of antennas and their topology do not have a significant effect on the convergence of the results.

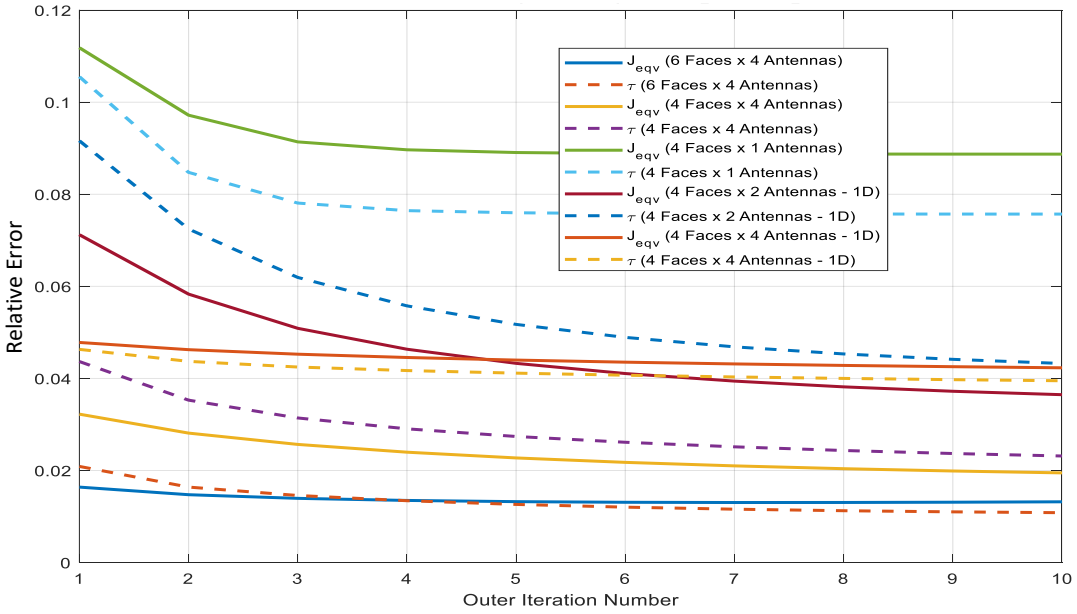

Figure 4.6. Relative error characteristics of j^{eqv} and $\boldsymbol{\tau}$ distributions for different source arrangements

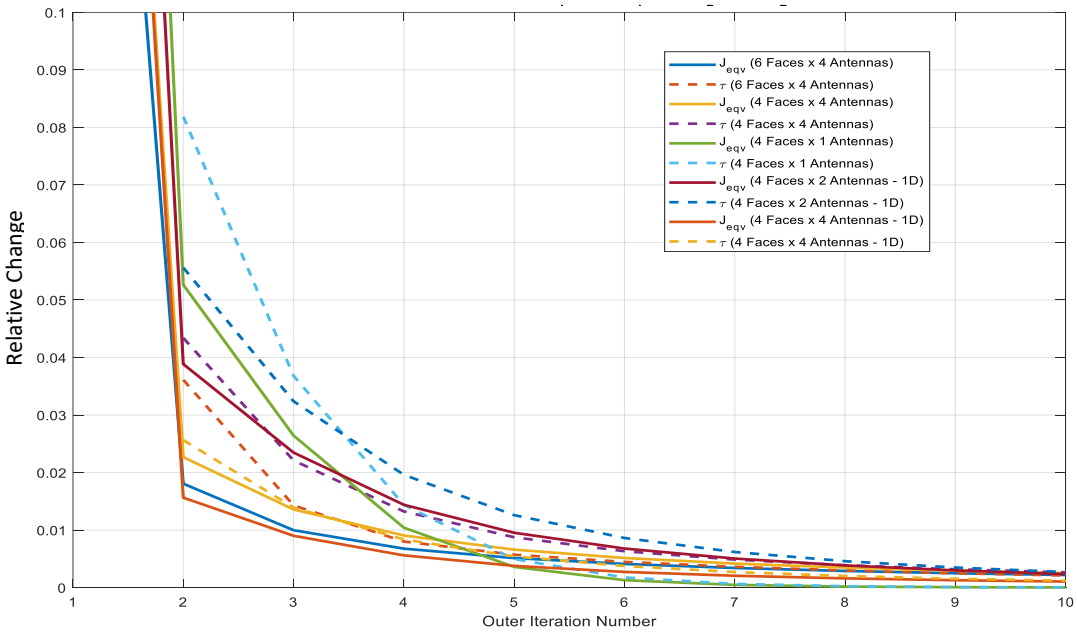

Figure 4.7. Relative change characteristics of j^{eqv} and $\boldsymbol{\tau}$ distributions for different source arrangements

4.1.2 Performance Analysis with Different Antenna Polarization Configurations

Up to this point, receiver antennas placed around the object are assumed to be polarization independent radiators, while the transmitter antennas are z-polarized only. In other words, at the receiving antenna positions, all components of electrical field vector are considered as measured field values. However, in the realistic scenario, the radiators have specific polarization characteristics for both transmitting and receiving situations. In order to have a practically applicable image reconstruction algorithm, the polarization characteristics of the transmitting and receiving antennas are incorporated into the forward solution algorithm. First of all, near field radiation pattern of a Hertzian dipole antenna which has arbitrary polarization at an arbitrary position in the space (see equation (44)) is utilized by the help of the Symbolic Math Toolbox of MATLAB. Afterwards, it is straightforward to define the position and polarization of the antennas arbitrarily with respect to that formulation. The forward and related inverse problem solutions are studied for different antenna polarization configurations in order to observe and compare the performance of the image reconstruction algorithm under different scenarios. The configuration named as “Polarization 1” is demonstrated in Figure 4.8. Transmitter and receiver antenna pairs have the same polarity. It is important that the polarization components are selected from the tangential components on the related object faces.

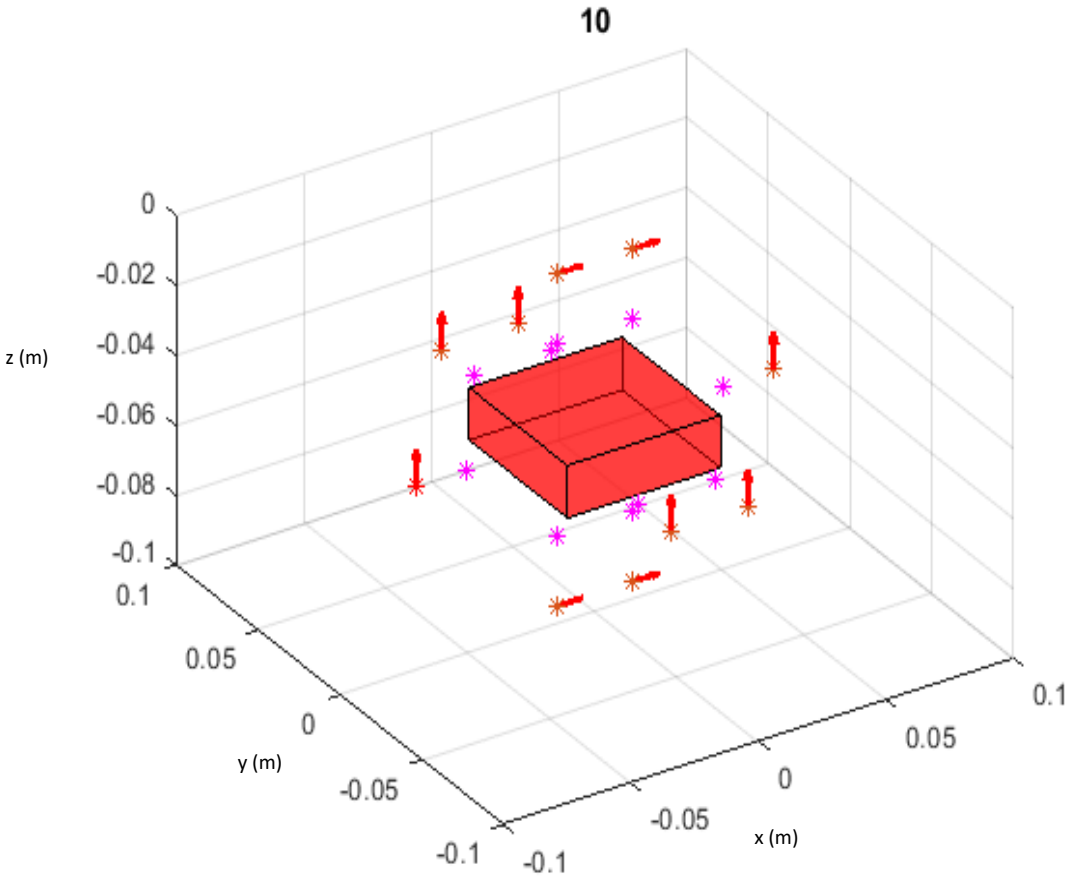

Figure 4.8. Transmitter/Receiver Antennas Single Polarization Configuration (Polarization 1)

“Polarization 2” is constructed by the complement of the “Polarization 1” which is also tangential on the object face for each antenna (See Figure 4.9).

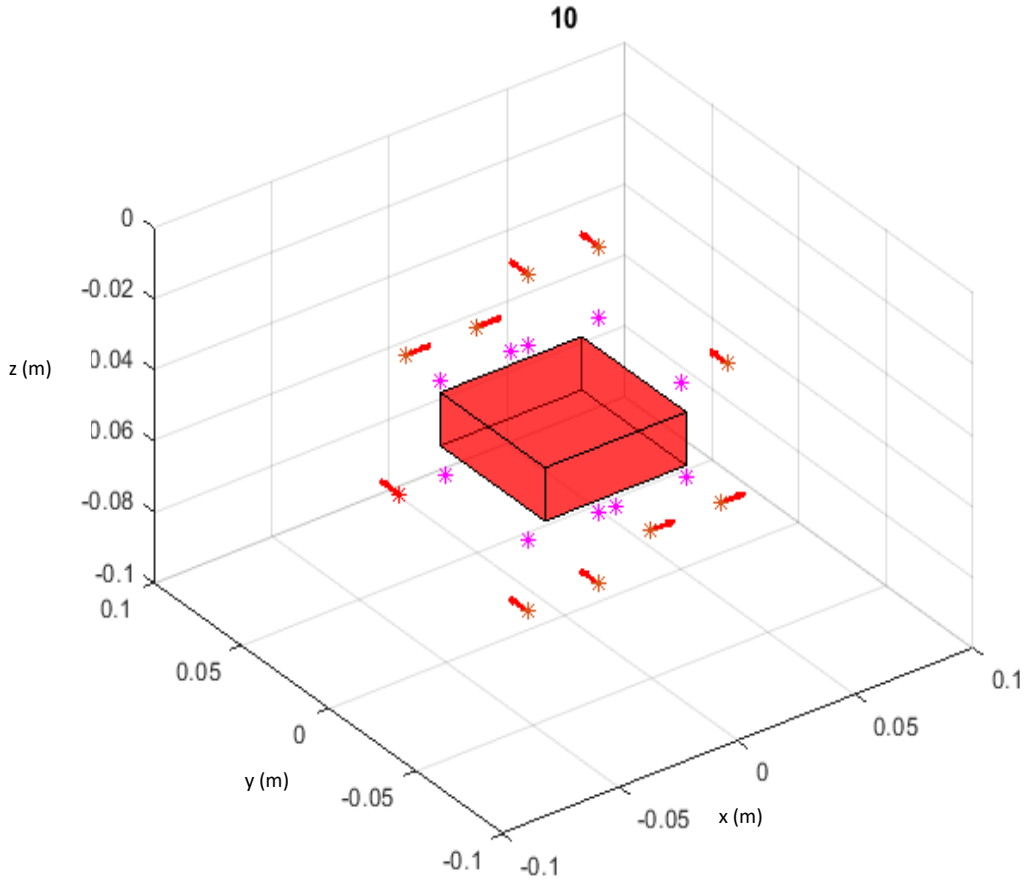

Figure 4.9. Transmitter/Receiver Antennas Single Polarization Configuration (Polarization 2)

"Dual Polarization" configuration is also implemented in order to observe the effect of the dual polarized transmitters and receivers on the performance of the image reconstruction algorithm (see Figure 4.10).

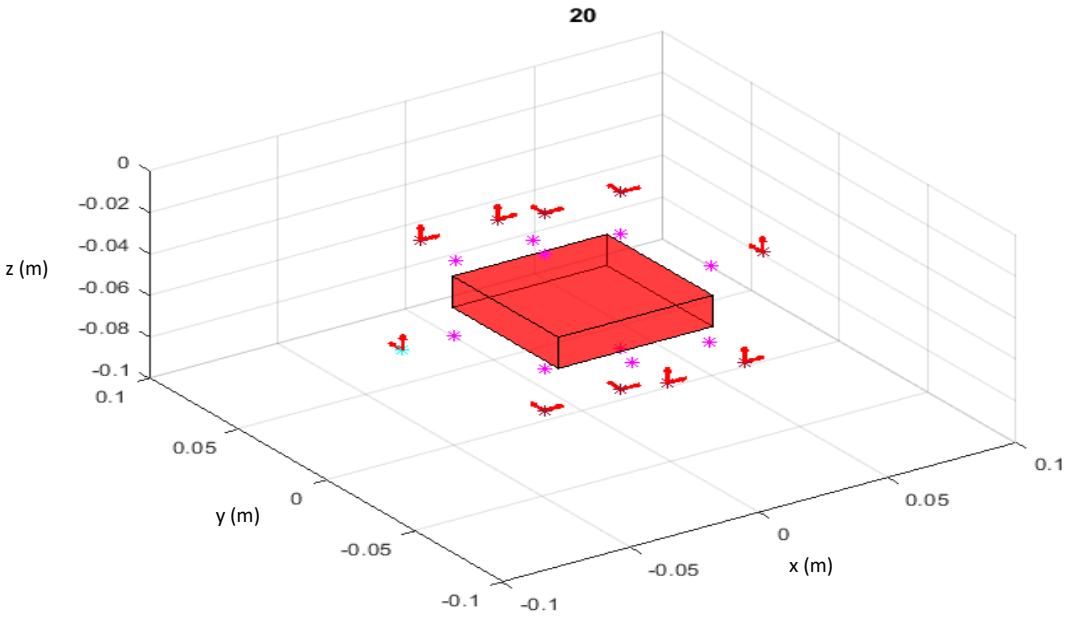

Figure 4.10. Transmitter/Receiver Antennas Dual Polarization Configuration

A single polarized antenna arrangement consisting of only normal components is called “Polarization 3” and shown in Figure 4.11.

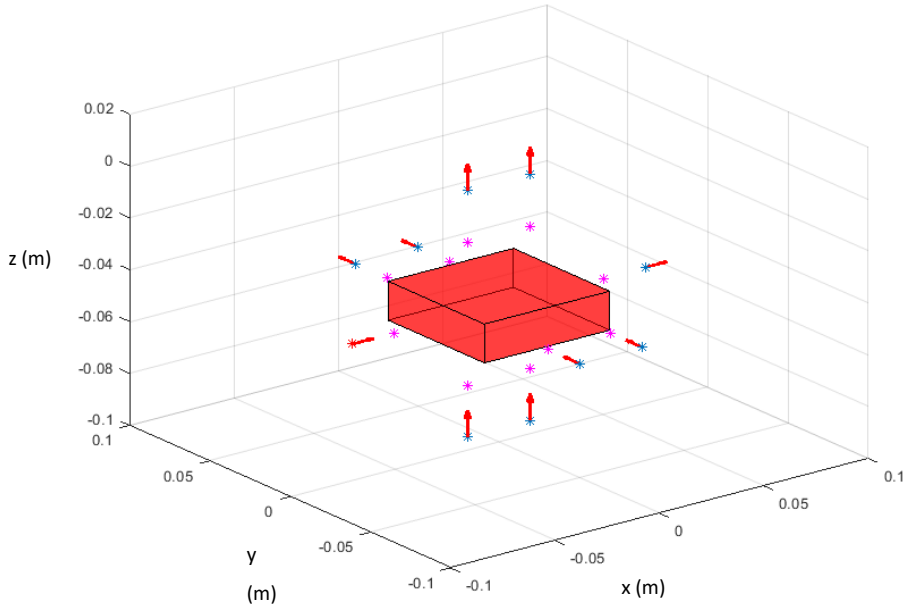

Figure 4.11. Transmitter/Receiver Antennas Single Polarization Configuration (Polarization 3)

Finally, the combination of all single polarized configurations called as “Triple Polarization” is also studied in order to compare the image reconstruction performance (see Figure 4.12).

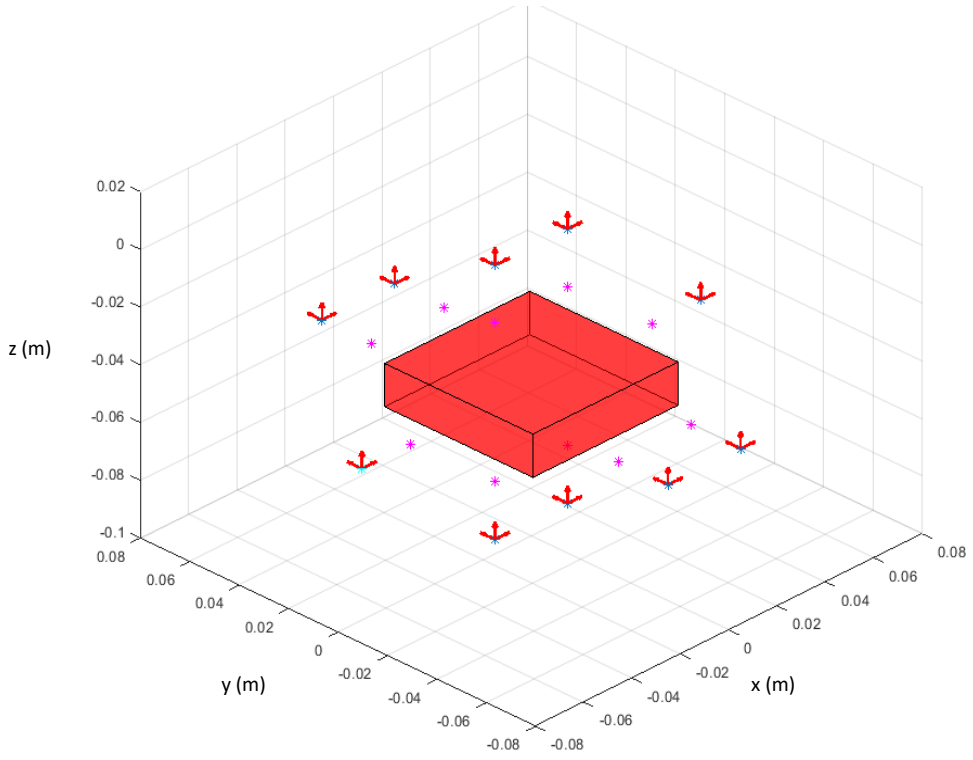

Figure 4.12. Transmitter/Receiver Antennas Triple Polarization Configuration

Relative change and relative error characteristics of the predicted distributions for current density (j^{eqv}) and electrical properties parameter (τ) of the object are presented between Figure 4.13 and Figure 4.16 with respect to different antenna polarization configurations defined above.

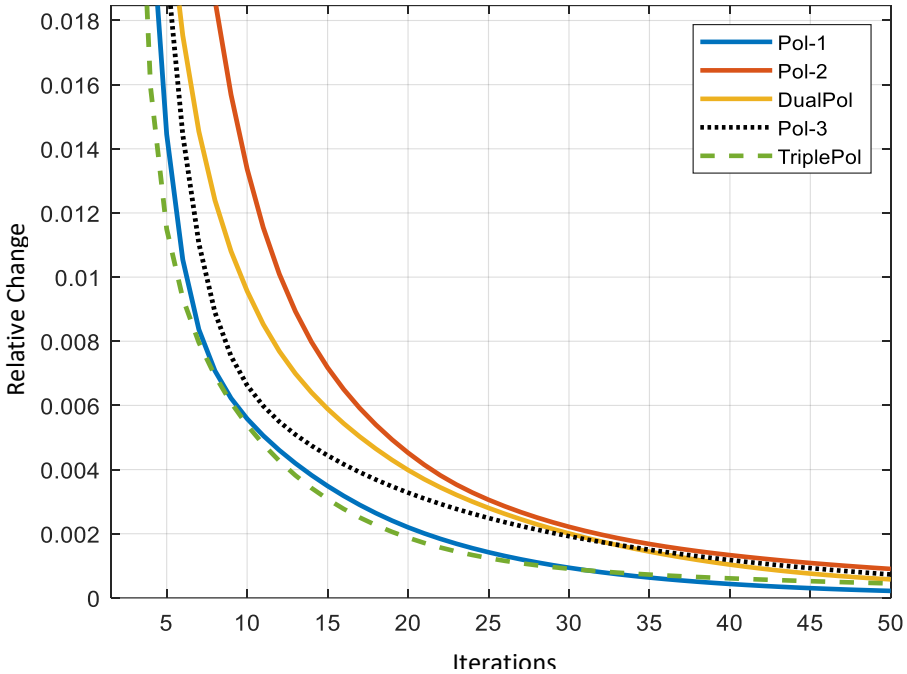

Figure 4.13. Relative change characteristics of predicted j^{eqv} distribution over 50 iterations for different polarization configurations

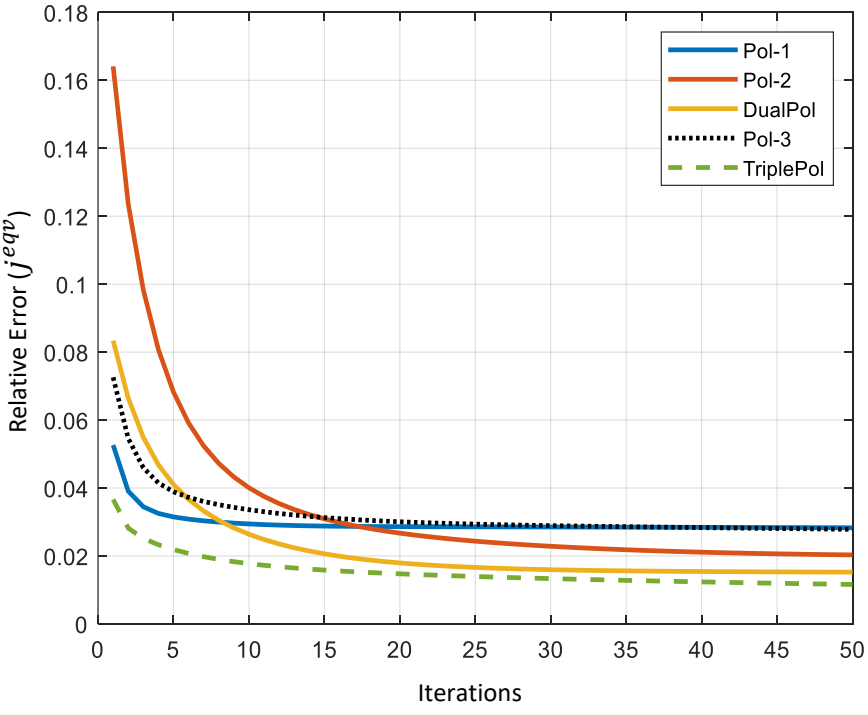

Figure 4.14. Relative error characteristics of predicted j^{eqv} distribution over 50 iterations for different polarization configurations

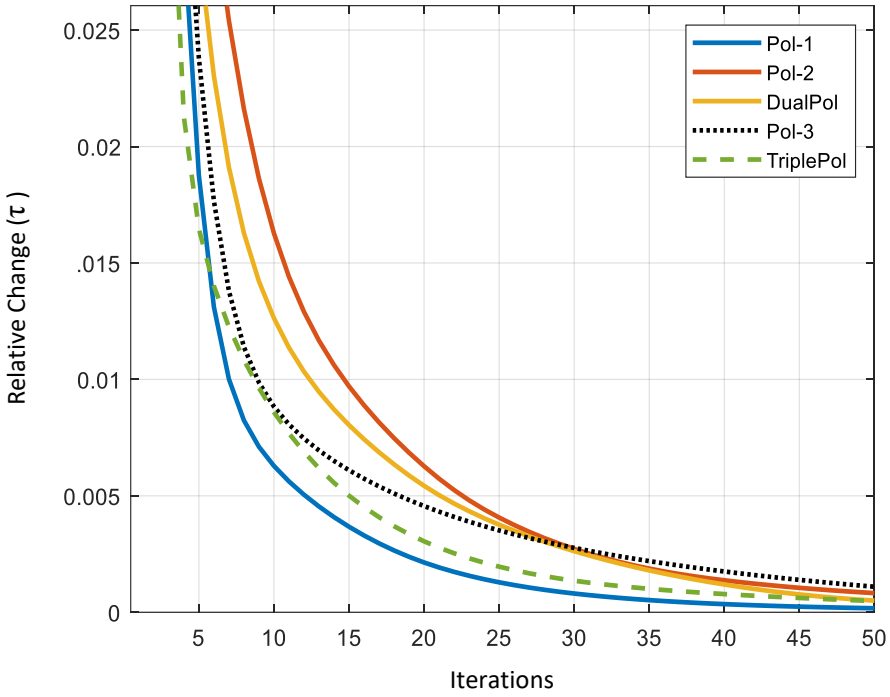

Figure 4.15. Relative change characteristics of predicted τ distribution over 50 iterations for different polarization configurations

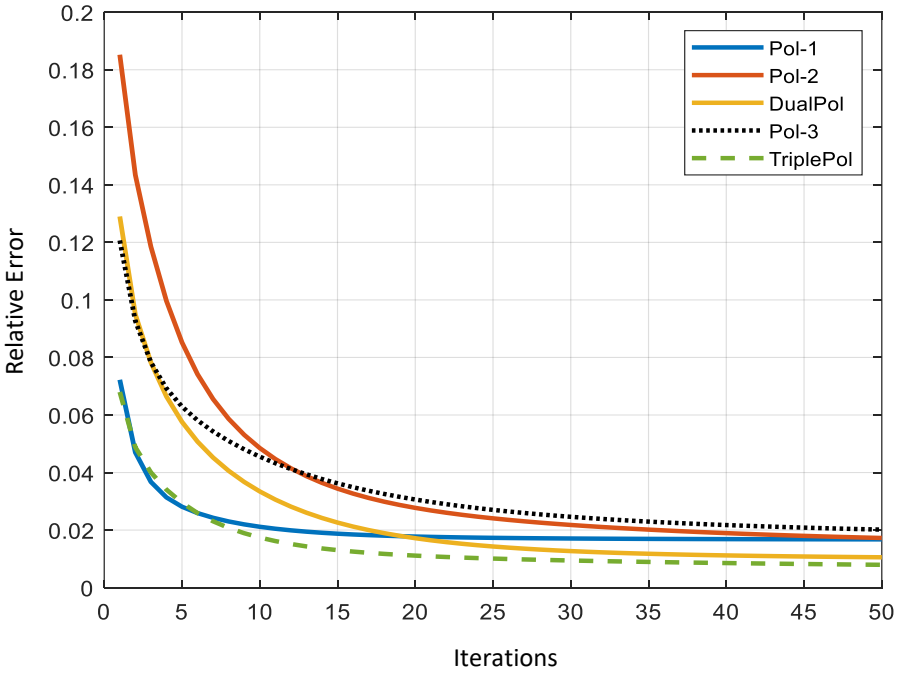

Figure 4.16. Relative error characteristics of predicted τ distribution over 50 iterations for different polarization configurations

The above results reveal that a single polarized antenna arrangement that is composed of one of the tangential components on the object face (Pol-1 and Pol-2) gives similar results for τ distribution. Dual Polarization solution is better in terms of error characteristics performance as expected since the number of measurements is doubled with respect to single polarization case. The results of Polarization 3 are slightly worse than Polarization 1 and Polarization 2 solutions as expected since tangential field components on a closed surface involve more information than the normal components. For the Triple Polarization case, the error terms for j^{eqv} and τ are not considerably better than Dual Polarization solution. Hence, it is not worth increasing the computational complexity by using triple polarization, but it is worth for the computational cost introduced by dual polarization.

In terms of computation cost, incorporating a second polarization on an existing single polarized antenna system is equal to doubling the number of antennas in the system. In this study, the performance parameters for two different scenarios which are equal in computational cost, are determined and compared. In the first case, there are 10 dual polarized antennas around the cubical object (see Figure 4.17), while there exist 20 single polarized antennas for the second case as shown in Figure 4.18. The main difference between the two cases is diversity in polarization and spatial distribution.

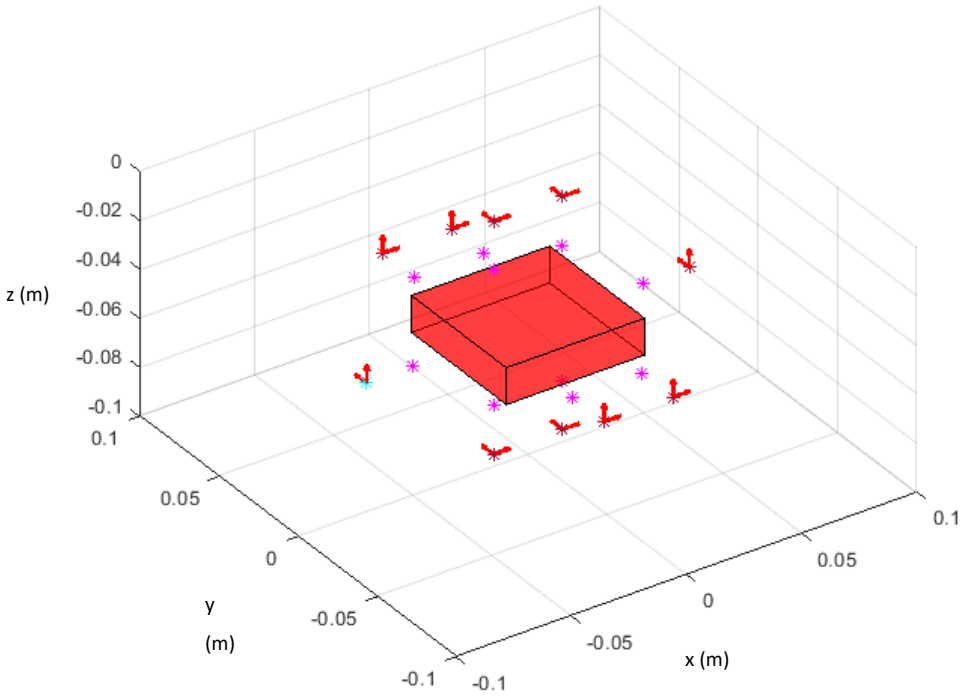

Figure 4.17. Transmitter/Receiver Antennas Polarization Configuration (Dual Polarized 10 Antennas)

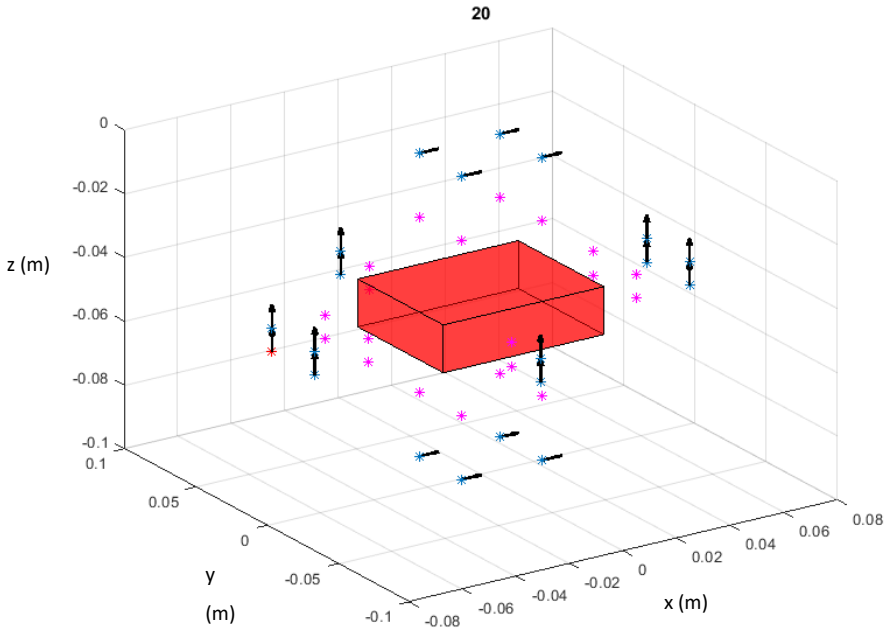

Figure 4.18. Transmitter/Receiver Antennas Polarization Configuration (Single Polarized 20 Antennas)

According to the results given in Figure 4.19 to Figure 4.22, there is no significant difference between the two configurations in terms of relative change characteristics for both j^{eqv} and τ variables. On the other hand, the dual polarized N-antennas configuration, where N is equal to 10, gives better error values when compared to single-polarized 2N antennas, especially in terms of τ variable. Therefore, it is noted that polarization diversity gives better results than the spatial diversity under same calculation cost conditions.

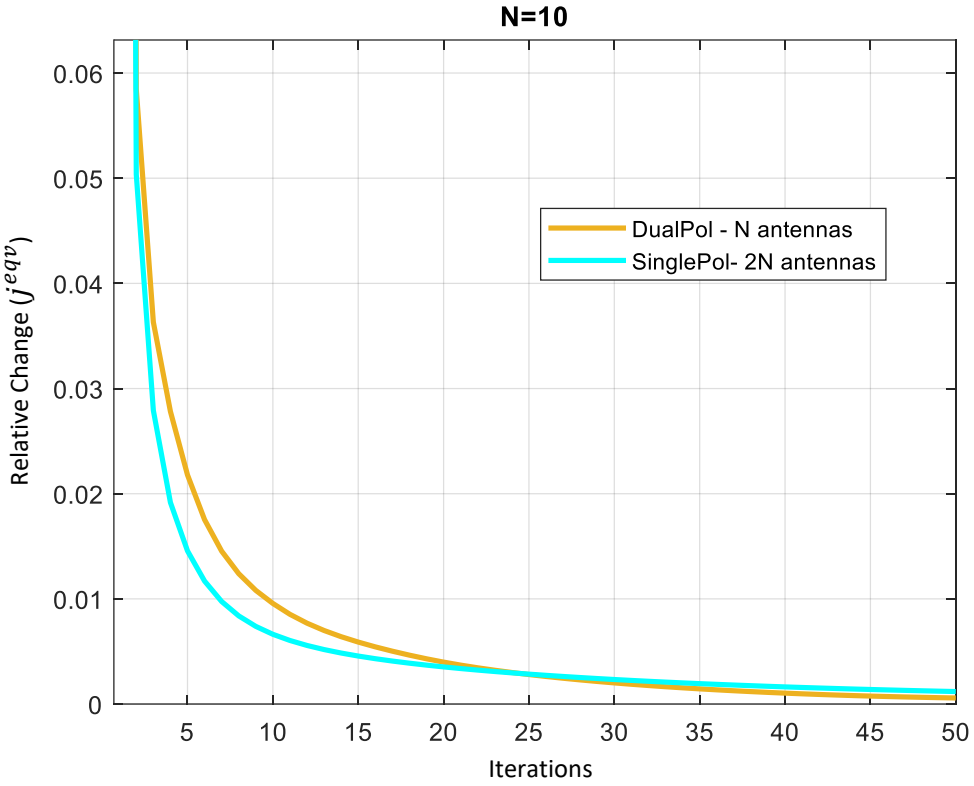

Figure 4.19. Relative change characteristics of predicted j^{eqv} distribution over 50 iterations for different polarization configurations

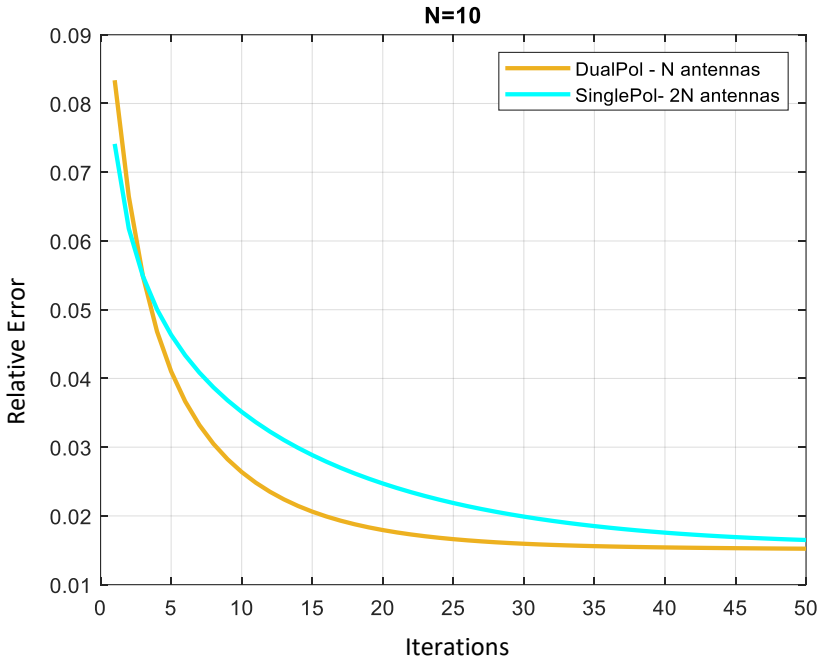

Figure 4.20. Relative error characteristics of predicted j^{eqv} distribution over 50 iterations for different polarization configurations

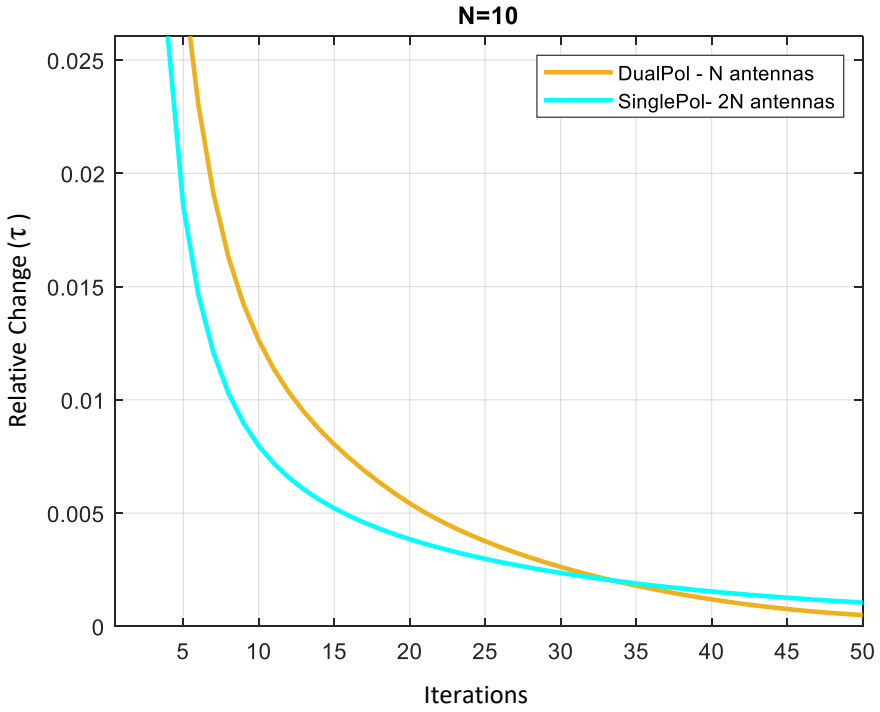

Figure 4.21. Relative change characteristics of predicted τ distribution over 50 iterations for different polarization configurations

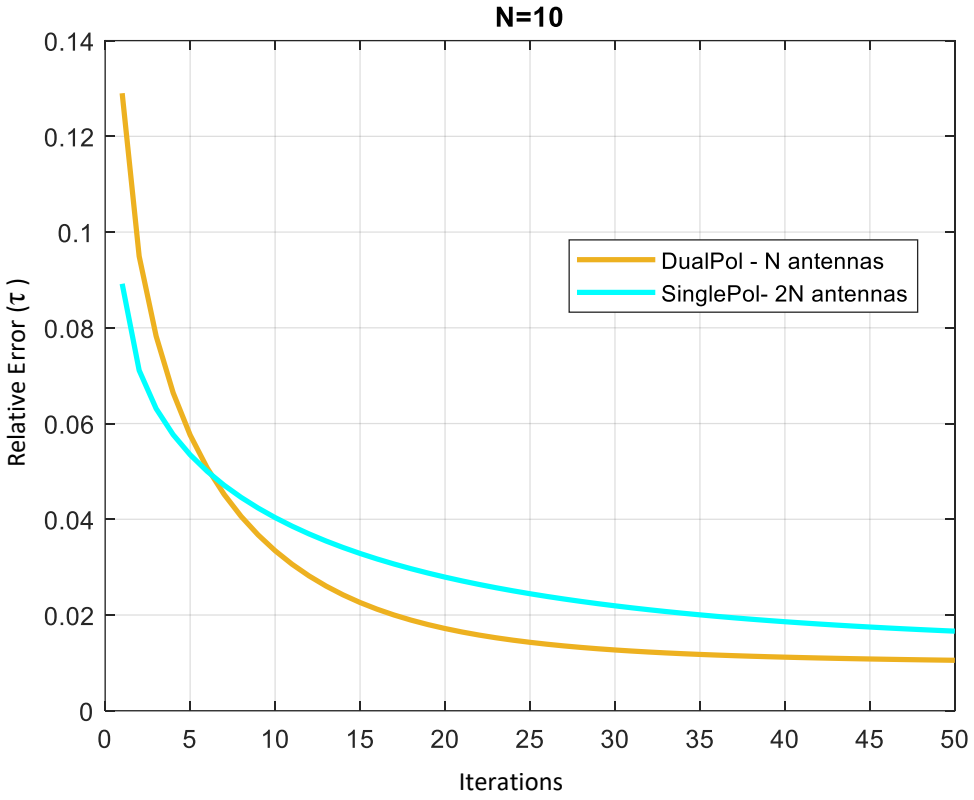

Figure 4.22. Relative error characteristics of predicted τ distribution over 50 iterations for different polarization configuration

In order to conduct a visual evaluation of the reconstructed images by single polarized and dual polarized configurations, contrast characteristics for relative permittivity and conductivity profiles are calculated by the formula

$$Contrast_n = \frac{|\alpha_{n,reconstructed} - \alpha_{n,whitematter}|}{|\alpha_{n,whitematter}|} \quad (78)$$

where α_n is the value of either relative permittivity ε_r or conductivity σ of n^{th} cell.

Note that, to detect the type of brain stroke, the important thing is the shape of the region with blood. Hence, rather than the absolute permittivity and conductivity values obtained after reconstruction, the contrast values with respect to healthy brain tissues (white matter) are more important.

As it is observed in in Figure 4.23 and Figure 4.24, the maximum contrast values and better detection performance are gathered by the dual polarized configuration which makes it superior when compared to its single polarized counterpart having the same calculation cost for the imaging system.

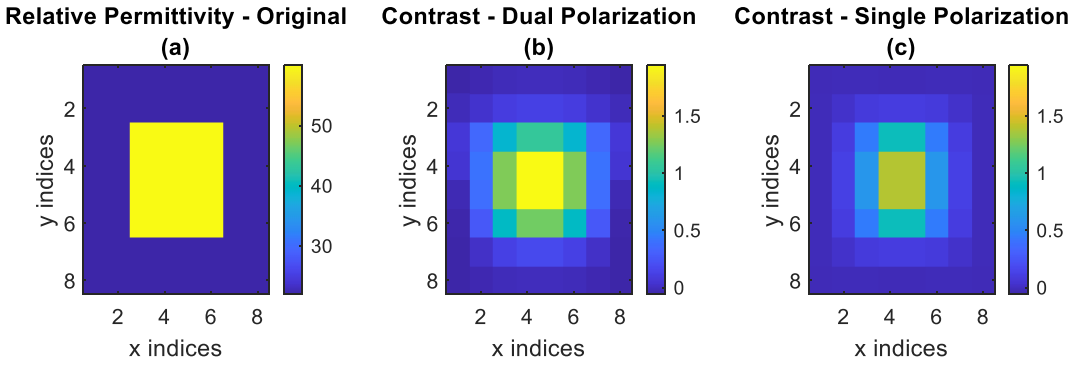

Figure 4.23. (a) Original relative permittivity distribution; relative permittivity contrast images for (b) dual polarization with 10 antennas, (c) single polarization with 20 antennas

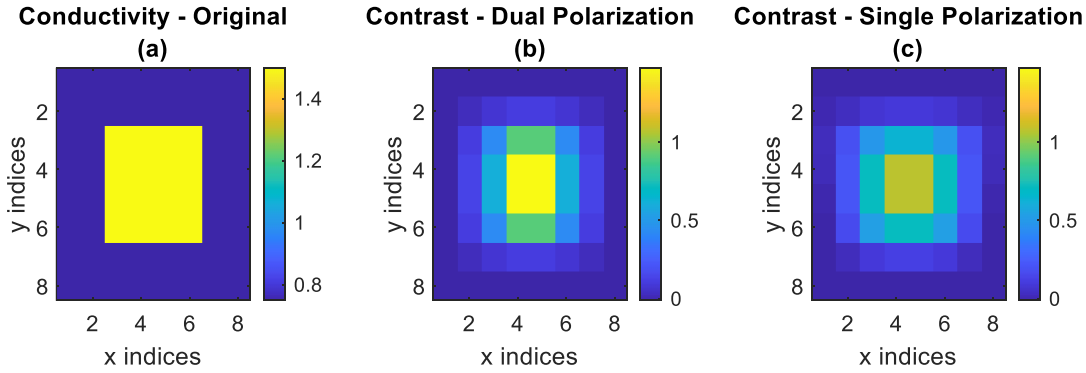

Figure 4.24. (a) Original conductivity distribution; conductivity contrast images for (b) dual polarization with 10 antennas, (c) single polarization with 20 antennas

4.2 Realistic Transmitter and Receiver Antenna Array Configuration

The main concern of the study is to construct a robust imaging system which is feasible and applicable to realistic scenarios. In order to realize such a system, antennas around the head are required to be positioned on a helmet-like surface conforming the shape of the human head. Furthermore, it is also necessary to have a

compact system which is not the case for the current bulky imaging systems like x-ray and MRI. Statistical data for the physical characteristics of the human head is given in [58] as demonstrated in Figure 4.25. The relevant parts of the head are "Bitragion breadth", "Glabella to back of head" and "Sellion to top of head", detailed definitions of which are also given in Figure 4.25.

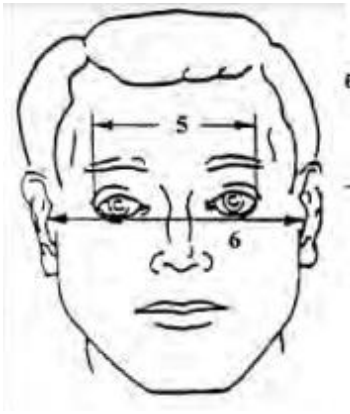

6 **Bitragion breadth.** The breadth of the head from the right tragion to the left. (Tragion is the cartilaginous notch at the front of the ear).

Sample			Percentiles 1st	5th	50th	95th	99th
A Men	cm	13.1	13.5	14.5	15.5	15.9
	(in)	(5.2)	(5.3)	(5.7)	(6.1)	(6.3)
B Women	cm	12.5	12.8	13.3	14.3	15.0
	(in)	(4.3)	(5.4)	(5.4)	(5.7)	(5.9)

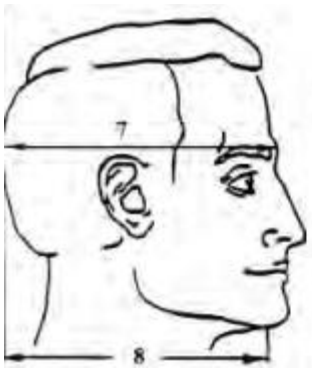

7 **Glabella to back of head.** The horizontal distance from the most anterior point of the forehead between the brow-ridges (glabella) to the back of the head, measured with a headboard.

Sample			Percentiles 1st	5th	50th	95th	99th
A Men	cm	18.3	18.8	20.0	21.1	21.7
	(in)	(7.2)	(7.4)	(7.9)	(8.3)	(8.5)
B Women	cm	17.5	18.0	19.1	20.2	20.7
	(in)	(6.9)	(7.1)	(7.5)	(8.0)	(8.1)

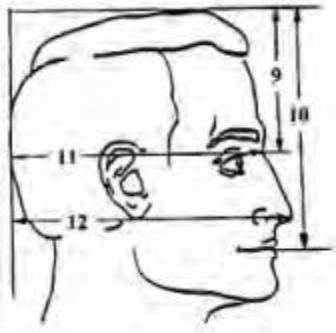

9 **Sellion to top of head.** The vertical distance from the nasal root depression between the eyes (sellion), to the level of the top of the head, measured with a headboard.

Sample			Percentiles 1st	5th	50th	95th	99th
A Men	cm	9.7	10.1	11.2	12.4	12.9
	(in)	(3.8)	(4.0)	(4.4)	(4.9)	(5.1)
B Women	cm	9.0	9.5	10.5	11.7	12.2
	(in)	(3.5)	(9.5)	(4.1)	(4.6)	(4.8)

Figure 4.25. Physical characteristics of human head [58]

As it is observed from Figure 4.25, the best conforming geometrical shape for the human head is an ellipsoid. Therefore, it is critical to place the transmitting and receiving antennas on an ellipsoidal surface maintaining the polarization characteristics.

Mathematical expression for the ellipsoidal surface can be defined as follows,

$$\frac{x^2}{a^2}+\frac{y^2}{b^2}+\frac{z^2}{c^2}=1 \tag{79}$$

together with the parametric equations below:

$$\begin{aligned} x &= a\sin\theta\cos\emptyset \\ y &= b\sin\theta\sin\emptyset \\ z &= c\cos\theta \end{aligned} \qquad \text{for } \emptyset \in [0,2\pi) \text{ and } \theta \in [0,\pi] \tag{80}$$

where a, b and c are half axes in x, y and z directions, respectively, which are determined with respect to the physical characteristics of human head.

Antenna element positions and polarization configurations are determined as in the following manner. First of all, elliptical curves shown in Figure 4.26 as blue lines are obtained analytically utilizing the parametric equations (80) for constant v values. The positions of the antennas are calculated on these lines after stating the number of antennas on each line. The separation is accomplished in an equiangular approach. Afterwards, the polarizations are defined for each antenna. Three main components of the polarization term are determined as follows. The polarization called Pol-1 is along with the tangential vector at antenna position on the corresponding elliptical curve. Pol-2 polarization is perpendicular to Pol-1 and tangential on ellipsoidal surface while Pol-3 is the polarization that is perpendicular to the surface at each antenna position.

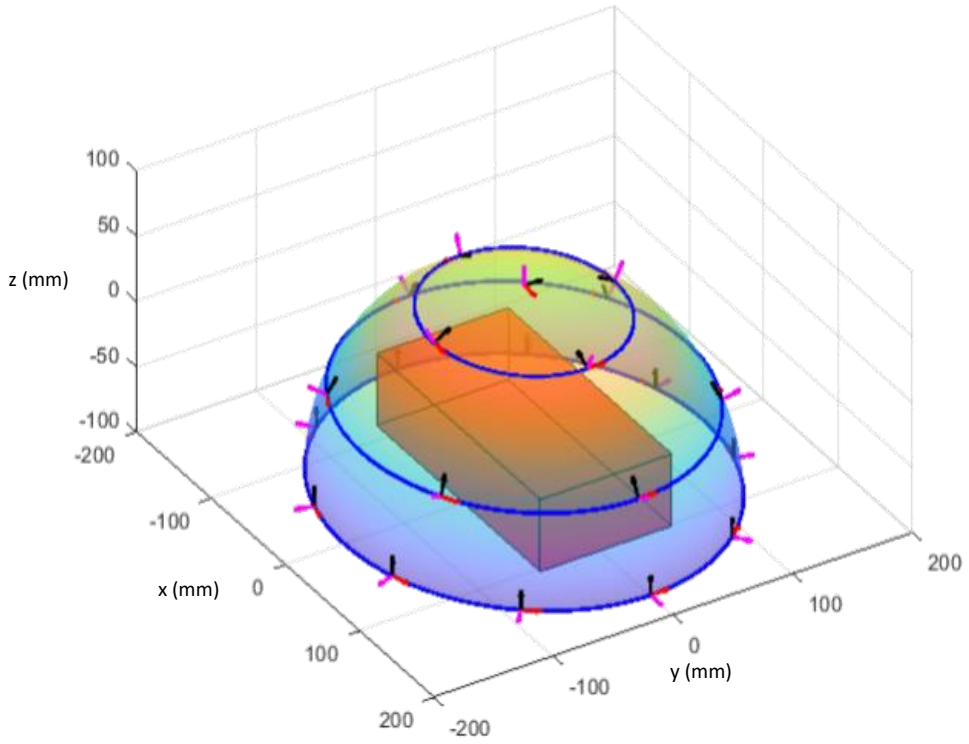

Figure 4.26. Antenna positions and polarization definitions on ellipsoidal surface

Realistic ellipsoid surface definition, referencing to [58], and the replacement of antennas on that surface are accomplished. The antennas have the options to exhibit single, dual, or triple polarizations. In Figure 4.26, antennas on an ellipsoidal surface and the cubical object to be imaged are presented.

As an example, 21 Hertzian dipole antennas are arranged on this ellipsoidal surface in dual polarized configuration covering an object that consists of 8x8x2 voxels in x, y and z directions, respectively. The length of the voxel in each direction is 8.8 mm. The region between the object and ellipsoidal surface is air and it is assumed to be known during the image reconstruction of the object. The scattering object is defined as shown in Figure 4.27 such that it consists of two separate blood regions and white matter medium filling the rest of the scatterer. The distribution given in Figure 4.27 is same for both of the two slices along z-direction. The relative permittivity and conductivity values obtained by using the ellipsoidal antenna configuration are presented in Figure 4.28 for the top slice along z-direction. It can be concluded from

the figures that the larger blood region is easily detectable, and the smaller blood region can be visually detected as well. It is important to note that, the ellipsoidal antenna arrangement and dual polarization configuration provide a resolution of about 1 voxel which is 8.8 mm, together with minimum detectable size of 8.8mm as well.

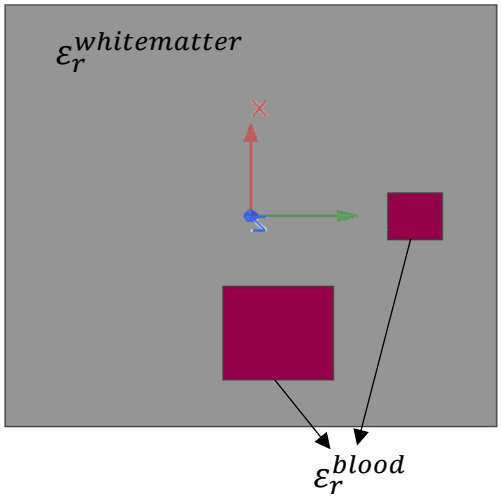

Figure 4.27. Model of the scatterer representing white matter and blood regions

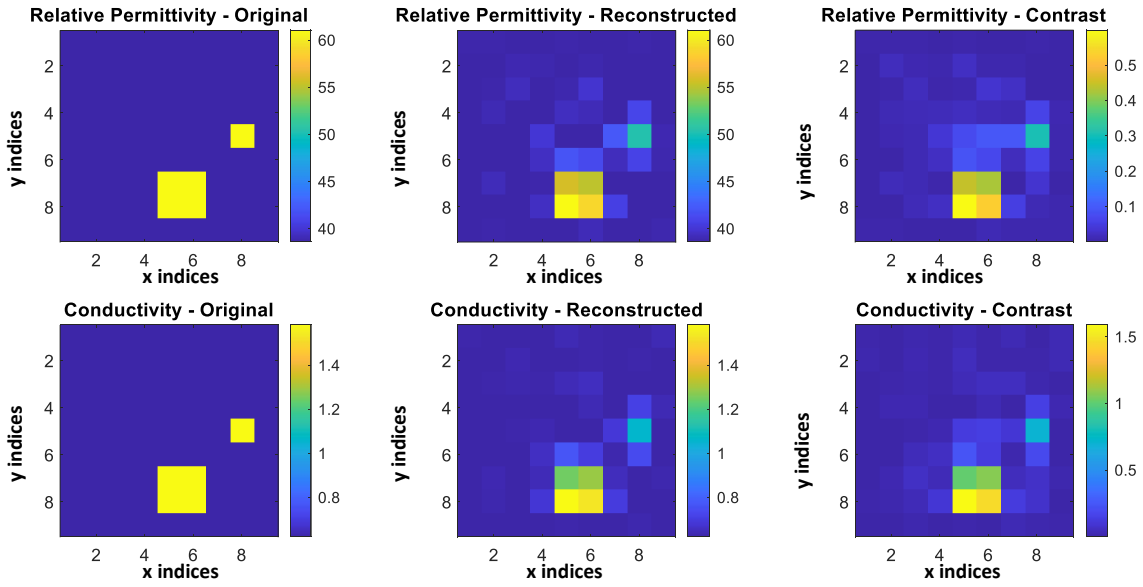

Figure 4.28. Original and reconstructed relative permittivity, conductivity and contrast distributions

4.3 Image Reconstruction with Realistic Head Model

As the goal of this thesis is to construct a near-field microwave imaging system for brain stroke detection, the image reconstruction studies are necessarily to be held using a realistic head model. Therefore, The Zubal head phantom MRI database is used in this study for the construction of a 3D numerical head model [11]. This dataset comprises 128 slices, where each slice contains 256 × 256 cubical elements of voxel size 1.1 × 1.1 × 1.4 mm, a sample view for a transverse cut is given in Figure 4.29. All parts of the brain are indexed separately and a table matching the indexes to different tissues of the brain is presented to the user which helps to implement electromagnetic simulations of human brain.

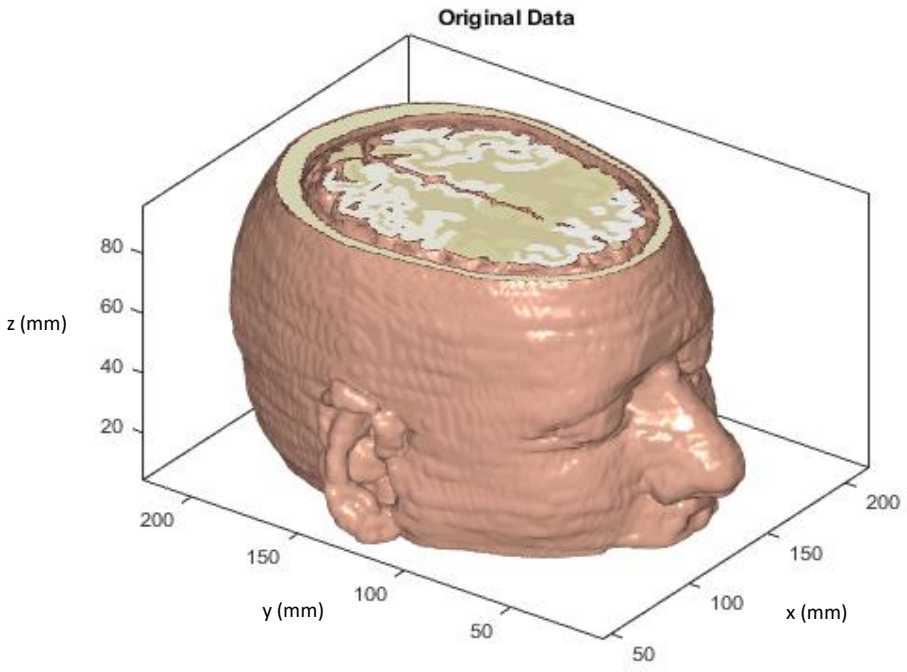

Figure 4.29. Zubal Head Phantom 3D view

The relative permittivity and conductivity distribution of the related brain tissues at 1 GHz are obtained from [67] as follows:

Table 4.2. Relative permittivity and conductivity of brain tissues at 1 GHz [67]

Tissue	Relative Permittivity	Conductance	Tissue	Relative Permittivity	Conductance
Skin	40,936	0,900	Eyeball	55,017	1,206
Skull	12,363	0,156	Cerebral Falx	44,201	0,993
Bone Marrow	5,485	0,043	Teeth	12,363	0,156
Cerebral fluid	68,439	2,455	Tongue	55,017	0,975
Gray Matter	52,282	0,985	Blood	61,065	1,583
White Matter	38,578	0,622	Spinal Cord	32,252	0,600
Fat	5,447	0,054	Skeletal Muscle	54,811	0,978
Trachea	41,779	0,802	Gland	59,470	1,079
Cartilage	42,317	0,829	Esophagus	64,797	1,232

The sagittal, frontal and transverse central cuts of the original data by [11] along with the permittivity and conductivity values mapped from Table 4.2 are presented in Figure 4.30. As the cell size of the original data is much smaller than the required values for brain stroke imaging, modifications are implemented on the data to reduce the resolution and bring it to around 10mm, which is the required and mostly studied resolution for brain stroke [68]. As a result, a head model consisting of 32x32x20 cubic cells in x, y and z dimensions and an edge length of 8.8mm for each cubic cell is created. The sagittal, frontal and transverse sections of the head model are shown in Figure 4.31. Smoothing is applied to manipulate some distortions caused by the resolution reduction, and the modified model presented in Figure 4.32 is obtained.

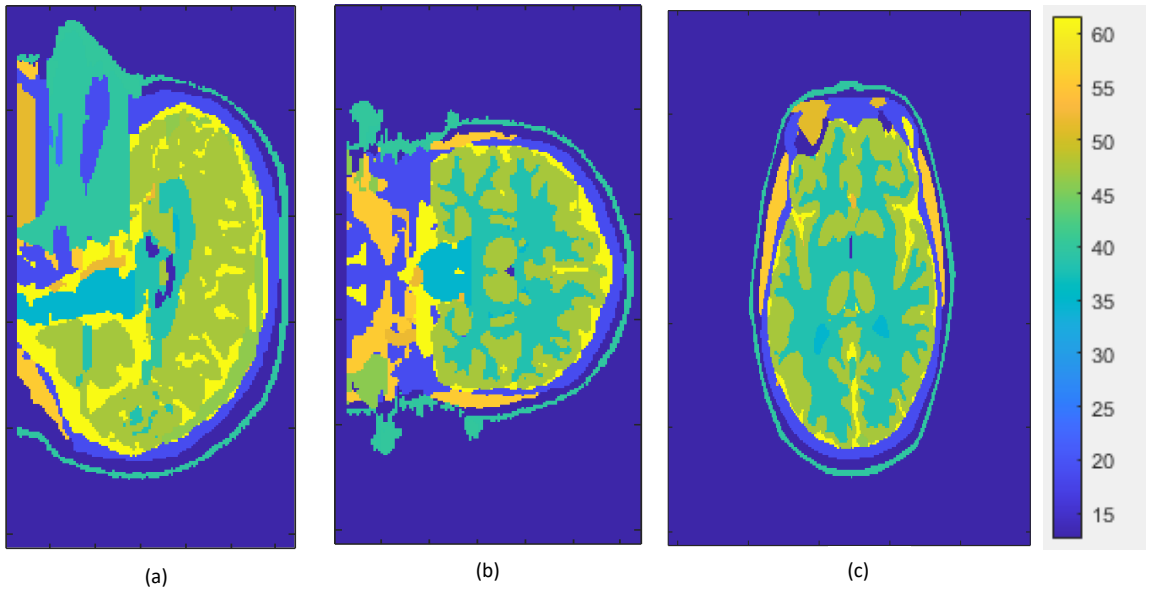

Figure 4.30. Sagittal (a), frontal (b) and transverse (c) cuts of human head tissue permittivity distribution from original data [11] (256x256x128 cells)

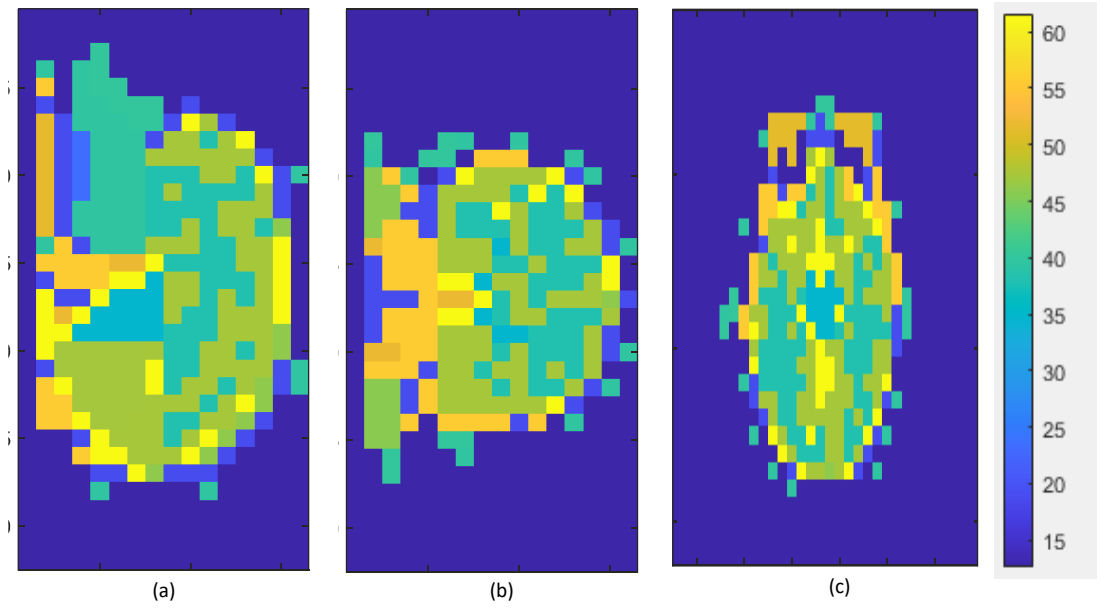

Figure 4.31 Sagittal (a), frontal (b) and transverse (c) cuts of human head tissue permittivity distribution with 32x32x20 cells

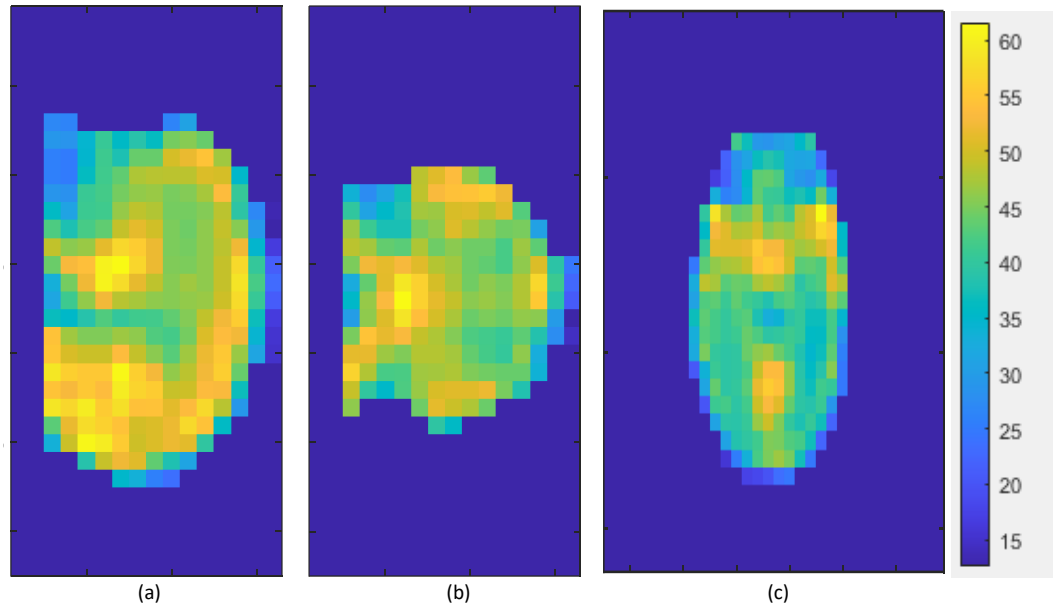

Figure 4.32. Sagittal (a), frontal (b) and transverse (c) cuts of human head tissue permittivity distribution with 32x32x20 cells (Smoothed)

In order to simulate the case with brain hemorrhage, a number of cells with the relative permittivity and conductivity values of blood are inserted inside the created head model. Detailed visuals representing brain stroke are provided in the following figures. Figure 4.33 shows the top view of the placement of 21 dual-polarized Hertzian dipole antennas with a transverse section representing the bleeding region. In Figure 4.34, the same scenario is presented with sagittal, frontal, and transverse sections of head from an isometric view.

In the scope of the thesis, the developed microwave imaging algorithm is executed using the realistic head model and Hertzian dipole antennas placed on an ellipsoidal surface around this model as detailed above. The obtained results, shown in Figure 4.35 and Figure 4.36, demonstrate the contrast images clearly indicating the region with brain stroke. This confirms that the image reconstruction algorithm developed in this thesis performs effectively with the realistic head model as well.

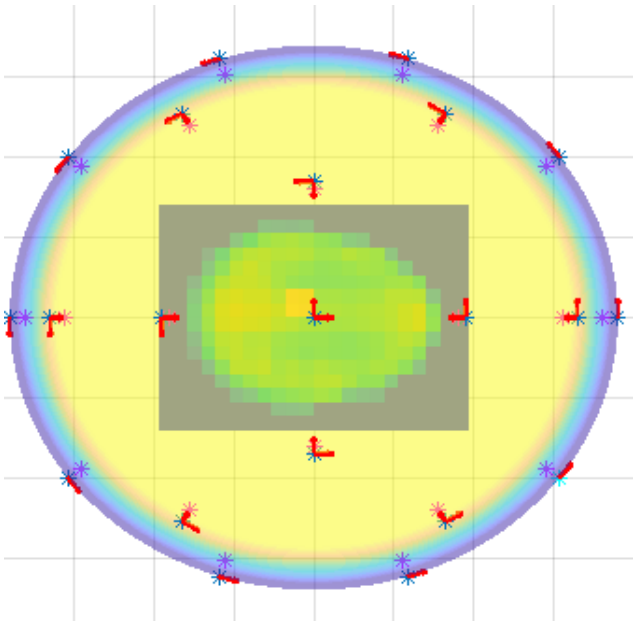

Figure 4.33. Top view of the placement of Hertzian dipole antennas and a transverse section of the head with the bleeding region

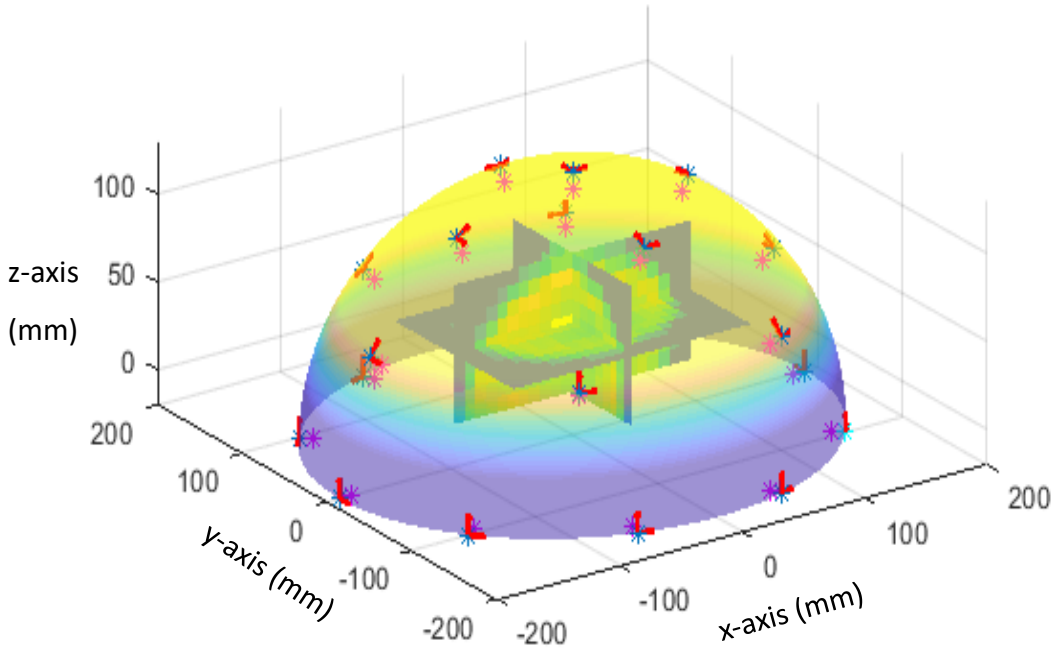

Figure 4.34. Isometric view of the placement of Hertzian dipole antennas and sagittal, frontal, and transverse sections of head with the bleeding region

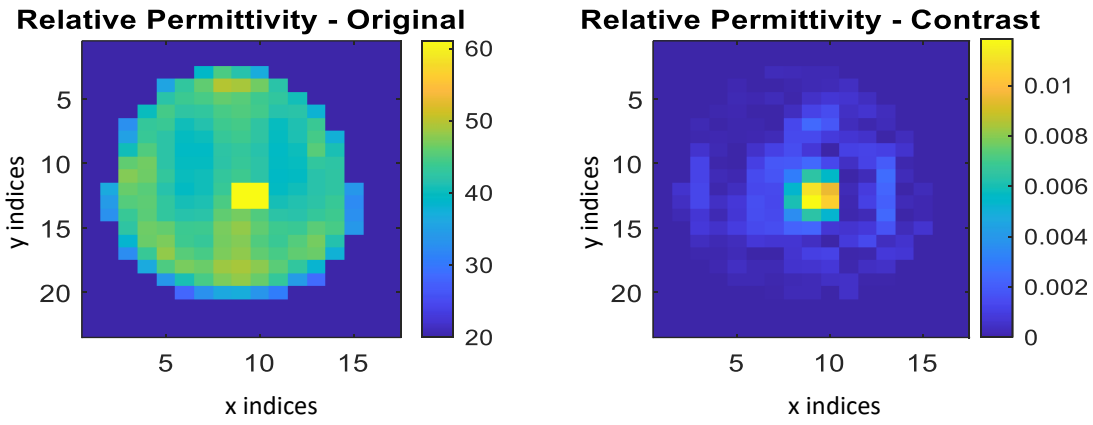

Figure 4.35. Original relative permittivity and reconstructed contrast images for the brain stroke detection

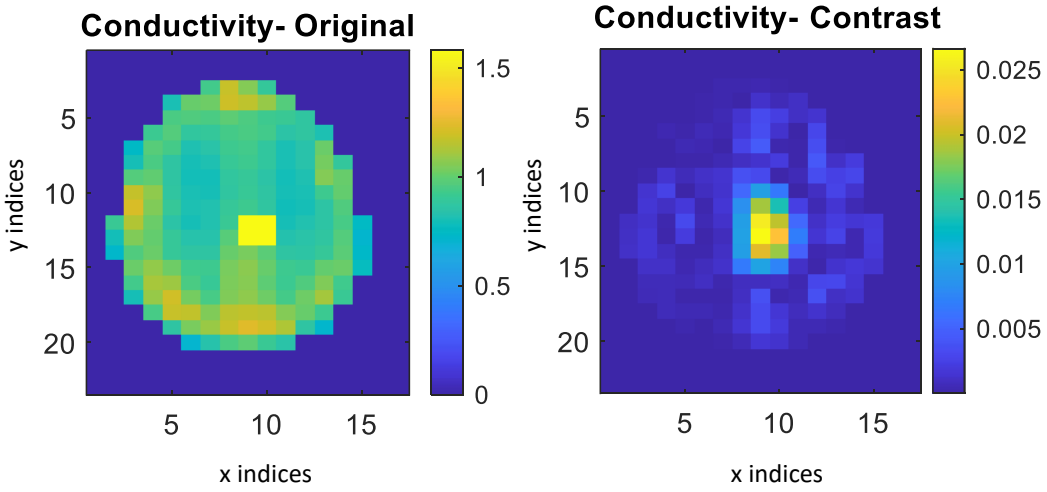

Figure 4.36. Original conductivity and reconstructed contrast images for the brain stroke detection

CHAPTER 5

IMAGE RECONSTRUCTION WITH PATCH ANTENNAS

5.1 Image Reconstruction with Dual Polarized Patch Antennas

This study is carried further by incorporating real antennas into the image reconstruction system. First of all, a dual polarized patch antenna is designed in order to implement the simulations on a realistic base. As a first step, a single polarized patch antenna in Figure 5.1 is designed which exhibits the return loss characteristics in Figure 5.2. A probe-fed square patch antenna is modeled in HFSS, which has dimensions as, dielectric width of 56 mm, metal patch length of 31.26 mm and dielectric thickness of 1.9 mm.

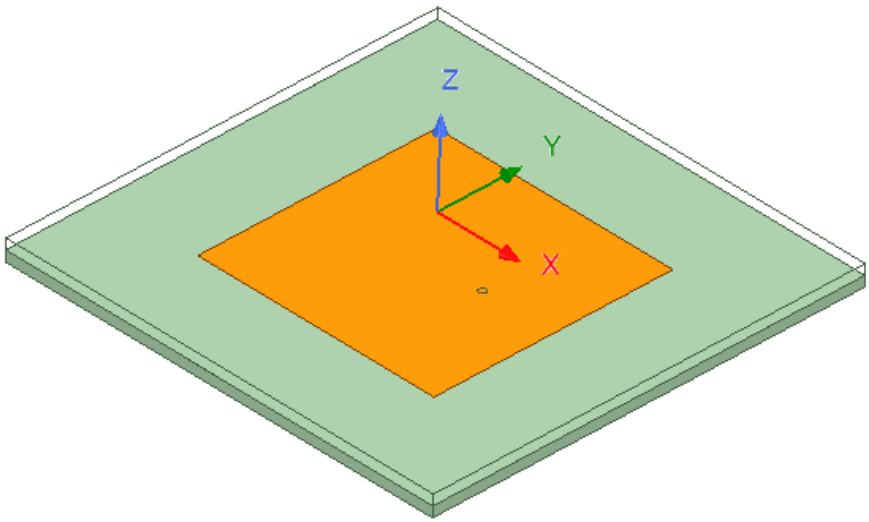

Figure 5.1. Single polarized patch antenna model

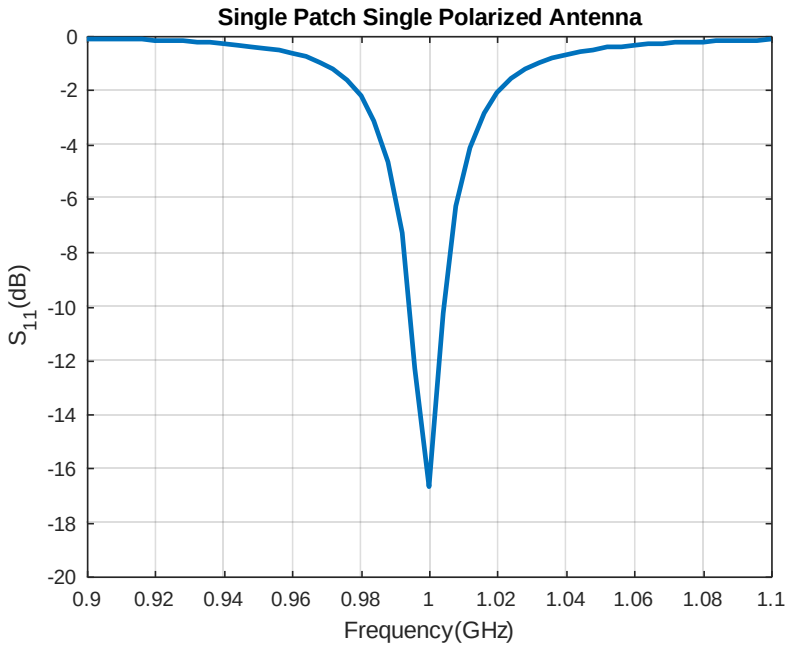

Figure 5.2. Return loss characteristics (S_{11}) of single polarized patch antenna

The operating frequency bandwidth of the patch antenna above is increased by inserting a second parasitic patch layer as presented in Figure 5.3. The second parasitic patch is on another dielectric layer of 1.9 mm thickness and has an edge length of 31.42 mm. The relatively wide-band return loss characteristics of dual patch antenna is demonstrated in Figure 5.4.

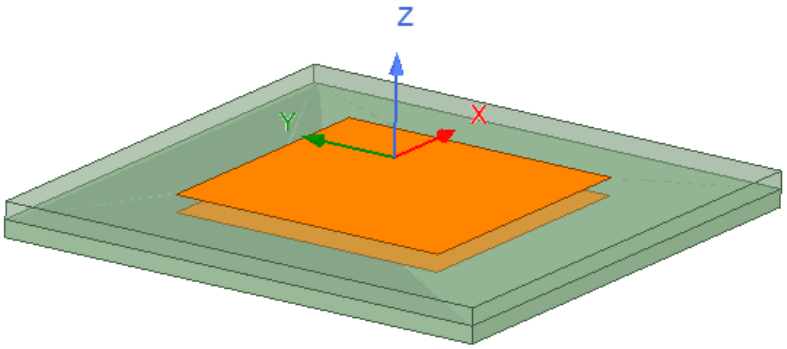

Figure 5.3. Single polarized dual patch antenna model

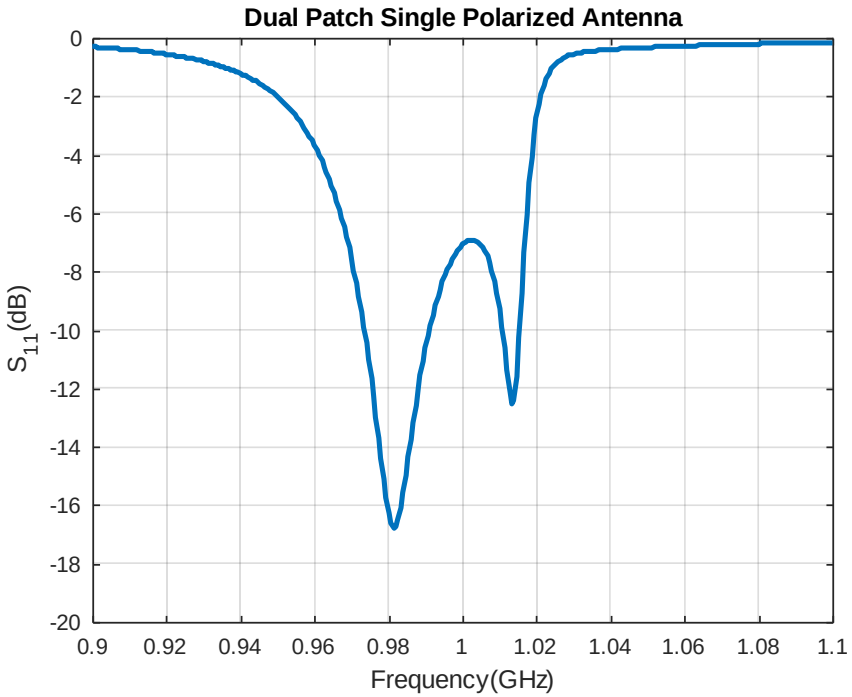

Figure 5.4. Return loss characteristics (S_{11}) of single polarized dual patch antenna

Finally, the second polarization is gained by casting a second port orthogonal to other port with respect to z-axis as given in Figure 5.5. Return loss characteristics of this model is given in Figure 5.6.

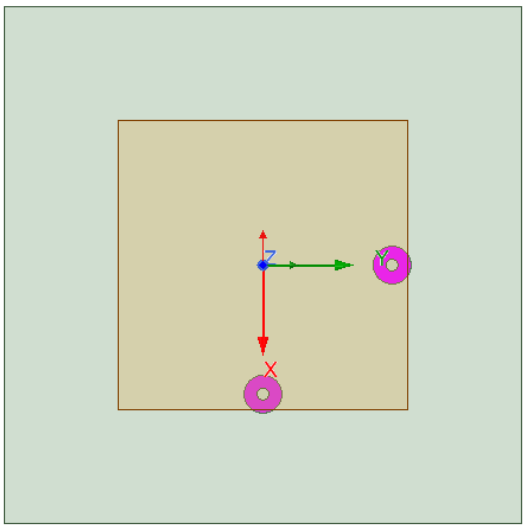

Figure 5.5. Dual-polarized dual-patch antenna model

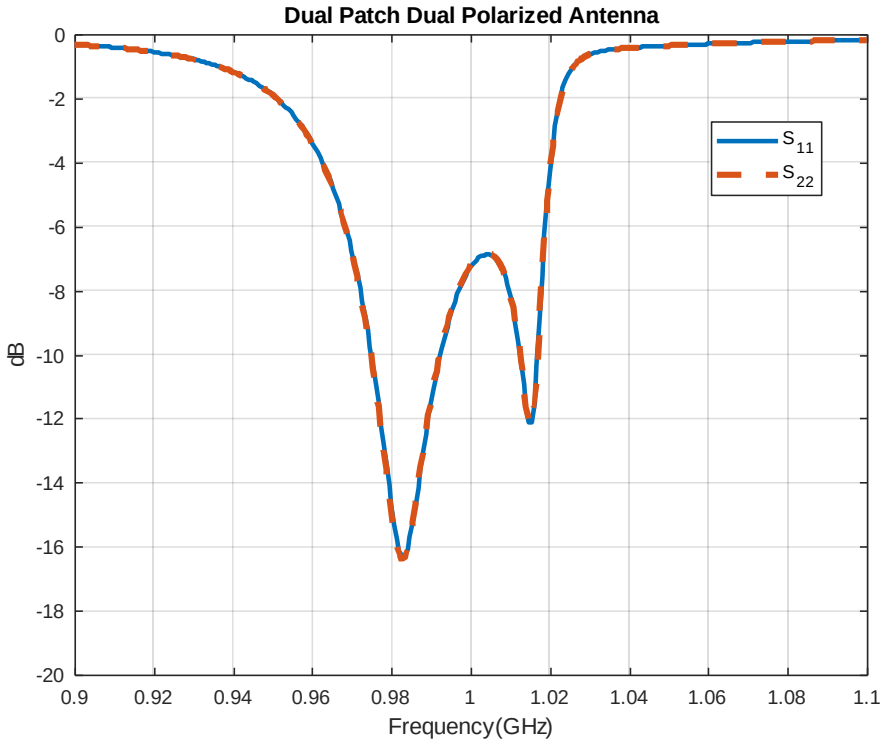

Figure 5.6. Return loss characteristics (S_{11} and S_{22}) of dual-polarized dual-patch antenna model

The ellipsoidal arrangement defined in Section 4.2 of this thesis is implemented for the designed patch antenna and the below realistic image reconstruction system is achieved in order to be utilized for the algorithms developed in this thesis, shown in Figure 5.7 and Figure 5.8.

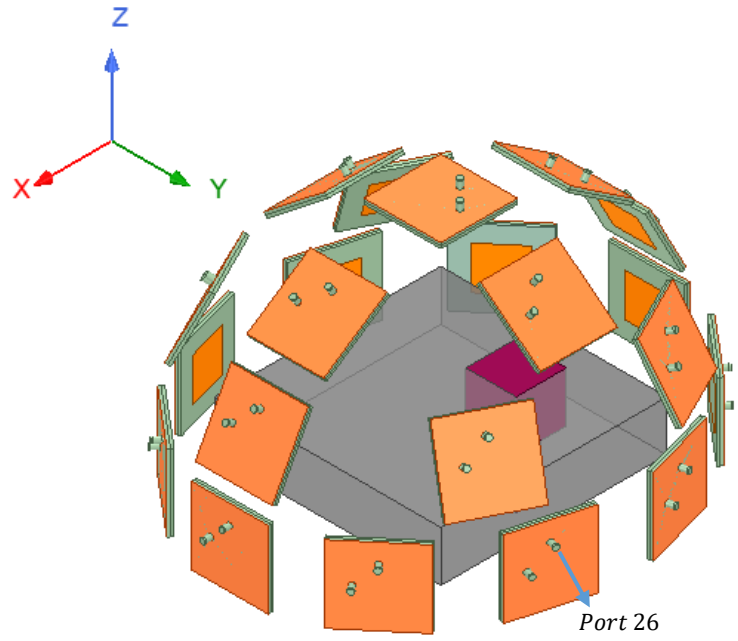

Figure 5.7. Ellipsoidal placement of patch antennas, measurement case with object

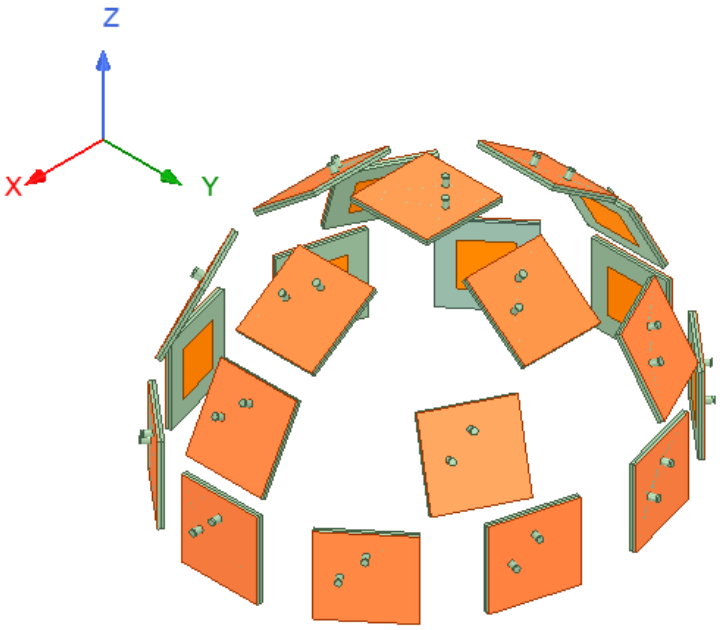

Figure 5.8. Ellipsoidal placement of patch antennas, measurement for incident fields (calibration and characterization)

The procedure for HFSS simulations can be summarized as follows. Firstly, characterization simulations are conducted for the case without any scatterer, and the

field values obtained from these simulations are stored in order to be utilized later. When the scatterer object is introduced, the simulations are repeated, and S-parameter values are obtained as measurement data. Subsequently, the characterization and measurement data obtained from HFSS simulations are fed into the image reconstruction algorithm, as described in Section 2.3.1 and Section 3.1, the image reconstruction process is performed.

Regarding HFSS simulations, two important points should be highlighted. Firstly, for accurate calculation of the field values to be stored as simulation results, special mesh operations are required to be defined at the relevant regions, which include the volume where the object is located and the area where field samples are taken at the antenna apertures (see Figure 5.9). The simulations are required to be executed after defining the mesh operations.

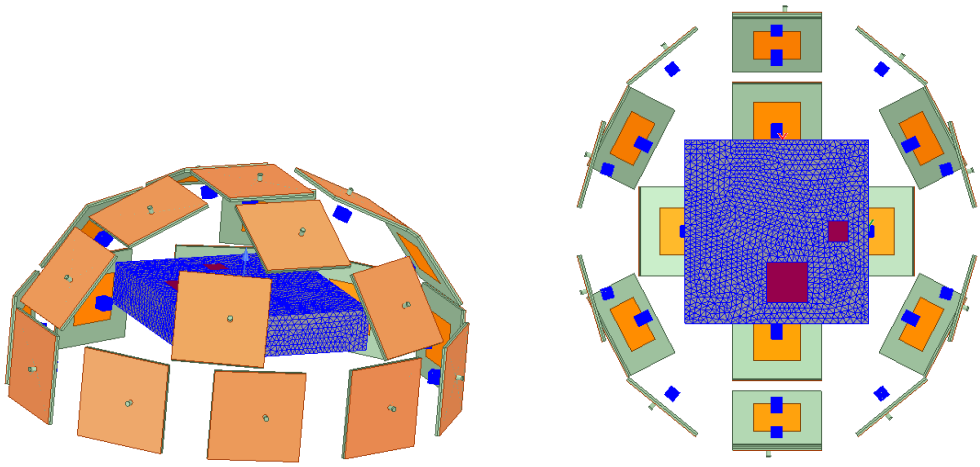

Figure 5.9. Mesh operations regions (blue) defined for accurate simulation results in HFSS

Secondly, the polarity vectors of the antenna ports must be predefined to be compatible with each other. If no prior definition is applied, there can be a 180-degree phase difference in excitation between the simulations performed with and without the scatterer at some ports (see Figure 5.10). To prevent this situation and avoid potential processing errors, the polarity of all ports should be defined during the port assignment process.

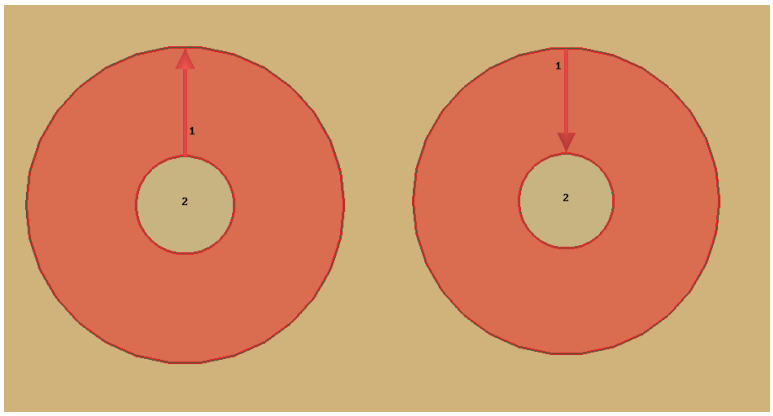

Figure 5.10. Port polarity definitions with 180-degree phase difference with respect to each other on the coaxial port at HFSS

After completing the steps for preparation, the simulations are conducted for two scenarios: one without the scatterer object and the other with the scatterer object. The scatterer object is modeled as previously shown in Figure 4.27. The data obtained from the simulations is fed into the image reconstruction algorithm developed within the scope of this thesis. The relative permittivity, conductivity, and contrast distributions presented in Figure 5.11 and Figure 5.12 have been obtained. According to these results, the region representing the brain stroke can be successfully detected visually.

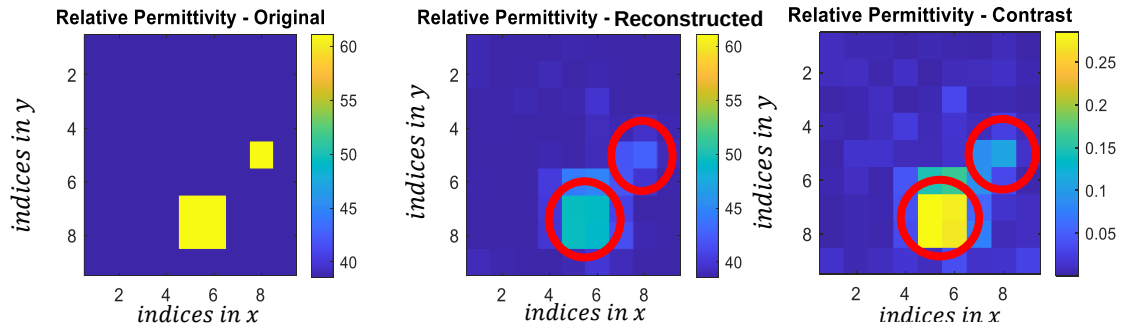

Figure 5.11. Relative permittivity distributions – original, reconstructed and contrast profiles obtained by the imaging system with dual polarized patch antennas

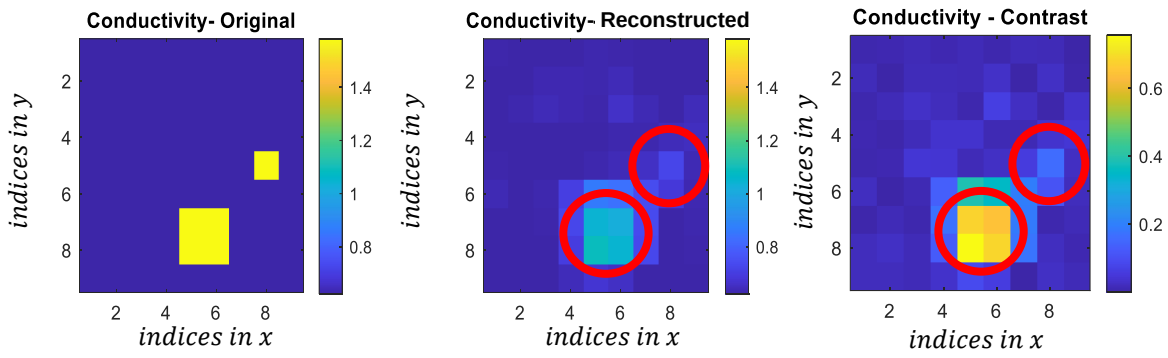

Figure 5.12. Conductivity distributions – original, reconstructed and contrast profiles obtained by the imaging system with dual polarized patch antennas

5.2 Image Reconstruction with Dual Polarized Patch Antennas under Noise

In this section, the impact of noise on the image reconstruction performance is investigated. The simulation data obtained in a noiseless environment in Section 5.1 of this thesis, is manipulated by adding a noise on measured S-parameter data as follows. To begin with, the mean power level (P_s) is computed in dB from the S-parameter matrix, excluding the diagonal elements. Afterwards, signal-to-noise ratio (SNR), which is the ratio between the desired voltage or power of a signal to the undesired signal or the power of the background noise, for the system is defined in dB. Subsequently, a complex Gaussian noise distribution with a variance of (P_s - SNR) is introduced to the initial S-parameter distribution. SNR level for the system in this study is determined as 20 dB. The effect of the given noise on the measured S-parameter characteristics is investigated for the case where Port 26, demonstrated in Figure 5.7, is excited and the rest are receivers. S-parameter characteristics with noise for this specific scenario is obtained for 100 cases with random Gaussian noise samples as depicted in Figure 5.13.

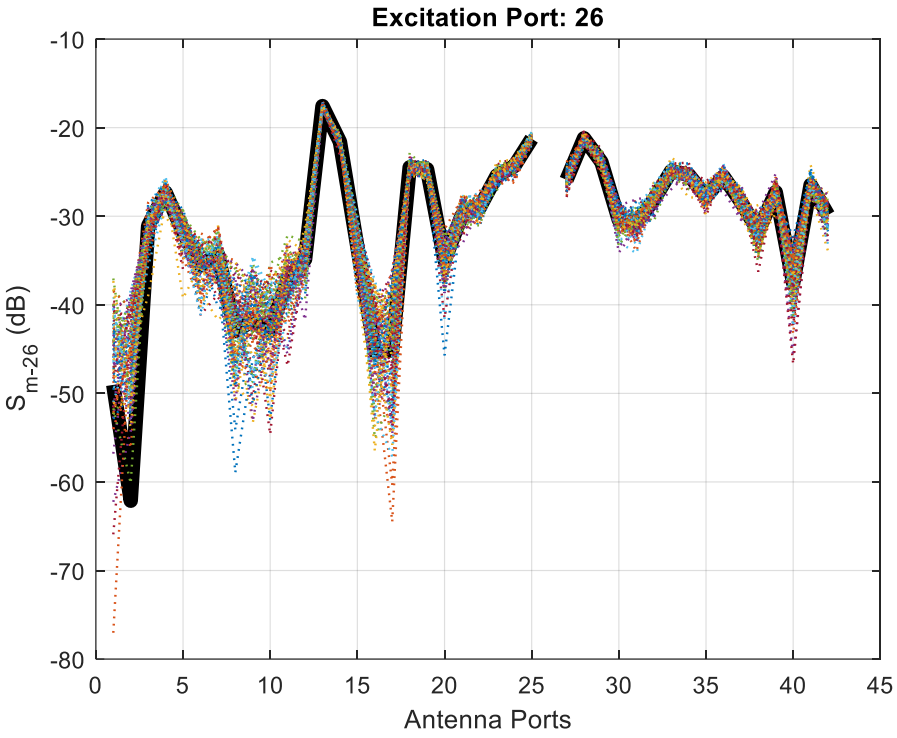

Figure 5.13. Measurement samples with (dashed lines) and without (thick solid black line) noise at receiver ports (excitation port no: 26) (SNR= 20 dB)

The image reconstruction steps are repeated for this measurement data with noise and relative permittivity, conductivity, and related contrast distributions resulting from this study are presented in Figure 5.14 and Figure 5.15.

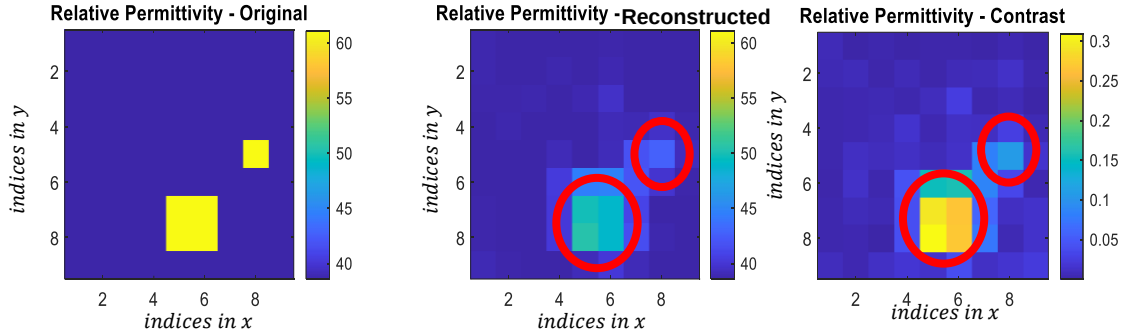

Figure 5.14. Relative permittivity distributions – original, reconstructed and contrast profiles obtained by the imaging system with dual polarized patch antennas with noise (SNR=20 dB)

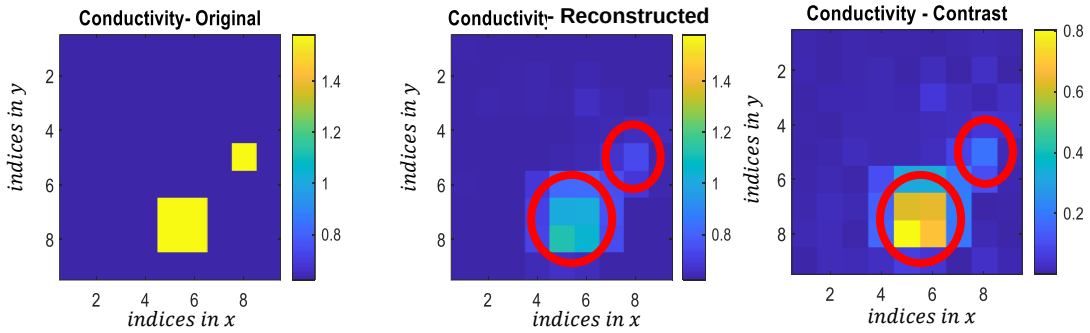

Figure 5.15. Conductivity distributions – original, reconstructed and contrast profiles obtained by the imaging system with dual polarized patch antennas with noise (SNR=20 dB)

For the sake of traceability, the contrast images for both cases, with and without noise, are also given together in Figure 5.16. As seen in the figure, the distribution in the region with blood is more homogeneous for the case without noise compared to the noisy one. However, the images reveal that the image reconstruction algorithm of this thesis study is robust against noise, which might be due to the utilization of regularization in optimization. The results for the noisy operation are consistent with and of acceptable quality when compared to the results acquired in the noiseless scenario.

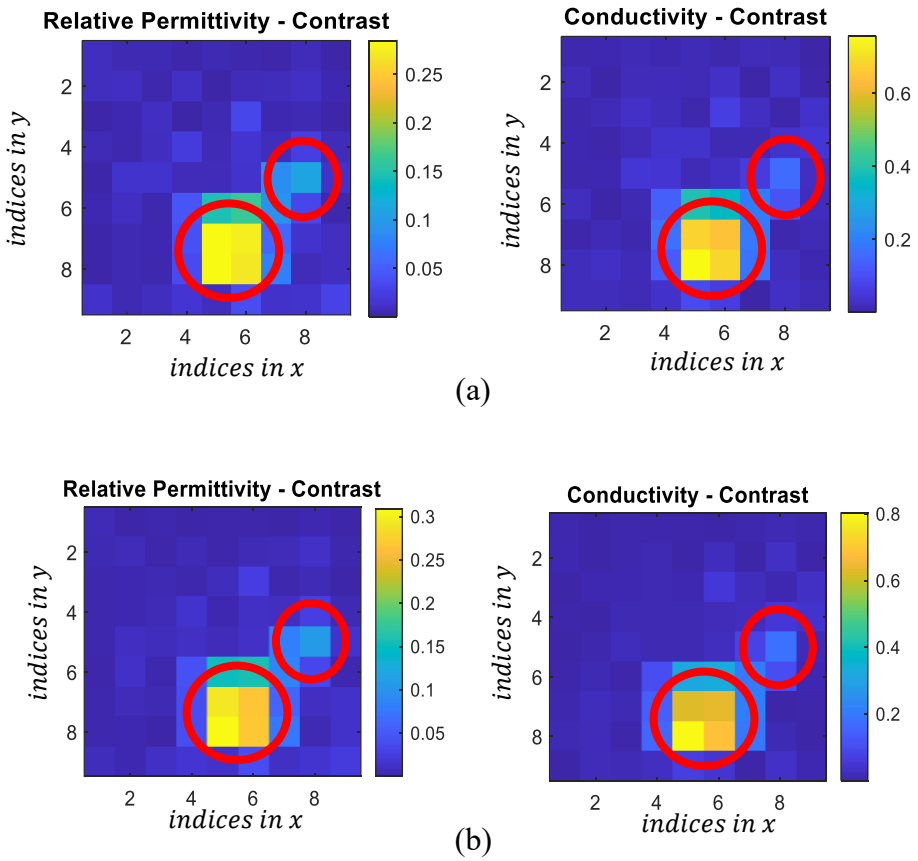

Figure 5.16. Contrast images for reconstructed relative permittivity and conductivity profiles – (a) without noise (b) with noise (SNR=20 dB)

CHAPTER 6

CONCLUSION

In this thesis, we focused on the detection of brain strokes using a near-field microwave imaging system. Our main goal is to improve the accuracy and quality of images by addressing the forward and inverse problem structures. Through a comprehensive literature review, we observed that existing microwave imaging systems have disadvantages such as bulkiness, slow image creation, high false detection rates, and a lack of consideration for practical parameters.

Definitions and derivations of the methodology and formulations related to forward and inverse problems and obtaining regarding state and data equations constitute the first milestones of this thesis study. Afterwards, implementation of the image reconstruction algorithm under various scenarios was an important challenge when we face the difficulties and borders of the current technique which is required to be understood and overcome in order to enhance the performance of near-field microwave imaging systems.

This thesis contributes in three main ways:

Firstly, we proposed an innovative image reconstruction approach using an alternating minimization technique, addressing two optimization variables: current density distribution and dielectric and conductivity profiles. By combining this approach with total variation regularization and the constrained split augmented Lagrangian shrinkage algorithm (C-SALSA), we achieve improved accuracy and efficiency in solving the ill-conditioned inverse problem.

Secondly, in contrast to previous studies utilizing single-polarized antennas, we investigated the impact of different antenna polarization types and the number of antennas on imaging performance. We conducted extensive experiments and found

that utilizing dual-polarized antennas resulted in better imaging performance compared to using twice as many single-polarized antennas. This finding offers practical implications for overcoming constraints related to limited antenna placement on the human head, opening up new possibilities for improved imaging in real-world scenarios.

Thirdly, while previous research conducted detailed full-wave analyses of the imaging system and antennas, we found that directly using this data in iterative image reconstruction algorithms posed computational challenges. Therefore, we developed a novel formulation that efficiently incorporates the near-field data obtained from individual antennas into the forward model, enabling us to utilize this data effectively in the image reconstruction process.

Comparing the resultant performance of the image reconstruction algorithm of this thesis study originating from aforementioned contributions with the results reported in the literature, the image resolution (minimum dimension of the stroke region and/or minimum distance between two separate stroke regions), which is a key parameter since it determines the minimum observable stroke region, is observed to be better in this study. In details, image reconstruction studies in the literature ([18], [33], and [74]) reveal the image resolution as greater than 10 mm. However, the resolution obtained in this thesis study (see Figure 4.28) is 8.8 mm, which is better than the results found in the literature.

In terms of number of frequencies of the measurements, it is evident that the quality of the images gets better as more information is gathered by multi-frequency system compared to single frequency operation as in this thesis study. Moreover, by capturing data from various frequency components, it becomes easier to differentiate between different materials and detect abnormal variations in electrical properties in the imaging domain. This can be particularly advantageous for detecting and identifying the stroke with greater accuracy. However, wideband frequency range imaging generates a larger amount of data that requires more sophisticated

processing techniques. Signal processing and image reconstruction becomes more complex, which may require more computational resources and efficient algorithms.

Overall, this thesis enhances our understanding of brain stroke detection using near-field microwave imaging and demonstrates the way for future research and practical applications in the field. The findings presented here offer valuable insights for researchers and practitioners, indicating critical points for further advancements in microwave imaging technology.

In future studies, a comprehensive system analysis can be conducted using a realistic head model and antenna elements together. For the head modeling, employing more complex mesh types such as tetrahedral or hexahedral elements, in contrast to cubic elements, which reduce the complexity of solving the forward problem and accelerates the process, could lead to enhanced outcomes if a more efficient solution approach is devised. For the antenna part, increasing the frequency bandwidth or utilizing dual-band operation also has the potential to yield significantly improved results.

REFERENCES

[1] L. E. Larsen and L. H. Jacobi, Eds., Medical Applications of Microwave Imaging. New York: IEEE Press, 1986.

[2] M. Miyakawa and J.-C. Bolomey, Eds., Non-Invasive Thermometry of the Human Body. Boca Raton, FL: CRC Press, 1996.

[3] Z. Q. Zhang and Q. H. Liu, "Three-Dimensional Nonlinear Image Reconstruction for Microwave Biomedical Imaging", IEEE Transactions on Biomedical Engineering, vol. 51, no. 3, March 2004.

[4] S. Lambot, E. C. Slob, I. van den Bosch, B. Stockbroeckx, and M. Vanclooster," Modeling of Ground-Penetrating Radar for Accurate Characterization of Subsurface Electric Properties", IEEE Transactions on Geoscience and Remote Sensing, vol. 42, no. 11, November 2004.

[5] I. Catapano and L. Crocco, "An Imaging Method for Concealed Targets", IEEE Transactions on Geoscience and Remote Sensing, vol. 47, no. 5, May 2009.

[6] M. Pastorino, Microwave Imaging, Hoboken N.J.: John Wiley, 2010.

[7] S. Semenov and D. Corfield, "Microwave Tomography for Brain Imaging: Feasibility Assessment for Stroke Detection", International Journal of Antennas and Propagation, 2008.

[8] M. A. Ali and M. Moghaddam, "3D Nonlinear Super-Resolution Microwave Inversion Technique Using Time-Domain Data", IEEE Transactions on Antennas and Propagation, vol. 58, no. 7, July 2010.

[9] D. Ireland and M. Bialkowski, "Feasibility Study on Microwave Stroke Detection using a Realistic Phantom and the FDTD Method", Proceedings of Asia-Pacific Microwave Conference, 2010.

[10] R. Scapaticci, L. Di Donato, I. Catapano, and L. Crocco, "A Feasibility Study on Microwave Imaging for Brain Stroke Monitoring", Progress in Electromagnetics Research B, vol. 40, 305-324, 2012.

[11] I.G. Zubal, C.R. Harrell, E.O. Smith, Z. Rattner, G. Gindi and P.B. Hoffer, "Computerized three-dimensional segmented human anatomy", Medical Physics, 21(2):299-302, 1994.

[12] A.T. Mobashsher, and A. Abbosh, “Microwave System to Detect Traumatic Brain Injuries Using Compact Unidirectional Antenna and Wideband Transceiver with Verification on Realistic Head Phantom”, IEEE Transactions on Microwave Theory and Techniques, vol. 62, no. 9, September 2014.

[13] B. J. Mohammed, A. M. Abbosh, S. Mustafa, and D. Ireland, “Microwave System for Head Imaging”, IEEE Transactions on Instrumentation and Measurement, vol. 63, no. 1, January 2014.

[14] A. T. Mobashsher, A Mahmoud and A. Abbosh, “Portable Wideband Microwave Imaging System for Intracranial Hemorrhage Detection Using Improved Back-projection Algorithm with Model of Effective Head Permittivity,” Sci. Rep. 6, 20459; doi: 10.1038/srep20459 (2016).

[15] A. S. M. Alqadami , A. Trakic , A. E. Stancombe, B. Mohammed , K. Bialkowski , and A. Abbosh, “Flexible Electromagnetic Cap for Head Imaging”, IEEE Transactions on Biomedical Circuits and Systems, Vol. 14, No. 5, October 2020.

[16] I. Bisio, C. Estatico, A. Fedeli , F. Lavagetto, M. Pastorino, A. Randazzo, and A. Sciarrone, “Brain Stroke Microwave Imaging by Means of a Newton-Conjugate-Gradient Method in L^p Banach Spaces”, IEEE Transactions on Microwave Theory and Techniques, vol. 66, no. 8, August 2018.

[17] R. Scapaticci, J. Tobon, G. Bellizzi, F. Vipiana,, and L. Crocco, “Design and Numerical Characterization of a Low-Complexity Microwave Device for Brain Stroke Monitoring”, IEEE Transactions on Antennas and Propagation, vol. 66, no. 12, December 2018.

[18] D. O. Rodriguez-Duarte, C. Origlia, J. A. T. Vasquez, R. Scapaticci, L. Crocco, and F. Vipiana, “Experimental Assessment of Real-Time Brain

Stroke Monitoring via a Microwave Imaging Scanner", IEEE Open Journal of Antennas and Propagation, August 2022.

[19] Imran M. Saied and Tughrul Arslan, "Noninvasive Wearable RF Device Towards Monitoring Brain Atrophy and Lateral Ventricle Enlargement", IEEE Journal of Electromagnetics, RF, and Microwaves In Medicine and Biology, Vol. 4, No. 1, March 2020.

[20] S. Mustafa, B. Mohammed, and A. Abbosh, "Novel Preprocessing Techniques for Accurate Microwave Imaging of Human Brain", IEEE Antennas and Wireless Propagation Letters, vol. 12, 2013.

[21] L. Guo and A. Abbosh, "Microwave Stepped Frequency Head Imaging Using Compressive Sensing with Limited Number of Frequency Steps", IEEE Antennas and Wireless Propagation Letters, vol. 14, 2015.

[22] Z. Wei and X. Chen, "Deep-Learning Schemes for Full-Wave Nonlinear Inverse Scattering Problems", IEEE Transactions on Geoscience and Remote Sensing, vol. 57, no. 4, April 2019.

[23] A. Brankovic, A. Zamani, A. Trakic, K. Bialkowski, B. Mohammed, D. Cook, J. Walsham, and A. M. Abbosh, "Unsupervised Algorithm for Brain Anomalies Localization in Electromagnetic Imaging", IEEE Transactions on Computatıinal Imaging, vol. 6, 2020.

[24] Salucci, M.; Polo, A.; Vrba, J. Multi-Step Learning-by-Examples Strategy for Real-Time Brain Stroke Microwave Scattering Data Inversion. Electronics 2021, 10, 95. https://doi.org/10.3390/ electronics10010095.

[25] S. D. Campbell, R. P. Jenkins, P. J. O'Connor, and D. H. Werner, "The Explosion of Artificial Intelligence in Antennas and Propagation", pp.16-27, IEEE Antennas & Propagation Magazine, June 2021.

[26] G. Chen , P. Shah , J. Stang, and M. Moghaddam, "Learning-Assisted Multimodality Dielectric Imaging", IEEE Transactions on Antennas and Propagation, vol. 68, no. 3, March 2020.

[27] M. Persson, A. Fhager, H. D. Trefna, Y. Yu, T. McKelvey, G. Pegenius, J. Karlsson and M. Elam, "Microwave-Based Stroke Diagnosis Making Global

Prehospital Thrombolytic Treatment Possible", IEEE Transactions on Biomedical Engineering, vol. 61, no. 11, November 2014.

[28] V. L. Coli , P. Tournier, V. Dolean, I. El Kanfoud, C. Pichot , C. Migliaccio , and L. Blanc-Féraud, "Detection of Simulated Brain Strokes Using Microwave Tomography", IEEE Journal of Electromagnetics, RF, and Microwaves in Medicine and Biology, vol. 3, no. 4, December 2019.

[29] I. Bisio, A. Fedeli, F. Lavagetto, G. Luzzati, M. Pastorino, A. Randazzo, and E. Tavanti., "Brain Stroke Detection by Microwave Imaging Systems: Preliminary Two-Dimensional Numerical Simulations", IEEE International Conference on Imaging Systems and Techniques (IST),2016.

[30] M. Slaney, A. C. Kak, and L. E. Larsen, "Limitations of imaging with first-order diffraction tomography," IEEE Trans. Microw. Theory Tech., vol. 32, no. 8, pp. 860–874, Aug. 1984.

[31] W. C. Chew and Y. M. Wang, "Reconstruction of Two-Dimensional Permittivity Distribution Using the Distorted Born Iterative Method", IEEE Transactıons on Medical Imaging, vol 9., no. 2. June 1990.

[32] J.H. Lin, C.C. Lu, Y.M. Wang, W.C. Chew, J.J. Mallorqui, A. Broquetas, C. Pichot, and J. C. Bolomey, "Processing Microwave Experimental Data with the Distorted Born Iterative Method of Nonlinear Inverse Scattering", Antennas and Propagation Society International Symposium, 1993.

[33] D. Ireland, K. Bialkowski and A. Abbosh, "Microwave Imaging for Brain Stroke Detection Using Born Iterative Method", IET Microwaves, Antennas & Propagation, Vol. 7, Iss. 11, pp. 909–915, 2013.

[34] D. E. Livesay and K. Chen, "Electromagnetic Fields Induced Inside Arbitrarily Shaped Biological Bodies", IEEE Transactions on Microwave Theory and Techniques, Vol. MTT-22, No. 12, December 1974.

[35] D. H. Schaubert, D. R. Wilton and A. W. Glisson , "A Tetrahedral Modeling Method for Electromagnetic Scattering by Arbitrarily Shaped Inhomogeneous Dielectric Bodies", IEEE Transactions on Antennas and Propagation, Vol. AP-32, No. 1, 1984.

[36] C. Tsai, H. Massoudi, C. H. Durney and M. F. Iskander , “A Procedure for Calculating Fields Inside Arbitrarily Shaped, Inhomogeneous Dielectric Bodies Using Linear Basis Functions with the Moment Method”, IEEE Transactions on Microwave Theory and Techniques, Vol. MTT-34, No. 11, November 1986.

[37] H. Massoudi, C. H. Durney and M. F. Iskander , “Limitations of the Cubical Block Model of Man in Calculating SAR Distributions”, IEEE Transactions on Microwave Theory and Techniques, Vol. MTT-32, No. 8, August 1984.

[38] J. P. Kottman and O. J. F. Martin , “Accurate Solution of the Volume Integral Equation for High-Permittivity Scatterers”, IEEE Transactions on Antennas and Propagation, Vol. 48, No. 11, 2000.

[39] I. Bisio, A. Fedeli, F. Lavagetto, G. Luzzati, M. Pastorino, A. Randazzo, and E. Tavanti., “Brain Stroke Detection by Microwave Imaging Systems: Preliminary Two-Dimensional Numerical Simulations”, IEEE International Conference on Imaging Systems and Techniques (IST),2016.

[40] Caorsi, S., Gragnani, G.L., Pastorino, M., “Two-dimensional microwave imaging by a numerical inverse scattering solution”, IEEE Trans. Microwave Theory Tech., 1990, 38, (8), pp. 981–989.

[41] K. Sertel and J. L. Volakis , “Method of moments solution of volume integral equations using parametric geometry modeling”, Radio Science, Vol. 37, No. 1, 1010, 2002.

[42] X. Li and S. C. Hagness, “A Confocal Microwave Imaging Algorithm for Breast Cancer Detection”, IEEE Microwave and Wireless Components Letters, vol. 11, issue 3, 2001.

[43] M. A. Ali and M. Moghaddam, “3D Nonlinear Super-Resolution Microwave Inversion Technique Using Time-Domain Data”, IEEE Transactions on Antennas and Propagation, vol. 58, no. 7, July 2010.

[44] I. T. Rekanos, M. S. Efraimidou, and T. D. Tsiboukis , “Microwave Imaging: Inversion of Scattered Near-Field Measurements”, IEEE Transactions on Magnetics, Vol. 37, No.5, 2001.

[45] E. A. Attardo, A. Borsic, G. Vecchi, and P. M. Meaney, “Whole-System Electromagnetic Modeling for Microwave Tomography”, IEEE Antennas and Wireless Propagation Letters, vol. 11, 2012.

[46] Z. Li, J. Wang, J. Wu and Q. H. Liu , “A Fast Radial Scanned Near-Field 3-D SAR Imaging System and the Reconstruction Method”, IEEE Transactions on Geoscience and Remote Sensing, Vol. 53, No. 3, 2015.

[47] A. E. Souvorov, A. E. Bulyshev, S. Y. Semenov, et al., “Microwave tomography: a two-dimensional Newton iterative scheme,” IEEE Transactions on Microwave Theory and Techniques,vol. 46, no. 11, pp. 1654–1659, 1998.

[48] T. K. Sarkar, E. Arvas, and S. M. Rao, “Application of fast fourier transform and the conjugate gradient method for efficient solution of electromagnetic scattering from both electrically large and small conducting bodies,” Electromagnetics, vol. 5, pp. 99–122, 1985.

[49] Z. Q. Zhang and Q. H. Liu, “A volume adaptive integral method (VAIM) for 3-D inhomogeneous objects,” IEEE Antennas Wireless Propagat. Lett., vol. 1, pp. 102–105, 2002.

[50] L. V. Kantorovic and G. P. Akilov, “Functional Analysis in Normed Spaces”, Pergamon Press, Oxford, pp. 586-587, 1964.

[51] R. F. Harrington, “Matrix Methods for Field Problems”, Proc. IEEE, vol.55, no.2, 1967.

[52] M. N. O. Sadiku, “Numerical Techniques in Electromagnetics”, CRC Press, 2001.

[53] M. Afonso, J. Bioucas-Dias, and M. Figueiredo, “Fast image recovery using variable splitting and constrained optimization,” IEEE Trans. Image Process., vol. 19, no. 9, pp. 2345–2356, Sep. 2010.

[54] M. Afonso, J. Bioucas-Dias, and M. Figueiredo, “An Augmented Lagrangian Approach to the Constrained Optimization Formulation of Imaging Inverse Problems,” IEEE Trans. Image Process., vol. 20, no. 3, pp. 681-695, Mar. 2011.

[55] F. S. Oktem, “Sparsity-based three-dimensional image reconstruction for near-field MIMO radar imaging”, Turkish Journal of Electrical Engineering and Computer Sciences, vol. 27, no.5, Article 2, 2019.

[56] C. R. Vogel and M. E. Oman, “Robust Total Variation-based Reconstruction of Noisy, Blurred Images”, IEEE Trans Image Process, 7 (6), pp. 813-824, 1998.

[57] D. Geman and C. Yang, “Nonlinear Image Recovery with Half-Quadratic Regularization”, IEEE Trans Image Process, 4 (7), pp. 932-946, 1995.

[58] Department of Defense Human Factors Engineering Technical Advisory Group (DOD HFE TAG), “Static Adult Human Physical Characteristics of The Adult Head”, April 2000.

[59] J. Liu, L. Chen, H. Xiong and Y. Han, “Review of Microwave Imaging Algorithms for Stroke Detection”, Medical & Biological Engineering & Computing, May 2023.

[60] R. L. Leijsen and et. al., “3-D Contrast Source Inversion- Electrical Properties Tomography”, IEEE Transactions on Medical Imaging, vol. 37, no. 9, pp. 2080-2089, 2018.

[61] E. C. Fear, X. Lii S. C. Hagness and M. A. Stuchly, “Confocal Microwave Imaging for Breast Cancer Detection: Localization of Tumors in Three Dimensions ”, IEEE Transactions on Biomedical Engineering, vol. 49, issue 8, 2002.

[62] D. O. Rodriguez-Duarte, J. A. T. Vasquez, R. Scapaticci, L. Crocco and F. Vipiana, "Assessing a Microwave Imaging System for Brain Stroke Monitoring via High Fidelity Numerical Modelling," in IEEE Journal of Electromagnetics, RF and Microwaves in Medicine and Biology, vol. 5, no. 3, pp. 238-245, Sept. 2021.

[63] A. Dalkılıç and L. Alatan, "The Effect of Antenna in the Forward Model of Near Field Microwave Imaging Systems," 2019 IEEE International Symposium on Antennas and Propagation and USNC-URSI Radio Science

Meeting, Atlanta, GA, USA, 2019, pp. 1679-1680, doi: 10.1109/APUSNCURSINRSM.2019.8888996

[64] J. Richmond, "A Reaction Theorem and Its Application to Antenna Impedance Calculations," IRE Transactions on Antennas and Propagation, pp. 515-520, 1961.

[65] H. A. Van der Vorst, "Bi-CGSTAB: A Fast and Smoothly Converging Variant of Bi-CG for the Solution of Nonsymmetric Linear Systems". SIAM J. Sci. Stat. Comput. 13 (2): 631–644, 1992.

[66] Y. E. Gül, "Fast simulation and modeling of scattering from targets in MIMO imaging systems," M.S. - Master of Science, Middle East Technical University, 2022.

[67] "Dielectric Properties," IT'IS Foundation, [Online], https://itis.swiss/virtual-population/tissue-properties/database/dielectric-properties/. [Accessed: Jul.30, 2023].

[68] M. Q. Awais, M. Zartasha, M. Samah, "Finite-element analysis of microwave scattering from a three-dimensional human head model for brain stroke detection", R Soc Open Sci. 2018;5(7):180319. Published 2018 Jul 11. doi:10.1098/rsos.180319

[69] V. Rokhlin, "Rapid solution of integral equations of classical potential theory", Journal of Computational Physics, 60(2):187–207, 1985.

[70] L. Greengard and V. Rokhlin, "A fast algorithm for particle simulation", Journal of Computational Physics, 73:325–348, 1987.

[71] E. A. Miran, F. S. Oktem and S. Koc, "Sparse Reconstruction for Near-Field MIMO Radar Imaging Using Fast Multipole Method," in IEEE Access, vol. 9, pp. 151578-151589, 2021, doi: 10.1109/ACCESS.2021.3126472.

[72] Y. Alvarez, J. Á. Martinez, F. Las-Heras and C. M. Rappaport, "An Inverse Fast Multipole Method for Imaging Applications," in IEEE Antennas and Wireless Propagation Letters, vol. 10, pp. 1259-1262, 2011, doi: 10.1109/LAWP.2011.2175477.

[73] A. Dalkilic, F. S. Oktem and L. Alatan, “Enhanced Near-Field Microwave Imaging System with Polarization Diversity,” Submitted to IEEE Antennas and Wireless Propagation Letters, 2023.

[74] J. Tesarik and O. Fiser, "Evaluating of Spatial and Contrast Resolution Ability of 2D Microwave Imaging System," 2019 PhotonIcs & Electromagnetics Research Symposium - Spring (PIERS-Spring), Rome, Italy, 2019, pp. 1428-1433, doi:10.1109/PIERS-Spring46901.2019.9017663.

APPENDICES

A. Comparative Analysis for the Results of Forward Problem Solver and Reference Studies

For the second case in [34] detailed in Section 2.1.3 (Figure 2.4), The electric field distribution normalized to incident field values at each sampling point for the reference study [34] are given in Appendix Figure 1. The counterpart of these values calculated by the algorithm developed in this study is also presented in Appendix Figure 2 arranged in the same manner.

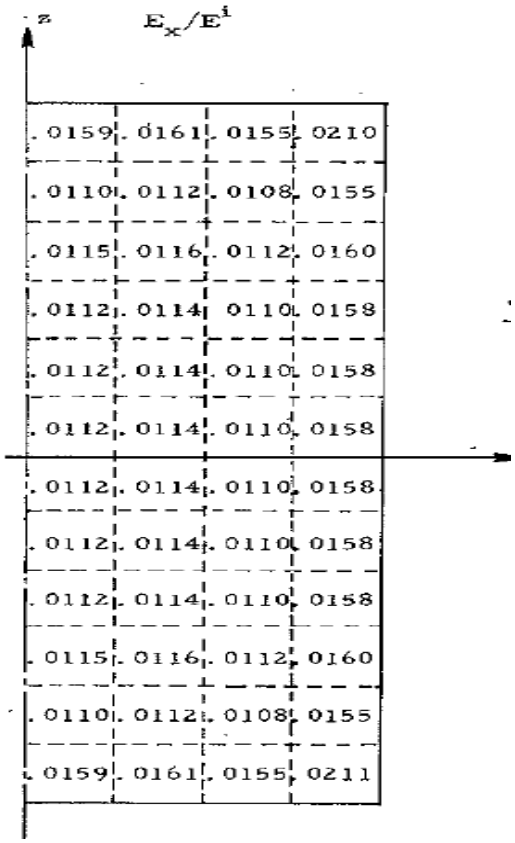

Appendix Figure 1. Reference results from [34] for the model in Figure 2.4

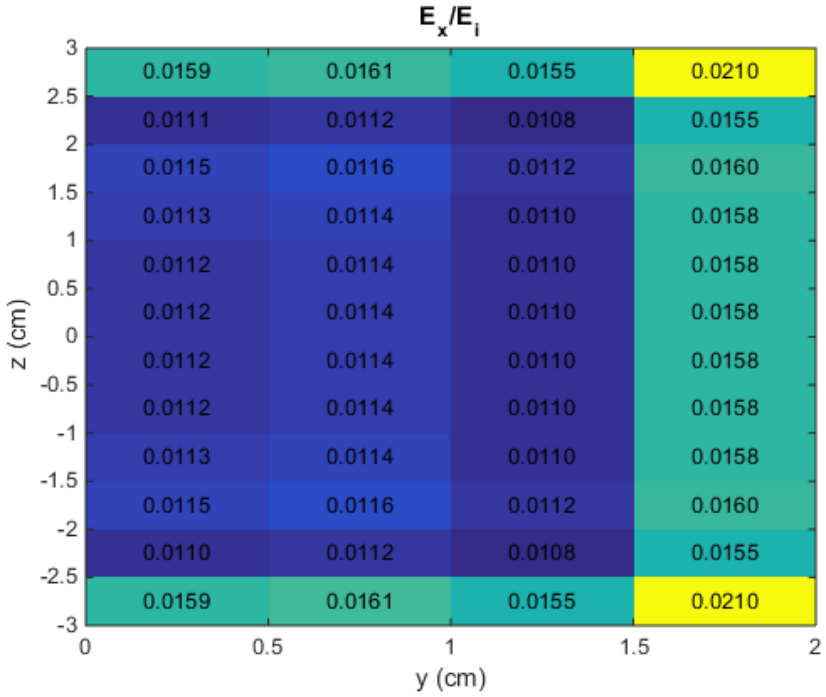

Appendix Figure 2. Implemented electric field distribution normalized to incident field

For the third case observed in [34] and detailed in Section 2.1.3, distribution of x-component of electric field referenced to the incident field obtained by both [34] and our study is demonstrated in Appendix Figure 3, the field values of z-component E-field normalized to incident field are shown in Appendix Figure 4.

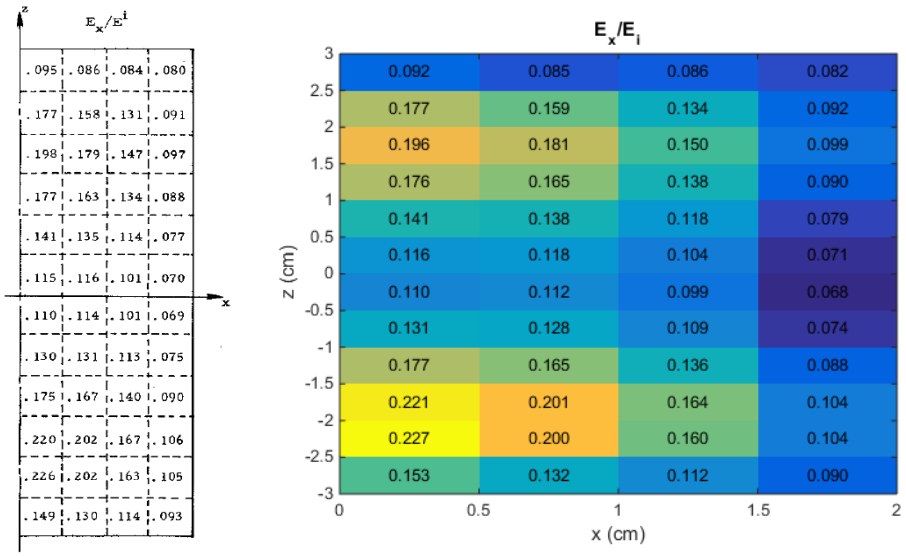

(a) (b)

Appendix Figure 3. Distribution of x-polarized total electric field normalized to incident field: (a) Reference study [34] and (b) This study

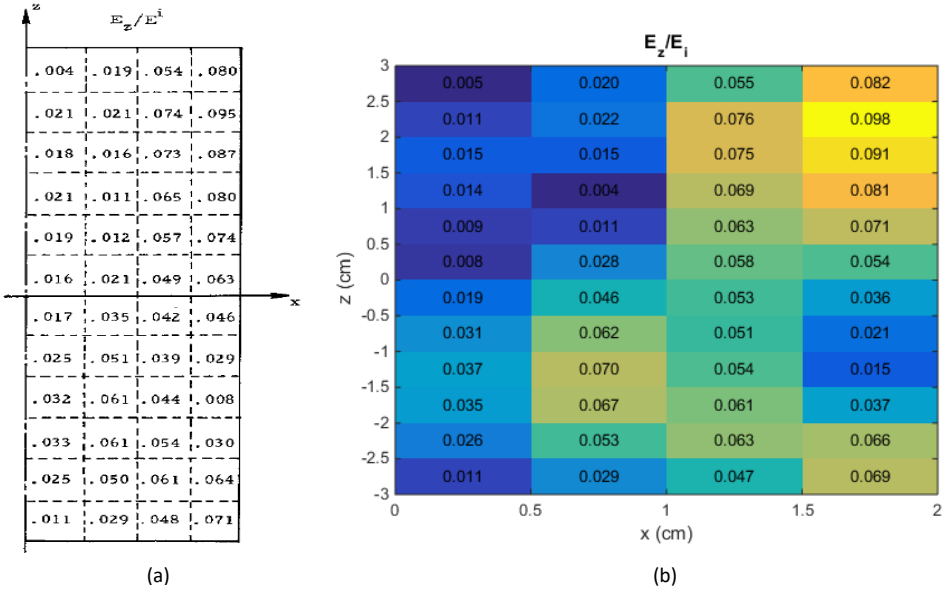

(a) (b)

Appendix Figure 4. Distribution of z-polarized total electric field normalized to incident field: (a) Reference study [34] and (b) This study

CURRICULUM VITAE

Surname, Name: Dalkılıç, Akın

EDUCATION

Degree	Institution	Year of Graduation
MS	METU Electrical and Electronics Engineering	2014
BS	METU Electrical and Electronics Engineering	2011
High School	Ankara Atatürk High School, Ankara	2006

FOREIGN LANGUAGES

Advanced English, Basic Spanish

PUBLICATIONS

1. A. Dalkilic, E. Ercil, "Phase Only Pattern Synthesis Applications for Antenna Arrays", URSI Turkey 6th Scientific Symposium, September 2012. Turkish.

2. C. B. Top, D. Dogan, A. Dalkilic, "Ka-band Circularly Polarized Omni Directional Slotted Waveguide Cylindrical Array Antenna", URSI Turkey 6th Scientific Symposium, September 2012. Turkish.

3. A. Dalkilic, L. Alatan, C. B. Top, "Analysis of Conformal Frequency Selective Surface Radome", Proceedings of European Conference on Antennas and Propagation (EUCAP), April 2014.

4. A. Dalkilic, "Analysis and Design of Conformal Frequency Selective Surfaces", Master Thesis, June 2014.

5. A. Dalkilic, C. Bayram, C. B. Top, E. Ercil, “Slotted Waveguide Array Beamformer Characterization Using Integrated Calibration Channel”, Proceedings of 36th Annual Antenna Measurement Techniques Association (AMTA) Symposium, October 2014.

6. A.Dalkilic, L. Alatan, C. B. Top, “Design of Frequency Selective Surfaces for Curved Structures”, URSI Turkey 8th Scientific Symposium, September 2016. Turkish.

7. A. Dalkilic, D. Dogan and M. E. Inal, “Characterization and Design of Elastomeric Magnetodielectric Materials for Radar Absorber Structures”, 32nd International Union of Radio Science (URSI) General Assembly and Scientific Symposium, August 2017.

8. A. Dalkılıç and L. Alatan, “The Effect of Antenna in the Forward Model of Near Field Microwave Imaging Systems,” 2019 IEEE International Symposium on Antennas and Propagation and USNC-URSI Radio Science Meeting, Atlanta, GA, USA, 2019, pp. 1679-1680, doi: 10.1109/APUSNCURSINRSM.2019.8888996.

9. A. Dalkilic, F. S. Oktem and L. Alatan, “Enhanced Near-Field Microwave Imaging System with Polarization Diversity,” Submitted to IEEE Antennas and Wireless Propagation Letters, 2023.